

UCSF

UC San Francisco Electronic Theses and Dissertations

Title

Mechanisms regulating actin barbed end polymerases of the Ena/VASP protein family

Permalink

<https://escholarship.org/uc/item/06v2q3r9>

Author

Hansen, Scott David

Publication Date

2012

Peer reviewed|Thesis/dissertation

**Mechanisms regulating actin barbed end polymerases
of the Ena/VASP protein family**

by

Scott David Hansen

DISSERTATION

Submitted in partial satisfaction of the requirements for the degree of

DOCTOR OF PHILOSOPHY

in

Biochemistry & Molecular Biology

in the

GRADUATE DIVISION

of the

UNIVERSITY OF CALIFORNIA, SAN FRANCISCO

Acknowledgements

I would like to thank Dyche for buying me a new set of pipets when I agreed to join his lab. I also want to thank him for offering to buy me reading glasses when he noticed that mine were held together with scotch tape. I thank him for listening to my stories during the tough times dealing with my family drama. Most of all, I thank him for giving me the opportunity to succeed and the freedom to choose my own path during graduate school.

I would like to thank Orkun Akin for mentoring me during my early years as graduate student. Orkun and I worked many late nights together in Genentech Hall. He generously shared his technical expertise about *in vitro* reconstitutions, which greatly improved my research and knowledge of biochemistry.

I would like to thank Margot Quinlan, Chris Campbell, Ethan Garner, Brad Zuchero, and Lauren Goins. They were the heart and soul of the Mullins lab when I joined.

I would like to thank my classmates and all the Tetrad graduate program for creating a unique environment for me to earn a thesis. It was a privilege attending UCSF for graduate school.

I would like to thank Ron Vale, Wallace Marshall, David Morgan, Geeta Narlikar, and Henry Bourne to being members of my qualifying exam and thesis committee.

I would like to thank Nico Stuurman for helping us improve our TIRF microscope imaging capabilities and allowing me to use the Vale lab microscopes.

I would like to thank Orion Weiner for having a high level of enthusiasm about science and always making himself available to talk about research.

I would like to thank Peter Bieling for challenging me to do better research and generously sharing reagents. I look forward to our future collaborations.

I would like to thank all of the Hansen and Chang family members for their loving support over the last 6 years.

Finally, I would like to thank my wife, Ann T. Chang, for enriching my life and helping me face many challenges during our 8 year relationship. Together we are invincible. You're the best.

Abstract

In eukaryotic cells, actin networks are built and dynamically reorganized during cell polarization and morphogenesis. The formation of different actin network architectures depends on whether filaments are allowed to elongate persistently or are capped shortly after nucleation. One class of proteins regulating the actin filament length distribution in cells are the barbed end associated proteins, which can terminate or accelerate actin polymerization. Depending on the activity and abundance of these proteins, cells construct actin networks that are either highly branched (lamellipodia) or a densely bundled (filopodia). Regulating the transition between these two types of actin networks, is the ubiquitously expressed Ena/VASP protein family. To determine how Ena/VASP proteins regulate actin assembly I developed a way of visualizing single VASP tetramers interacting with single actin filaments *in vitro*. Visualization of single VASP tetramers revealed several novel mechanisms controlling lateral F-actin interactions, barbed end association, and processivity. Providing an additional level of regulation, I identified a membrane tethered actin binding protein, Lamellipodin, that can modulate Ena/VASP barbed end processivity by simultaneously interacting with filamentous actin. Together these results provide a mechanistic framework for understanding how Ena/VASP proteins regulate actin polymerization and network architecture *in vivo*.

Contributions

The introduction of my dissertation was written in collaboration with Dyche Mullins as a review for Current Opinions in Molecular Biology. The experiments and results described in Chapter 2 and 3 were designed, performed, analyzed, and interpreted by myself. Dyche Mullins assisted in writing the manuscript that resulted from the work in Chapter 2. The study of alpha E-catenin function (Chapter 4) was initiated at Woods Hole by James Nelson and Adam Kwiatkowski (Stanford). All the TIRF microscopy experiment in Chapter 4 were designed and performed by myself. Purification of the alpha E-catenin proteins was performed by Adam Kwiatkowski and Sabine Pokutta (Stanford). The cryo-electron microscopy reconstruction of alpha E-catenin bound to filamentous actin was performed by Chung-Yueh Ouyang, HongJun Liu, Niels Volkmann, and Dorit Hanein (UC San Diego). The contents of Chapter 5 were written by myself to be submitted as a methods chapter in a book called, Adhesion Protein Protocols (3rd ed.). The contribution from Brad Zuchero is not included in Chapter 5. The unpublished results in the Chapter 6 resulted from a short term collaboration with Frank Gertler (MIT).

Table of Contents

Preface	Copyright.....ii
	Acknowledgementsiii
	Abstract.....v
	Contributions.....vi
	Table of Contents.....vii
	List of Tables.....viii
	List of Figures.....ix
Chapter 1	Introduction.....1
Chapter 2	VASP is a processive barbed end polymerase.....21
Chapter 3	Modulation of Ena/VASP barbed end processivity by a membrane tethered actin binding protein.....85
Chapter 4	A Mechanistic Framework for Actin Cytoskeleton Reorganization by α -Catenin at Cell-Cell Contacts.....145
Chapter 5	Single actin filament TIRF assay.....185
Chapter 6	Unpublished experiments and results.....206
Appendix A	Permissions.....218

List of Tables

Chapter 3

Table 1:	Defining the actin binding domain of Lamellipodin.....	144
----------	--	-----

List of Figures

Chapter 2

F1: Cy3-KCK-hVASP ^{CCC-SSA} and unlabeled hVASP are functionally equivalent.....	73
F2: Mechanisms regulating the interaction between VASP and filamentous actin.....	74
F3: Mechanism for VASP barbed end capture.....	75
F4: Processivity of barbed end associated VASP tetramers.....	76
F5: VASP enhances barbed end polymerization in the presence of profilin-actin.....	77
F6: VASP antagonizes capping protein barbed end association in the presence of profilin-actin.....	78
F7: Model for VASP barbed end association.....	79
SF1: Cy3-VASP GAB and FAB domain mutants.....	80
SF2: Salt dependence of Cy3-VASP actin filament binding, barbed end polymerization, and anti-capping.....	81
SF3: Cy3-VASP C-terminal fragment does not capture barbed ends.....	82
SF4: Nucleotide dependence of VASP binding to filamentous actin.....	83
SF5: Localization of Cy3VASP during actin filament bundling.....	84

Chapter 3

F1: Lamellipodin localizes to the barbed end attachment zone in the absence of VASP.....	132
--	-----

F2:	Lamellipodin is an actin binding protein.....	133
F3:	Lamellipodin can simultaneously bind to filamentous actin and the VASP EVH1 domain.....	134
F4:	Lamellipodin C-terminal domain binds to filamentous actin <i>in vivo</i>	135
F5:	Lamellipodin enhances VASP barbed end processivity by a clustering independent mechanism.....	136
F6:	ActA and Lamellipodin enhance VASP processivity by distinct mechanisms	137
F7:	Model for Lamellipodin mediated Ena/VASP barbed end processivity...	138
SF1:	Actin based motility on lipid coated glass beads.....	139
SF2:	Sequence of the Lamellipodin actin binding domain.....	140
SF3:	Parameters that regulate Lamellipodin actin filament binding <i>in vitro</i>	141
SF4:	Sedimentation equilibrium to determine stoichiometry of VASP-Lpd interaction.....	142
SF5:	Lamellipodin interaction with Ena/VASP protein requires FPPPP motif and EVH1 domain.....	143

Chapter 4

F1:	α E-catenin ABD binds cooperatively to F-actin.....	177
F2:	Electron cryo-microscopy and 3D reconstructions of actin filaments in the presence of α E-catenin actin-binding domain (ABD).....	178
F3:	α E-catenin ABD reduces barbed end polymerization.....	179
F4:	α E-catenin inhibits Arp2/3 complex branching.....	180

F5:	α E-catenin inhibits cofilin severing.....	181
SF1:	α E-catenin binds cooperatively to filamentous actin.....	182
SF2:	α E-catenin ABD reduces barbed end polymerization.....	183
SF3:	Localization GFP α E-catenin ABD during actin filament bundling.....	184

Chapter 5

F1:	Extinction coefficients for maleimide fluorophore.....	204
F2:	Cartoon for construction of TIRF flow cells.....	204
F3:	Schematic for glass surface chemistry, pegylation, and actin filament attachment in the TIRF flow cells.....	205
F4:	Imaging dynamic actin filament assembly by TIRF microscopy.....	205

Chapter 6

F1:	VASP does not modulate mDia2 polymerase activity.....	214
F2:	mDia2 interacts with VASP.....	215
F3:	Single molecule imaging of barbed end associated SNAP-Alexa488-mDia2.....	216
F4:	Actin filament bundling by fascin.....	217

Chapter 1

Introduction

Scott D. Hansen and R. Dyche Mullins

In preparation for Current Opinions in Molecular Biology

Introduction

i. Innovations

Recent innovations in structural biology have dramatically improved our understanding of actin filament architecture and the ways in which regulatory proteins modulate it. The atomic structure of monomeric actin was solved in 1980 but, unfortunately, no one has ever crystallized actin packed in a configuration that approximates a canonical filament. Consequently, the best actin filament models derive from a combination of electron microscopy and image reconstruction, usually exploiting helical filament symmetry to maximize resolution (Behrmann et al., 2012). New methods of sample preparation have now pushed the resolution of the best actin filament models significantly below ten Angstroms while new image analysis techniques have revealed conformational heterogeneity and plasticity in actin filaments (Oda et al., 2009; Murakami et al., 2010; Fujii et al., 2010). In addition, higher resolution cryo-electron microscopy structures of actin binding proteins has provided insight about the different modes of actin filament binding.

Much of our understanding of actin dynamics comes from studying the bulk properties of actin-containing solutions. Early investigators, for example, followed filament assembly using flow birefringence. Later work made use of light scattering or fluorescence of environmentally sensitive dyes coupled to actin to follow the kinetics of filament assembly. Assays like these remain important — in part because they are easy to perform — but they provide much less information compared to methods based on imaging individual filaments. The first single-

filament studies of actin dynamics compared snapshots, taken at different times, of fixed samples imaged by electron microscopy (Pollard, 1986). Then, twenty years ago, improvements in the optics of light microscopes and sensitivity of CCD cameras made it possible to image single growing and shortening filaments. Recent technical innovations have revolutionized such single filament studies. These include: (1) the use of TIRF microscopy (Breitsprecher et al., 2009), (2) improved passivation of glass surfaces (Hermanson, 1996; Bieling et al., 2009), (3) improved methods for immobilizing proteins, and (4) rapid switching of buffer components and protein concentrations using microfluidics (Jegou et al., 2011). With an increased availability of synthetic fluorophores and improved single molecule imaging techniques, multicolor TIRF-M has also provided a platform for visualizing the assembly and disassembly of filamentous actin with high spatial and temporal resolution *in vitro*.

ii. Actin nucleators

In 1998, Mullins et al. reported that the Arp2/3 complex can nucleate an actin filament from the side of an existing mother filament to generate a branch. From this discovery emerged the dendritic actin nucleation model, which provided a mechanism to explain how non-muscle cells build and organize actin filaments during cell migration (Pollard et al., 2001; Pollard and Borisy, 2003). Although the minimal requirements for activation of the Arp2/3 complex were determined more than a decade ago, there is still an incomplete understanding of

how coincident signals activate the Arp2/3 complex and which steps in the nucleation cycle are rate limiting.

Defining the Arp2/3 nucleation pathway. For several years, GST tagged NPFs have anecdotally been known to potently activate the Arp2/3 complex in pyrene actin polymerization assays. Padrick et al. (2008) systematically characterized this phenomenon and determined that dimeric WASP binds 1:1 with the Arp2/3 complex in solution. Recently, the location of the two NPF binding sites were partially mapped (Padrick et al., 2011; Ti et al., 2011; Xu et al., 2012). Using tandem NPFs (i.e. $VCA_{(GGS)_4}VCA$), Padrick et al. (2011) mapped the C domain binding sites on the Arp2/3 complex by chemical cross-linking. The use of the Arp2/3 binding protein, cortactin, to block one of the VCA binding sites during the cross-linking experiments was critical to unambiguously define these binding sites. Although the affinities for the two NPF binding sites differ by >100-fold in solution, they appear to be regulated by mother filament binding in both a positive and negative manner.

Cryo-electron microscopy structures of the Arp2/3 complex with bound NPF show that the high affinity CA domain interaction sterically clashes with the mother actin filament binding face on the Arp2/3 complex (Xu et al., 2012). Ti et al. (2011) found that the CA domain binds more tightly to the Arp2/3 complex in solution compared to Arp2/3 bound to filamentous actin. Supporting these observations, VCA cross-linked to the pointed-end side of Arp2 (i.e. high affinity NPF binding site) inhibits mother filament attachment and nucleation (Ti et al., 2011). Conversely, actin filament binding is hypothesized to strengthen the low

affinity NPF interaction. Based on the different binding modes of the CA domain to the Arp2/3 complex, each NPF is hypothesized to execute a distinct step in the nucleation pathway.

How is actin monomer delivery to the Arp2/3 complex coordinated with NPF and mother filament binding? Padrick et al. (2011) found that maximal activation of the Arp2/3 complex requires the delivery of two actin monomers by two NPFs. Based on the following results, each NPF binding event is likely to cause conformational and affinity changes throughout the Arp2/3 nucleation cycle: (1) cross-linked actin-VCA binds more tightly to Arp2/3 in the presence of filamentous actin, (2) cross-linked actin-VCA is a weak Arp2/3 activator, and (3) mother filament binding weakens the interaction between VCA bound to the high affinity site (Ti et al., 2011). Since the low affinity VCA interaction occurs on the barbed end face of the Arp2/3 complex and is compatible with mother filament binding, this NPF could be primed for delivery of an additional actin monomer.

There are still several unanswered questions regarding the Arp2/3 nucleation pathway. For example, we still do not know which steps in the pathway are rate limiting. Fortunately, many of the binding steps have been identified and there are mutants that can be used to trap transition states in the nucleation pathway. Using these reagents, single molecule TIRF microscopy experiments should provide the resolution to further dissect the Arp2/3 nucleation pathway. However, imaging fluorescently labeled Arp2/3 and NPFs will be challenging for the following reasons: (1) chemically labeling the Arp2/3 complex with amine or thiol reactive fluorophore can compromise the nucleation activity,

(2) recombinant Sf9 cell expression of the seven subunit Arp2/3 complex is non-trivial, and (3) nucleation promoting factors are unstructured positively charged proteins that have many non-specific interactions *in vitro*. The third challenge regarding the difficulties of handling the NPFs in single molecule assay might be remedied by using different NPFs or minimal protein fragments. This will require identifying new NPFs and characterizing how they activate the Arp2/3 complex.

Improvements in protein homology based identification have recently led to the discovery of several nucleation promoting factors (NPFs) that contain single or tandem Wiskott-Aldrich syndrome protein homology 2 (WH2) domains (i.e. WHAMM, WASH, and JMY1). Unique amongst the NPFs is the multifunctional actin nucleator, JMY1. Similar to the actin nucleator, SPIRE, JMY1 contains tandem WH2 domains that can bind multiple actin monomers and autonomously nucleate actin filaments (Zuchero et al., 2009). Common to NPFs, JMY1 contains a central (C) and acidic (A) domain that can bind and activate the Arp2/3-complex. Unlike most NPFs, full length JMY1 is not auto-inhibited *in vitro*, nor has it been found to interact with a regulatory complex. *In vivo*, JMY1 activity is thought to be regulated by shuttling between the nucleus and the cytoplasm (Zuchero et al., 2012). Localization of JMY1 is dependent in part on two nuclear localization sequences (NLS) that overlap with two WH2 domains (Zuchero et al., 2012). Depending on the cellular concentration of monomeric actin and the occupancy of the WH2 domains, JMY1 predominantly localizes in either the cytoplasm or the nucleus. Identifying the protein interactions that regulate the subcellular localization and the nucleation activity of JMY1 will be

required for determining the significance of the Arp2/3 activating versus the autonomous actin nucleation activity in cells.

iii. Actin barbed end polymerases

A second class of actin nucleators that regulate the formation of linear unbranched actin filaments are formins (Pruyne et al., 2002; Sagot et al., 2002). Mammals express 15 different formin proteins, each of which is likely to regulate the formation of a distinct actin filament structure (Schonichen et al., 2010). This model is strongly supported by genetic studies in *S. pombe*, showing the three different formin proteins function to build either the cytokinetic ring, actin cables, or actin patches (Scott et al., 2011). Furthermore, formins have been shown to localize and interact with proteins that targeted to a variety of organelles. Although the mechanism of formin dependent actin nucleation remains unknown, formins are known to function as highly processive actin barbed end polymerases. Initially, Kovar et al. (2003) proposed that formins function as processive barbed end capping proteins. Supporting this model, Kovar et al. (2003) demonstrated that filaments nucleated by either formins or capping protein were unable to anneal at their barbed ends. Furthermore, the actin filament length distribution of for actin polymerized in the presence of formins and capping protein are nearly identical. Romero et al. (2004) proposed an alternative model and suggested that formin barbed end elongation requires ATP hydrolysis. This model suggested that the barbed end processivity is an energy consuming process and that formins function similar to myosin motors.

Although Romero et al. (2004) were the first to show that formins remain processively attached to growing actin filament barbed ends in the presence of profilin-actin, their model was later challenged by Kovar et al. (2006) who found that formins are processive polymerases in the presence of either ADP-actin and ATP-actin. Much of the debate regarding the mechanism of formin polymerase activity stemmed from the different formin activities observed in the of actin alone or profilin-actin.

Formins are structurally conserved and are considered to be auto-inhibited *in vivo* (Otomo et al., 2010). Formin activation is regulated by RhoGTPases, lipids, microtubules, and a host of other protein interaction. Structurally, formins consist of a conserved homodimeric FH2 domain which forms a ring-like structure that can processively track elongating actin filament barbed ends (Xu et al., 2004). The rate of formin mediated barbed end polymerization is strongly influenced by the FH1 domain, which contains long stretches of unstructured proline residues that function to recruit the actin monomer binding protein, profilin (Paul et al., 2008). Recently, Courtemanche et al. (2012) showed that across formin families there is a strong correlation between the profilin binding affinity and the position of the poly-proline stretch relative to the FH2 domain. Poly-proline stretches closest to the FH2 domain have the weakest affinity for profilin, while those distant to the FH2 domain bind more tightly to profilin. The architecture of the FH1 domain further supports a model in which profilin-actin is directly transferred by the formin to the barbed end and not simply from solution.

Currently, profilin-actin are the only proteins that have been shown to modulate the formin barbed end processivity.

The Ena/VASP protein family represents a unique class of tetrameric proteins that regulate the elongation of actin filament barbed ends. Unlike the formin protein family, Ena/VASP proteins do not nucleate actin filaments. Similar to formins and nucleation promoting factors (NPFs), Ena/VASP proteins contain a poly-proline domain and WH2-like motif that interact with profilin and monomeric actin respectively. Although these interactions were identified more than a decade ago, the mechanism by which these domains collaborate to promote actin filament assembly has eluded researchers. By imaging the dynamic assembly of single actin filaments *in vitro*, Ena/VASP proteins were unambiguously shown to enhance barbed end filament elongation (Breitsprecher et al., 2008; Hansen and Mullins, 2010). Breitsprecher et al. (2011) found that the rate of Ena/VASP mediated barbed end elongation *in vitro* is dependent on the affinity for monomeric actin. Although all Ena/VASP proteins are predicted to converge on the same maximal rate of filament assembly *in vivo*, differences in the affinity for monomeric actin result in different actin filament elongation rates *in vitro*. Single molecule imaging revealed that Ena/VASP proteins can bind to the sides of actin filaments, diffuse, and capture growing actin filament barbed ends in the presence of monomeric actin or profilin-actin (Hansen and Mullins, 2010). Although weakly processive compared to the formin family of actin polymerases, single VASP tetramers can surf on growing barbed ends for ~ 1.5 seconds *in vitro* (Hansen and Mullins, 2010).

How does a weakly processive actin barbed end polymerase antagonize a high affinity barbed end capping protein? Capping protein and Ena/VASP proteins antagonize each other *in vivo* (Bear et al., 2002; Mejillano et al., 2004). Depending on the relative concentrations of each proteins, strikingly different actin network architectures can be generated (i.e. lamellipodia and filopodia). *In vitro*, capping protein binds to actin filament barbed ends with a sub-nanomolar affinity and a dwell time of nearly 30 minutes (Kuhn and Pollard, 2007). Conversely, VASP transiently associates with growing barbed ends with a K_d of 9 nM (Hansen and Mullins, 2010). Compared to capping protein however, VASP captures barbed ends significantly faster. Similar to microtubule associated proteins of the MCAK and XMAP215 protein families (Brouhard et al., 2008), the ability of Ena/VASP proteins to bind and diffuse along actin filaments allows them to target filament ends faster than would be predicted for a diffusion limited process; this is especially true over short distances. Diffusion allows Ena/VASP proteins to explore the filament lattice more rapidly than would be possible by ATP-dependent directed transport.

Clustering multiple Ena/VASP proteins provides a second mechanism for antagonizing capping protein barbed end attachment. *In vivo*, Ena/VASP proteins localize to the plasma membrane where they promote actin filament elongation. High local membrane concentrations of Ena/VASP can result in the formation of filopodial actin based membrane protrusions, which are void of capping protein (Svitkina et al., 2003). Breitsprecher et al. (2008) demonstrated that single actin filaments can processively elongate from surfaces coated with high densities of

Ena/VASP proteins in the presence of capping protein. Processive filament attachment was dependent on the Ena/VASP WH2 domain, suggesting that clustered WH2 domains drive processive filament attachment. In other words, clustering weakly processive barbed end polymerases increasing the collective barbed end processivity.

How processive are Ena/VASP proteins *in vivo*? Cell biology experiments suggest that a combination of free actin filament barbed ends and a membrane tethered binding partner (e.g. Lamellipodin, RIAM, integrins) are required for sustained membrane localization of VASP (Krause *et al.*, 2005; Lacayo *et al.*, 2007; Neel *et al.*, 2009). Single molecule imaging of GFP-VASP revealed that molecules dwell at the leading edge of lamellipodial protrusions for 5-8 seconds (Miyoshi *et al.*, 2006 JCB). Consistent with this observation, photobleaching experiments have shown that membrane associated GFP tagged Ena/VASP recovers on the order of 8-17 seconds (Applewhite *et al.*, 2006; Lai *et al.*, 2008; Vitriol *et al.*, 2007). How Ena/VASP proteins are recruited to the plasma membrane and how their binding partners regulate the lifetime, density, and actin barbed end polymerase activity remains unknown.

iv. Signaling and actin network assembly

More than a decade ago, dendritic actin network assembly was reconstituted *in vitro* using polystyrene beads coated with the *Listeria* protein, ActA, plus six additional proteins that were known to regulate actin assembly in eukaryotic cells (Loisel *et al.*, 1999). Because the majority of pathogenic proteins

that promote actin assembly function in a constitutive manner (i.e. ActA, Sca2, EspF_U), the complex regulation required to generate actin networks in eukaryotic cells can be bypassed. For example, enterohemorrhagic *E. coli* (EHEC) can inject the EspF_U protein into eukaryotic cells, where it binds multiple N-WASP proteins and bypasses the Cdc42/PIP₂ regulation that is normally required for N-WASP dependent actin assembly (Sallee et al., 2008; Cheng et al. 2008). Dissecting the structure and function relationships of these pathogenic proteins has given us insight about the mechanism of NPF autoinhibition, activation, and molecular mimicry by pathogenic proteins. However, few advances have been made in reconstituting the complexity of RhoGTPase dependent actin assembly that is thought to occur to actin based membrane protrusions.

Recently, several groups have made conceptual advances concerning the autoregulation of the WAVE complex and the activation mechanism. First, both recombinant and natively purified WAVE complex are auto-inhibited and require multiple inputs (i.e. Rac1 GTPase, PI(3,4,5)P₃, IRSp53) for activation (Ismail et al., 2009; Lebensohn et al., 2009; Chen et al., 2010). In the case of the natively purified WAVE2 complex, phosphorylation of the WAVE2 complex is also required for Rac2-GTP and PIP₃ to function as activators (Lebensohn et al., 2009). Although several activators and effectors of the WAVE complex have been identified, there is still no consensus as to which factors are required to reconstitute WAVE based actin network assembly *in vitro*. Previous studies have reported that micro-molar concentrations of Rac1 GTPases are required for activation of the WAVE complex (Ismail et al., 2009). This observation suggested

that another GTPase or signaling molecule may be required to activate the WAVE complex. Recently, Koronakis et al. (2011) reported on the signaling landscape for actin networks that were assembled in the presence of different lipid membrane compositions. By using mass-spectrometry based protein identification, they discovered that Rac1 GTPase synergizes with Arf1 GTPase to promote WAVE complex dependent actin assembly in brain extract. By adding dominant negative fragments to the bead motility assay they were able to cripple specific arms the actin assembly pathway to determine the contribution of Cdc42, Rac1, and Arf1 GTPase to network assembly. Consistent with previous reports, Koronakis et al. (2011) found that the Cdc42/N-WASP and Rac1/Arf1/WAVE nucleation pathways are mediated by either PIP₂ or PIP₃ lipids respectively. Although PIP₃ has been implicated in regulating WAVE complex activity, it remains unclear whether the mechanism is strictly for membrane localization or allosteric regulation of the WAVE complex.

The challenge moving forward is building a unifying model to describe WAVE complex dynamics and regulation based on the plethora of cell biological, genetic, and biochemical data. Although N-WASP/Cdc42 and WAVE/Rac1 are likely to function as the core regulators of their respective nucleation pathways, we will continue to find new modulators of these pathways (i.e. GAPs and GEFs) that are expressed in a tissue specific manner and regulate these GTPases in combinatorial fashion.

v. Frontiers

Protein interactions between signaling molecules and actin cytoskeleton at the plasma membrane are intrinsically weak. This is evident from single molecule and speckle microscopy studies of the actin cytoskeleton, which show that dendritic actin networks are rapidly assembled and disassembled on the order of seconds in cells (Iwasa and Mullins, 2006). From these studies it has become evident that the single actin filament TIRF-M assay can only be used to explore a limited range of actin monomeric concentrations. Furthermore, not all actin binding proteins are suitable for single molecule characterization due to weak affinities for filamentous actin and *in vitro* assay buffer incompatibilities. These limitations require researchers to develop new assays for characterizing actin binding proteins and the signaling proteins that regulate their activity. Reconstitution of signaling pathways on supported lipid bilayers provides one method of increasing the local protein concentration. In addition, many proteins that regulate actin network assembly interact directly with phospholipids; this interaction can be required for activation in addition to localization. Ideally, reconstitutions of the actin cytoskeleton on membranes will allow researchers to characterize how the spatial localization of proteins is regulated by positive feedback loops and coincident signals.

References

- Applewhite, D.A., M. Barzik, S. Kojima, T.M. Svitkina, F.B. Gertler, and G.G. Borisy. Ena/VASP proteins have an anti-capping independent function in filopodia formation. *Mol. Biol. Cell.* 2007, 18, 2579-2591.
- Bear, J.E., T.M. Svitkina, M. Krause, D.A. Schafer, J.J. Loureiro, G.A. Strasser, I.V. Maly, O.Y. Chaga, J.A. Cooper, and G.G. Borisy. 2002. Antagonism between Ena/VASP proteins and actin filament capping regulates fibroblast motility. *Cell.* 109, 509-521.
- Behrmann E, Tao G, Stokes DL, Egelman EH, Raunser S, Penczek PA. Real-space processing of helical filaments in SPARX. *J Struct Biol.* 2012, Feb;177(2):302-13.
- Bieling, P., Telley, I.A., Hentrich, C., Piehler, J., and T. Surrey. Fluorescence Microscopy Assays on Chemically Functionalized Surfaces for Quantitative Imaging of Microtubule, Motor, and +TIP Dynamics. *Methods in Cell Biology.* 2010. v.95.
- Breitsprecher D, Kieseewetter AK, Linkner J, Vinzenz M, Stradal TE, Small JV, Curth U, Dickinson RB, Faix J. Molecular mechanism of Ena/VASP-mediated actin-filament elongation. *EMBO J.* 2011, Feb 2;30(3):456-67.
- Breitsprecher D, Kieseewetter AK, Linkner J, Urbanke C, Resch GP, Small JV, Faix J. Clustering of VASP actively drives processive, WH2 domain-mediated actin filament elongation. *EMBO J.* 2008, Nov 19;27(22):2943-54.
- Breitsprecher D, Kieseewetter AK, Linkner J, Faix J. Analysis of actin assembly by in vitro TIRF microscopy. *Methods Mol Biol.* 2009, 571:401-15.
- Brouhard, G.J., J.H. Stear, T.L. Noetzel, J. Al-Bassam, K. Kinoshita, S.C. Harrison, J. Howard, A.A. Hyman. XMAP215 is a processive microtubule polymerase. *Cell.* 2008, 132: 79-88.
- Chen Z, Borek D, Padrick SB, Gomez TS, Metlagel Z, Ismail AM, Umetani J, Billadeau DD, Otwinowski Z, Rosen MK. Structure and control of the actin regulatory WAVE complex. *Nature.* 2010, Nov 25;468(7323): 533-8.
- Cheng HC, Skehan BM, Campellone KG, Leong JM, Rosen MK. Structural mechanism of WASP activation by the enterohaemorrhagic E. coli effector EspF(U). *Nature.* 2008, Aug 21;454(7207):1009-13.

Co C, Wong DT, Gierke S, Chang V, Taunton J. Mechanism of actin network attachment to moving membranes: barbed end capture by N-WASP WH2 domains. *Cell*. 2007, Mar 9;128(5):901-13.

Courtemanche, N. and T.D. Pollard. Determinants of formin homology 1 (FH1) domain function in actin filament elongation by formins. *J. Bio. Chem.* 2012, 287(10): 7812-7820.

Fujii, T., A.H. Iwane, T. Yanagida, and K. Namba. Direct visualization of secondary structures of F-actin by electron cryomicroscopy. *Nature*. 2010. 467: 724-729.

Hansen, S.D. and R.D. Mullins. VASP is a processive actin polymerase that requires monomeric actin for barbed end association. *J Cell Biol.* 2010. Nov 1;191(3):571-84.

Hermanson, G.T. Bioconjugate Techniques. San Diego: Academic Press (pp. 266-272). (Product # 20002T). 1996.

Ismail, A.M., S.B. Padrick, B. Chen, J. Umetani, and M.K. Rosen. The WAVE regulatory complex is inhibited. *Nature Structural & Molecular Biology*. 2009. 16(5): 561-563.

Iwasa, J.H. and R.D. Mullins. Spatial and temporal relationships between actin-filament nucleation, capping, and disassembly. *Curr. Bio.* 2007, 17(5): 395-406.

Jégou A, Niedermayer T, Orban J, Didry D, Lipowsky R, Carlier MF, Romet-Lemonne G. Individual actin filaments in a microfluidic flow reveal the mechanism of ATP hydrolysis and give insight into the properties of profilin. *PLoS Biol.* 2011 Sep;9(9):e1001161.

Jégou A, Carlier MF, Romet-Lemonne G. Microfluidics pushes forward microscopy analysis of actin dynamics. *Bioarchitecture*. 2011 Nov 1;1(6):271-276.

Koronakis, V., P.J. Hume, D. Humphreys, T. Lui, O. Horning, O.N. Jensen, and E.J. McGhie. WAVE regulatory complex activation by cooperating GTPases Arp and Rac1. *Proc Natl Acad Sci USA*. 2011. 108(35): 14449-14454.

Kovar, D.R., J.R. Kuhn, A.L. Tichy, and T.D. Pollard. The fission yeast cytokinesis formin Cdc12p is a barbed end actin filament capping protein gated by profilin. *Journal Cell Biology*. 2003. 161(5): 875-887.

Kovar, D.R., E.S. Harris, R. Mahaffy, H.N. Higgs, and T.D. Pollard. 2006. Control of the assembly of ATP- and ADP-actin by formins and profilin. *Cell*. 124: 423–435.

- Krause, M., J.D. Leslie, M. Stewart, E.M. Lafuente, F. Valderrama, R. Jagannathan, G.A. Strasser, D.A. Rubinson, H. Liu, and M. Way. 2004. Lamellipodin, an Ena/VASP ligand, is implicated in the regulation of lamellipodial dynamics. *Dev. Cell.* 7, 571-583.
- Kuhn, J.R. and T.D. Pollard. Single Molecule Kinetic Analysis of Actin Filament Capping. *J. Bio. Chem.* 2007. 282(38):28014-28024.
- Lacayo, C.I., Z. Pincus, M.M. VanDuijn, C.A. Wilson, D.A. Fletcher, F.B. Gertler, A. Mogilner, and J.A. Theriot. Emergence of large-scale cell morphology and movement from local actin filament growth dynamics. *PLoS Biol.* 2007. 5,e233.
- Lai, F.P., M. Szczodrak, J. Block, J. Faix, D. Breitsprecher, H.G. Mannherz, T.E. Stradal, G.A. Dunn, J.V. Small, and K. Rottner. Arp2/3 complex interactions and actin network turnover in lamellipodia. *EMBO.* 2008. 27: 982-992.
- Lebensohn, A.M. and M.W. Kirschner. Activation of the WAVE complex by coincident signals controls actin assembly. *Molecular Cell.* 2009, 36, 512-524.
- Li P, Banjade S, Cheng HC, Kim S, Chen B, Guo L, Llaguno M, Hollingsworth JV, King DS, Banani SF, Russo PS, Jiang QX, Nixon BT, Rosen MK. Phase transitions in the assembly of multivalent signalling proteins. *Nature.* 2012. Mar 7;483(7389):336-40.
- Loisel, T.P., R. Boujemaa, D. Pantaloni, and M. Carlier. Reconstitution of actin-based motility of *Listeria* and *Shigella* using pure proteins. *Nature.* 1999. 401: 613-615.
- Mejillano, M.R., S. Kojima, D.A. Applewhite, F.B. Gertler, T.M. Svitkina, and G.G. Borisy. Lamellipodial versus Filopodial mode of the actin nanomachinery: Pivotal role of the filament barbed end. *Cell.* 2004. v118:363-373.
- Miyoshi, T., T. Tsuji, C. Higashida, M. Hertzog, A. Fujita, S. Narumiya, G. Scita, and N. Watanabe. Actin turnover-dependent fast dissociation of capping protein in the dendritic nucleation actin network: evidence of frequent filament severing. *J. Cell Biol.* 2006. 175(6):947-955.
- Mullins, R.D., J.A. Heuser, and T.D. Pollard. The interaction of Arp2/3 complex with actin - Nucleation, high affinity pointed end capping, and formation of branching networks of filaments. *Proc Natl Acad Sci U S A.* 1998. 95: 6181-6186.
- Murakami, K., T. Yasunaga, T.Q. Noguchi, Y. Gomibuchi, K.X. Ngo, T.Q. Uyeda, and T. Wakabayashi. Structural basis for actin assembly, activation of ATP hydrolysis, and delayed phosphate release. *Cell.* 2010. 143: 275-287.

Neel, N.F., M. Barzik, D. Raman, T. Sobolik-Delmaire, J. Sai, A.J. Ham, R.L. Mernaugh, F.B. Gertler, and A. Richmond. VASP is a CXCR2-interacting protein that regulates CXCR2-mediated polarization and chemotaxis. *J. Cell Sci.* 2009. 122: 1882-1894.

Oda T, Iwasa M, Aihara T, Maeda Y, Narita A. The nature of the globular- to fibrous-actin transition. *Nature.* 2009. Jan 22;457(7228):441-5.

Otomo, T., D.R. Tomchick, C. Otomo, M. Machius, and M.K. Rosen. Crystal structure of the formin mDia1 in autoinhibited conformation. *PLoS.* 2010. 5(9): e12896.

Padrick SB, Doolittle LK, Brautigam CA, King DS, Rosen MK. Arp2/3 complex is bound and activated by two WASP proteins. *Proc Natl Acad Sci U S A.* 2011. Aug 16;108(33):E472-9.

Paul, A. and T. Pollard. The Role of the FH1 Domain and Profilin in Formin-Mediated Actin-Filament Elongation and Nucleation. *Curr. Bio.* 2008. 18: 9-19.

Pollard, T.D. Rate constants for the reactions of ATP- and ADP-actin with the ends of actin filaments. *Journal of Cell Biology.* 1986. 103(6): 2747-2754.

Pollard, T.D., L. Blanchoin, and R.D. Mullins. Actin dynamics. *J. Cell Sci.* 2001. 114, 3-4.

Pollard, T.D. and G.G. Borisy. Cellular motility driven by assembly and disassembly of actin filaments: integration of signals to the Arp2/3 complex. *Cell.* 2003. 112, 453-465.

Pruyne, D., M. Evangelista, C. Yang, E. Bi, S. Zigmund, A. Bretscher, and C. Boone. Role of formins in actin assembly- nucleation and barbed-end association. *Science.* 2002. 297: 612-615.

Reymann AC, Boujemaa-Paterski R, Martiel JL, Guerin C, Cao W, Chin HF, De La Cruz EM, Thery M, Blanchoin L. Actin network architecture can determine myosin motor activity. *Science.* 2012 Jun 8;336(6086):1310-4.

Reymann AC, Suarez C, Guerin C, Martiel JL, Staiger CJ, Blanchoin L, Boujemaa-Paterski R. Turnover of branched actin filament networks by stochastic fragmentation with ADF/cofilin. *Mol Biol Cell.* 2011 Jul 15;22(14):2541-50.

Romero, S. , C.L. Clainche, D. Didry, C. Egile, D. Pantaloni, and M. Carlier. Formin is a processive motor that requires profilin to accelerate actin assembly and associated ATP hydrolysis. *Cell.* 2004. 119: 419-429.

Sagot, I., A.A. Rodal, J. Moseley, B.L. Goode, and D. Pellman. An actin nucleation mechanism mediated by Bni1 and profilin. *Nat. Cell Bio.* 2002. 4: 626-631.

Salje J, van den Ent F, de Boer P, Lowe J. Direct membrane binding by bacterial actin MreB. *Molecular Cell.* 2011 Aug 5;43(3):478-87.

Sallee, N.A., G.M. Rivera, J.E. Dueber, D. Vasilescu, R.D. Mullins, B.Y. Mayer, and W.A. Lim. The pathogen protein EspFU hijacks actin polymerization using mimicry and multivalency. *Nature.* 2008, 454(7207): 1005-1008.

Schonichen, A. and M. Geyer. Fifteen formins for an actin filament: A molecular view on the regulation of human formins. *Biochimica et Biophysica Acta.* 2010. 152-163.

Scott, B.J., E.M. Neidt, and D.R. Kovar. The functionally distinct fission yeast formins have specific actin-assembly properties. *Mol. Bio. Cell.* 2011.

Svitkina, T.M., E.A. Bulanova, O.Y. Chaga, D.M. Vignjevic, S. Kojima, J.M. Vasiliev, and G.G. Borisy. 2003. Mechanism of filopodia initiation by reorganization of a dendritic network. *J. Cell Biol.* v160(3): 409-421.

Thoresen T, Lenz M, Gardel ML. Reconstitution of contractile actomyosin bundles. *Biophys J.* 2011, 100(11): 2698-705.

Ti, S., C.T. Jurgenson, B.J. Nolan, and T.D. Pollard. Structural and biochemical characterization of two binding sites for nucleation-promoting factor WASp-VCA on Arp2/3 complex. *Proc Natl Acad Sci U S A.* 2011.

Vitriol, E.A., A.C. Uetrecht, F. Shen, K. Jacobson, and J.E. Bear. 2007. Enhanced EGFP-chromophore-assisted laser inactivation using deficient cells rescued with functional EGFP-fusion proteins. *PNAS.* 104(16): 6702-6707.

Xu, Y., J.B. Moseley, I. Sagot, F. Poy, D. Pellman, B.L. Goode, and M.J. Eck. Crystal structures of a Formin Homology-2 domain reveal a tethered dimer architecture. *Cell.* 2004. 116: 711-723.

Xu, X., I. Rouiller, B.D. Slaughter, C. Egile, E. Kim, J.R. Unruh, X. Fan, T.D. Pollard, R. Li, D. Hanein, and N. Volkman. Three-dimensional reconstructions of Arp2/3 complex with bound nucleation promoting factors. *EMBO Journal.* 2012, 31: 236-247.

Zuchero, J.B., A.S. Coutts, M.E. Qianlan, N.B. La Thangue, and R.D. Mullins. P53-cofactor JMY is a multifunctional actin nucleation factor. *Nat. Cell Bio.* 2009.

Zuchero, J.B., B. Belin, and R.D. Mullins. Actin binding to WH2 domains regulates nuclear import of the multifunctional actin regulator JMY. *Mol. Cell Bio.* 2012. 23: 853-863.

Chapter 2

VASP is a processive actin polymerase that requires monomeric actin
for barbed end association

Scott D. Hansen and R. Dyche Mullins

Published: Nov. 1, 2010, *Journal of Cell Biology*, 191(3):571-84.

Abstract

Ena/VASP proteins are essential regulators of the actin cytoskeleton during cell migration and morphogenesis and they promote assembly of both filopodial and lamellipodial actin networks. To understand the molecular mechanisms underlying their cellular functions we used Total Internal Reflection Fluorescence microscopy to visualize fluorescent VASP tetramers interacting with static and growing actin filaments in vitro. These experiments revealed multiple filament binding modes: (1) static side binding, (2) side binding with 1-dimensional diffusion, and (3) processive barbed end tracking. Actin monomers antagonize side binding but promote high-affinity ($K_d = 9$ nM) barbed end binding. In low ionic strength buffers VASP tetramers deliver multiple actin monomers to a growing barbed end before dissociating. In higher ionic strength buffers VASP requires profilin for effective polymerase activity. Although single VASP tetramers are weakly processive ($K_{off} = 0.69$ sec⁻¹), they effectively antagonize capping protein barbed end association. Based on our observations, we propose a mechanism that accounts for all three binding modes and provides a model for how VASP promotes actin filament assembly.

Introduction

Assembly of actin filament networks drives many fundamental cellular processes, including: cell polarization and migration, endocytosis, intracellular trafficking, and maintenance of membrane-bounded compartments. The functions of these different actin networks are determined in part by differences in their localization, composition, and architecture (Fletcher and Mullins, 2010). These basic properties are, in turn, specified by proteins that regulate the assembly and crosslinking of actin filaments (Pollard *et al.*, 2001; Welch and Mullins, 2002). Two important and widely studied actin-based structures -- lamellipodia and filopodia -- are assembled at the leading edge of motile cells and play important roles in directed cell migration. Lamellipodia are three dimensional, space-filling networks that resist deformation and generate forces that advance the cell membrane (Pollard and Borisy, 2003), while filopodia are parallel bundles of actin filaments required for sensing chemical gradients and interacting with appropriate cellular targets (Alder *et al.*, 2006). The filaments in a lamellipodial actin network are kept short because their growth is rapidly terminated by capping protein (Iwasa and Mullins, 2007; Akin and Mullins, 2008). The molecular dynamics of filopodia are not well understood but they appear, at least in some cases, to arise from a subset of lamellipodial filaments that first increase in length and then become highly aligned and tightly crosslinked (Mejillano *et al.*, 2004; Mogilner and Rubinstein, 2005; Svitkina *et al.*, 2003). The increase in filament length required for lamellipod to filopod transitions could be caused by faster filament elongation or by delayed filament capping. In vivo,

these transitions are important for many processes, including neurite outgrowth, tumor metastasis, and chemotaxis.

One set of factors that modulates the architecture of lamellipodial networks and promotes their reorganization into filopodia is the Ena/VASP family of proteins. The first member of this family to be described was VASP (VAsodilator-Stimulated Phosphoprotein), a human protein originally identified as a target of cAMP/cGMP dependent kinases during platelet activation (Halbrugge and Walter, 1989; Halbrugge et al., 1990). Subsequent work identified additional family members, including the *Drosophila* protein Ena (Gertler et al., 1990) and its mammalian orthologs: Mena and EVL, which are highly expressed in neurons and the spleen/thymus respectively (Gertler *et al.*, 1996; Lanier *et al.*, 1999).

The Ena/VASP proteins are modular and consist of several functional domains separated by unstructured linkers. The N-terminal EVH1 (Ena/VASP homology 1) domain binds specific targeting sequences in upstream regulators (Prehoda et al., 1999; Krause et al., 2004; Boeda et al., 2007). The C-terminal region contains a coiled-coil motif that mediates self-assembly of Ena/VASP proteins into stable tetramers (Bachmann *et al.* 1999; Kuhnel et al., 2004) and which appears to be required for proper function in vivo (Applewhite et al., 2007). Between the EVH1 and the coiled-coil are a set of sequence motifs that mediate the interaction of Ena/VASP proteins with both monomeric and filamentous actin. The so-called GAB (Globular Actin Binding) and FAB (Filamentous Actin Binding) domains have been shown to bind actin monomers and filaments (Bachmann *et al.* 1999; Huttelmaier *et al.*, 1999). Adjacent to these domains is a central proline-

rich region, which interacts with the actin monomer-binding protein profilin to recruit profilin-actin complexes (Mahoney et al., 1997; Ferron et al., 2007).

Since their discovery, Ena/VASP proteins have emerged as important regulators of actin network architecture. Deletion of all three Ena/VASP proteins in mice is embryonic lethal (Dent et al., 2007; Kwiatkowski et al., 2007). In migrating cells VASP localizes across the lamellipodial network and at the tips of filopodial protrusions (Rottner et al., 1999; Lanier et al., 1999). VASP is thought to play a central role in formation of these filopodial protrusions because, in fibroblasts, removal of VASP dampens filopodium formation and favors assembly of lamellipodia (Bear et al., 2002). Loss of VASP, however, also decreases the coherence of lamellipodial networks, which impairs migration of fish keratocytes (Lacayo et al., 2007) and slows the rate of lamellipodial protrusions in fibroblasts (Bear et al., 2002).

While the effects of perturbing localization and expression of Ena/VASP proteins have been well characterized *in vivo*, the mechanisms underlying the ability to regulate actin assembly remain controversial. Previous studies demonstrated that purified VASP can bind filamentous actin and induce formation of bundles *in vitro* (Huttelmaier *et al.*, 1999; Barzik et al., 2005). *In vivo*, however, VASP localizes to the tips rather than the sides of filopodia, indicating that side-binding and crosslinking alone likely does not explain its ability to promote formation of actin bundles inside living cells (Lanier et al., 1999; Applewhite et al., 2007). Interestingly, purified VASP has been shown to capture actin filament barbed ends and prevent termination of filament elongation by

capping protein in solution (Bear et al., 2002; Barzik et al., 2005; Pasic et al., 2008). Recently however, Breitsprecher *et al.* (2008) reported that VASP cannot antagonize capping protein in solution, but instead requires dense clustering to sterically hinder capping protein barbed end association. Previous studies have also reached different conclusions regarding whether VASP accelerates actin filament elongation. While one report detected marginal effects of VASP on the elongation rates of single actin filaments (Pasic et al., 2008), another study reported a significant acceleration of barbed end filament elongation (Breitsprecher et al., 2008). In addition, two studies concluded that VASP accelerates barbed end filament elongation in the presence of profilin-actin (Barzik et al., 2005; Pasic et al., 2008), while another study reached the opposite conclusion (Breitsprecher et al., 2008). One significant difference between these studies turns out to be the ionic strength of the buffers used in the experiments.

To better understand the mechanisms underlying the cellular function of VASP and to address questions raised by previous studies, we used total internal reflection fluorescence (TIRF) microscopy to visualize single fluorescently labeled VASP tetramers bound to static and growing actin filaments. In low ionic strength buffers we find that VASP is a processive actin polymerase that localizes to growing barbed ends where it accelerates polymerization in both the absence and presence of profilin. VASP barbed end association requires both the GAB and FAB domains as well as monomeric actin. In higher ionic strength buffers the combination of VASP plus profilin retains effective polymerase activity while the polymerase activity of VASP, plus actin alone decreases significantly.

Our observations help reconcile discrepancies between previous studies of VASP activity and enable us to construct a molecular model of how VASP functions to promote actin assembly.

Results

VASP accelerates actin assembly from the barbed-end.

We first constructed a fluorescent derivative of human VASP and visualized its interaction with filamentous actin using time-lapse Total Internal Reflection Fluorescence (TIRF) microscopy. This required mutating all the endogenous cysteines of human VASP (C7S, C64S, C334A) and introducing an N-terminal Lys-Cys-Lys peptide sequence, which we labeled with Cy3-maleimide (Cy3-VASP; Fig. 1 A). Consistent with results from Huttelmaier et al. (1999) and Barzik et al. (2005), our recombinant VASP co-sedimented with filamentous actin and accelerated actin assembly in bulk assays (Fig. 1, B and C). We also found that, in low ionic strength buffers (50 mM KCl) similar to those used by Breitsprecher et al. (2008), both unlabeled and Cy3-VASP accelerated barbed end growth up to 3-fold (Fig. 1 D). Acceleration was dose-dependent, with a maximum rate of ~30 subunit/second in the presence of 50 nM VASP (Fig. 1 D, Movie 1). Interestingly, in the higher ionic strength buffers (100 mM KCl) used by Pasic et al. (2008) we observed only a modest acceleration (20%) of actin assembly in the presence of VASP (Fig. 1 D). Since the behavior of Cy3-VASP was indistinguishable from unlabeled, wildtype VASP in all our assays, we considered the two proteins functionally equivalent.

Multiple modes of association between VASP and actin filaments.

Multi-step photobleaching verified that the fluorescent Cy3-VASP foci observed in our TIRF assays were single tetramers (Fig. 2, A and B). These molecules

displayed two distinct modes of interaction with actin filaments: (1) static side binding and (2) side-binding, followed by 1-dimensional diffusion along the filament (Fig. 2 C, Movie 2). The most common interaction was diffusive binding (68%, n=719), while a minority of these tetramers (11%, n=116) stopped moving and became statically attached. We also observed a large number of transient interactions (21%, n=222) whose lifetimes were too short to judge whether they were static or diffusive. A histogram of the association lifetimes of all interactions was best fit by a double exponential equation (Fig. 2 D) with characteristic dwell times corresponding to: (1) short-lived, 1D diffusion ($\tau_1=0.36\pm 0.01$ sec, n=909) and (2) static binding ($\tau_2=4.99\pm 0.35$ sec, n=148). Supporting our conclusion that the shorter dwell time represents diffusive binding, our data fit well to a single exponential when we removed the lifetimes for the static VASP molecules ($\tau_1=0.44\pm 0.01$ seconds, n=936) (Fig. 2 E).

To determine whether tetramerization is required for side binding, we visualized the localization of monomeric Cy3-VASP^{1-343aa} or dimeric Cy3-VASP^{1-343aa}-LZ (leucine zipper) on filamentous actin (Fig. 2 F). The oligomerization state of each construct was verified by sedimentation equilibrium ultracentrifugation and gel filtration (data not shown). Surprisingly, we detected no interactions between monomeric or dimeric VASP and filamentous actin under conditions in which tetrameric VASP strongly localized to actin filaments (Fig. 2 F).

Previous studies identified two regions of VASP that bind actin, called the GAB (Globular Actin Binding) and FAB (Filamentous Actin Binding) domains. These sequences have generally been thought to act independently and to carry

out distinct functions (Barzik et al., 2005; Ferron et al., 2007). The FAB domain has been proposed to bind the sides of actin filaments and promote bundling, while the GAB domain is thought to recruit actin monomers for barbed-end polymerization. We explored the function of these domains in more detail using point mutants (Fig. S1 A). Consistent with a role in binding filamentous actin, we found that mutation of basic residues in the FAB domain abolished actin filament binding (Fig. 2 F and S1, C and D). We also observed a reduced affinity of Cy3-VASP for actin filaments in buffers of increasing ionic strength (Fig. S2, A-C). Based on the crystal structure of an actin monomer bound to the VASP GAB domain (Ferron et al., 2007) and on previously reported actin binding mutants (Loureiro et al., 2002), we also generated the following GAB mutants:

VASP^{L226A,I230A,L235A} and VASP^{R236E,K237E}. As expected both mutations had reduced affinities for monomeric actin (data not shown). Surprisingly, however, both GAB mutations also compromised filament binding, albeit less severely than the FAB mutations (Fig. 2 F-H; Movie 3). The majority of interactions between GAB mutants and actin filaments were too short-lived to be characterized as either diffusive or static (Fig. 2 G). This result indicates that in the absence of soluble actin monomers the GAB domain can contribute to the interaction with the sides of actin filaments.

How does the presence of monomeric actin affect the side binding activity of VASP? If the GAB domain interacts with both monomers and filaments using the same residues, then the presence of monomeric actin should produce an effect similar to mutating the GAB domain, namely a decrease in the dwell time

on actin filaments. To test this prediction we compared the dwell times of wildtype VASP in the absence of monomeric actin to those measured in the presence of 1 μ M monomeric actin. For these experiments we used Latrunculin B to keep actin in the monomeric state and to avoid confounding effects due to filament elongation. Similar to the effect observed when the GAB domain was mutated, addition of 2 μ M monomeric actin dramatically reduced the lifetime of VASP on actin filaments ($\tau_1=0.10\pm0.002$ sec and $\tau_2=0.58\pm0.01$ sec, n=1006 molecules) (Fig. 2, G and H; Movie 4). Together, these data indicate that binding of monomeric actin to the GAB domain antagonizes lateral association of VASP with actin filaments.

VASP barbed end association requires actin monomer binding.

Previous work by Bear et al., (2002) and Pasic et al., (2008) suggested that VASP has an intrinsic affinity for actin filament barbed ends. In addition, the C-terminal fragment, VASP^{280-380aa}, has been proposed to contain a “cryptic” barbed end capture motif (Pasic et al., 2008). To test these proposals we compared the localization of Cy3-VASP and Cy3-VASP^{280-380aa} (C-terminal fragment) on the sides and barbed ends of polarity-marked actin filaments (Alexa488, barbed end; Alexa568, pointed end) (Fig. S3 B). First we measured the relative frequency and dwell time of Cy3-VASP binding to the apparent barbed end and the sides of filaments in the presence or absence of monomeric actin and/or capping protein. We found that, in the absence of monomeric actin, single VASP tetramers bound uniformly along the filament with no bias toward

the barbed end (Fig. 3, A-C). In addition, the dwell time of single VASP tetramers near the barbed end was indistinguishable from molecules bound elsewhere on the filament (data not shown). The presence of capping protein did not change the distribution or the binding frequency of VASP alone along the filament (Fig. 3 C). This suggests that the molecules we observe near the barbed end under these conditions are actually bound to the sides of the filaments.

Next we tested whether the C-terminal fragment, VASP^{280-380aa}, had an intrinsic barbed end capture activity. No binding of Cy3-VASP^{280-380aa} on the sides or barbed ends of filamentous actin could be detected (Fig. S3, A and C). Furthermore, VASP^{280-380aa} did not change the actin filament elongation rate, as would be expected for a protein that binds to the barbed end (Fig. S3 D). We also tested whether a barbed end capture motif could be unmasked by mutating both the GAB and FAB domains. However, we failed to detect an interaction between Cy3-VASP^{(L226A,I230A,L235A)/(RRRK-4A)} and filamentous actin (Fig. S3, A and D). Together, these results suggest that VASP lacks an intrinsic or cryptic barbed end capture motif.

Since VASP alone does not preferentially localize to barbed ends, we hypothesized that monomeric actin could be required to target VASP to barbed ends. When we visualized the localization the Cy3-VASP in the presence of 2 μ M actin (+LatB), we observed a shift from uniform localization to preferential barbed end binding (9% versus 24% of molecules barbed end localized; Fig. 3, A and C). This shift correlated with an increase in the dwell time at the apparent barbed end ($\tau_1=0.77\pm0.04$ sec, n=205 molecules) and a decrease in the dwell

time elsewhere on the filament ($\tau_1=0.11\pm 0.01$ sec, $n=181$), due to actin monomer binding antagonizing lateral filament interactions (Fig. 3 D). Whereas capping protein had no effect on the uniform localization of VASP alone, in the presence of monomeric actin it blocked barbed end association of VASP (Fig. 3, C and D). When we mutated either the GAB or FAB domain, localization to the barbed end was not detected (data not shown). Together these data indicate that actin monomer binding is required for VASP barbed end association.

Several actin regulators have been shown to bind preferentially to either ATP or ADP actin filaments (Blanchion and Pollard, 1999; Mahaffy and Pollard, 2006), so we next asked whether the nucleotide state of the actin filament biases the binding of VASP toward the barbed end. To address this question, we correlated the localization and dwell time of Cy3-VASP to the age of filamentous actin (Fig. S4 A; nucleotide state: ADP-P_i versus ADP). We followed the life history of elongating actin filaments, terminated barbed end growth with capping protein, and then imaged the localization of Cy3-VASP on these filaments (Fig. 3 E; Fig. S4, B and C). First, we found that the binding frequency of Cy3-VASP molecules was independent of the ADP-P_i/ADP nucleotide state of the filament (Fig. 3 F). Second, the dwell times for single molecules binding to regions of filaments with a high or low probability of containing ADP-P_i were nearly identical (Fig. 3 G; $\tau_1= 0.93\pm 0.01$ sec, $n=235$, $p(\text{ADP-P}_i) > 0.5$; $\tau_1= 1.0\pm 0.01$ sec, $n=1135$, $p(\text{ADP-P}_i) < 0.5$). Third, the steady state localization of a sub-saturating concentration of Cy3-VASP was independent of the probability of finding ADP-P_i along the filament length (Fig. 3, H and I). Together, these data suggest that

VASP does not recognize the ADP-P_i/ADP nucleotide state of the filament to which it binds.

Processivity of single VASP tetramers.

We next wondered whether, similar to formins, VASP associates processively with growing filament ends and delivers multiple actin monomers before dissociating. When we imaged Cy3-VASP barbed end association events in the presence of polymerizable actin (Fig. 4 A), we found that single VASP tetramers persistently associated with and surfed along the growing barbed ends (Fig. 4, B-F; Movie 5). Interestingly, we occasionally observed molecules that initially laterally associated with actin filaments and then diffused in 1-D before capturing the growing filament end (Fig. 4 D). Once attached to the barbed end, VASP tetramers surfed along for 1.45 ± 0.02 seconds ($n=1166$ molecules) in the presence of $1 \mu\text{M}$ actin before dissociating (Fig. 4 E). Strikingly, we found that the average velocity of single VASP tetramers bound to growing filament ends (33 ± 6.5 sub/sec, $n=7$ highly processive VASP tetramers; Fig. 4 F and Movie 6) closely matched the maximum rate of filament growth measured in the presence of 50 nM VASP (29.1 ± 1.2 sub/sec, $n \geq 30$ filaments; Fig. 4, G and H), while unoccupied barbed ends elongated at the basal polymerization rate (~ 10 sub/sec; dashed line Fig. 4 C). By fitting the rate of actin filament growth versus the concentration of VASP, we calculated a K_d of 9.2 nM for the VASP barbed end interaction (Fig. 4 G). Using the barbed end dwell time ($\tau_1=1.45$ seconds in the presence $1 \mu\text{M}$ Actin) and maximum polymerization rate ($+ 50 \text{ nM}$ VASP), we

estimate that a VASP tetramer delivers, on average, 42 monomers before dissociating from the barbed end. We were unable to determine the effect of ionic strength on processivity because of rapid filament motion in higher ionic strength buffers.

Consistent with monomeric actin being required for barbed end association, we did not observe an interaction between VASP GAB mutants (VASP^{L226A,I230A,L235A} and VASP^{R236E,K237E}) and growing actin filament barbed ends (data not shown). Furthermore, neither of these mutants could enhance barbed end filament elongation (Fig. S1 B). Similar to the phenotype observed for the GAB mutants, we found that mutations in the FAB domain (VASP^{RRRK-EEEE}) abolished processive barbed end filament tracking (data not shown).

Contrary to the model proposed by Breitsprecher et al. (2008), VASP barbed end association rarely transitioned to a lateral side-binding interaction (0.5%; n=1166 molecules). Instead, VASP tetramers dissociated directly from the barbed end with an off rate of 0.69 sec^{-1} ($1/\tau_1$) in the presence of $1 \mu\text{M}$ actin. Although VASP tetramers rarely transition from barbed end to a static lateral interaction, molecules from solution frequently bound the sides of growing filaments near the barbed end. The lifetime of these molecules were significantly shorter ($\tau_1=0.22\pm 0.01 \text{ sec}$, n=280; Fig. 4 C arrowheads) than the processive barbed end tracking tetramers.

To better understand the mode of interaction between VASP and growing barbed ends, we measured the maximum barbed end growth rate in the presence of saturating VASP and increasing concentrations of Mg-ATP-actin

(0.25-2 μM ; Fig. 4 H). We found that the barbed end association rate constant for Mg-ATP-actin increases 2.7-fold in the presence of 50 nM tetrameric VASP ($9\mu\text{M}^{-1}\text{sec}^{-1}$ actin alone versus $24\mu\text{M}^{-1}\text{sec}^{-1}$ plus 50 nM VASP; Fig. 4 H, curve fit not shown). Next, we measured the single molecule lifetimes of Cy3-VASP processively bound to growing actin filament barbed end (Fig. 4 I). At all actin concentrations tested, the lifetimes of barbed end associated VASP tetramers were exponentially distributed. Strikingly, although we observed a 4-fold increase in the maximum rate of barbed end polymerization between 0.5 μM and 2 μM actin, we observe only a 19% reduction in barbed end dwell time for VASP tetramers (Fig. 4 I). This demonstrates that the lifetime of VASP barbed attachment is almost insensitive to the barbed end growth velocity. Based on actin monomer binding data obtained by sedimentation equilibrium, it appears that VASP tetramers are not completely saturated in the presence of 2 μM monomeric actin (Fig. S6). We hypothesize that VASP will promote faster barbed end elongation and deliver more subunits at higher actin concentrations.

Since the majority of actin monomers are bound to profilin *in vivo* (Kaiser et al., 1989), we next investigated the effect of human profilin I on VASP-mediated actin polymerization. From sedimentation equilibrium experiments, we find that monomeric VASP interacts with two molecules of human profilin I (Fig. 5 A). This interaction requires the poly-proline domain located in the central domain of VASP. Attempts to measure the stoichiometry of profilin-actin binding to full length tetrameric VASP were foiled by the complexity of interaction between the three protein. Compared to barbed end polymerization in the presence of 2 μM

profilin-actin alone (11.4 ± 1.2 sub/sec), we observed a 2.5-fold rate enhancement in the presence of 50 nM VASP (28.2 ± 2.0 sub/sec) (Fig. 5 B; Movie 7).

Enhancement was dependent on the interaction between profilin and the poly-proline domain ($2 \mu\text{M}$ Actin-hPro1^{H133S} + VASP; 11 ± 0.7 sub/sec) (Fig. 5 B) and was only marginally affected by increasing the ionic strength of the buffer (Fig. 5 C). Mutations in the high affinity poly-proline domain (VASP^{PPPLPPAP-AAAAAAA}) also reduced the maximum barbed end polymerization rate (Fig. 5 B). In the presence of a profilin mutant that cannot bind actin (hPro1^{Y59A}) filaments assembled at a rate indistinguishable from that of VASP plus actin alone (data not shown). In conclusion, these results show that VASP can promote barbed end growth in the presence of profilin-actin and. Consistent with results published by Barzik et al. (2005), this acceleration is dependent on the interaction between profilin-actin and the poly-proline domain. Interestingly, the interaction between profilin-actin and the poly-proline domain can partially rescue the inability of VASP^{L226A,I230A,L235A} to accelerate barbed end filament elongation in the presence of actin alone ($2 \mu\text{M}$ Actin-hPro1 + VASP^{L226A,I230A,L235A}, 16.3 ± 1.2 sub/sec) (Fig. 5 B).

Since the interaction between profilin and the poly-proline domain is essential for rapid VASP-mediated polymerization of profilin-actin in vitro, we investigated what effect slower polymerization rates have on VASP barbed end processivity. When we measured the barbed end association lifetime for VASP tetramers in the presence of hPro1 or hPro1^{H133S}, we observed no significant differences (Fig. 5 D). Since the dwell time was insensitive to slower barbed end

polymerization kinetics, VASP tetramers simply delivered fewer actin monomers per association event in the presence of hPro1^{H133S} (Fig. 5 E). In the presence of 1 μM hPro1-actin, VASP tetramers deliver ~ 30 actin monomers within 1.45 sec (Fig. 5 E), while only 10 actin monomers are delivered by VASP tetramers over the same period of time in the presence of 1 μM hPro1^{H133S}-actin.

VASP antagonizes capping protein barbed end association in the presence of profilin-actin.

To test whether VASP antagonizes capping protein, we polymerized profilin-actin in the presence or absence of VASP and/or capping protein (Fig. 6 A). Comparing the average filament length distribution after 5 min of barbed end growth, we found that filaments grown in the presence of 0-20 nM MmCP, plus 50 nM VASP were significantly longer (Fig. 6 A and B). Interestingly, the difference in filament length was not solely due to a VASP dependent rate enhancement of barbed end growth (Fig. 6 B, dashed line). Rather VASP barbed end polymerase activity significantly delayed association of capping protein. Based on the rate at which barbed end growth was terminated by capping protein in the presence of VASP (Fig. 6 C), we calculated a 6.3-fold reduction in the barbed end association rate constant for capping protein ($12 \mu\text{M}^{-1} \text{sec}^{-1}$, no VASP; $1.9 \mu\text{M}^{-1} \text{sec}^{-1}$, plus 50 nM VASP; Fig. 6 D). We also performed these experiments in the presence of 100 mM KCl and observed a 2.7-fold reduction in the association rate constant for capping protein (Fig. S2 D).

Discussion

The polymerase activity of VASP: Polymerization, processivity, and profilin.

Two previous TIRF microscopy studies reported different effects of VASP on actin filament elongation. Pasic et al. (2008) observed minor effects, while Breitsprecher et al. (2008) observed a significant concentration-dependent acceleration of barbed end growth. One difference between the previous studies is the ionic strength of the buffers used in the assays of filament elongation. In the present study we find that, in the low ionic strength buffers (50 mM KCl) used by Breitsprecher et al. (2008) human VASP accelerates barbed-end elongation of actin filaments by 300%, while, in the higher ionic strength buffers (100 mM KCl) used by Pasic et al. (2008), the effect on elongation is much more modest (~20%). In our hands, the polymerase activity of VASP requires the presence of both the GAB and FAB. Interestingly, we find that VASP also accelerates filament elongation by approximately 250% in the presence of human profilin 1 and that this effect is mostly insensitive to the ionic strength. In the presence of profilin, the acceleration of filament assembly requires an interaction between profilin-actin complexes and the poly-proline domain of VASP. Remarkably, when both profilin and an intact poly-proline domain are present, the polymerase activity of VASP^{L226A,I230A,L235A} (GAB mutant) was partially rescued.

The simplest interpretation of these results is that VASP can add actin monomers to the barbed end from either the GAB domain or from a profilin-actin complex bound to the poly-proline domain. The difference in sensitivity to ionic strength is likely due to the fact that binding of actin monomers to the GAB

domain is driven primarily by electrostatic interactions while binding of profilin to proline-rich domains is primarily a hydrophobic interaction whose affinity is actually increased by raising the salt concentration (Petrella *et al.*, 1996). Similarly, the affinity of profilin for monomeric actin is relatively insensitive to ionic strength (Vinson *et al.*, 1998). In ameboid cells most unpolymerized actin is bound to profilin (Kaiser *et al.*, 1989; Pollard and Borisy, 2003) and so we suggest that the salt-independent polymerase activity of VASP in the presence of profilin-actin complexes is a more physiologically relevant phenomenon than the polymerase activity observed in the absence of profilin.

Because the filament elongation rate increases with VASP concentration, Breitsprecher *et al.* (2008) proposed that VASP binds barbed ends distributively, delivering a maximum of 4 actin monomers before either dissociating or remaining statically attached to the side of the filament. We find, however, that, in the low ionic strength buffers used for these experiments, individual hVASP tetramers interact processively with growing filament ends and, in the presence of 2 μM actin, can deliver more than 60 actin monomers before dissociating. The average lifetime of a VASP tetramer on the end of a growing actin filament is 1.45 sec, which makes its activity much less processive than some formins (Kovar *et al.*, 2006). Interestingly, however, the lifetime of barbed end association is only weakly sensitive to the rate of filament elongation and this is true both in the presence and absence of profilin. For technical reasons we could not explore the effects of actin concentrations above 2 μM but, at physiological actin concentrations, we estimate a single VASP tetramer could deliver several

hundred monomers per barbed end association event. In summary, we propose that actin, or profilin-actin, targets VASP to the barbed end of actin filaments where it remains weakly tethered by the FAB domain and delivers monomers for a dwell time that is independent of the rate of filament elongation.

Multiple modes of actin interaction.

In the absence of monomeric actin, VASP tetramers undergo both static and diffusive binding to the sides of actin filaments. Based on mobility and lifetime, diffusive binding is the weaker of the two modes and mutagenesis indicates that the majority of binding energy in this mode is contributed by the FAB domain. The simplest model to account for the difference between the two modes is that diffusive binding involves engagement of a smaller number of FAB domains than the longer-lived, static mode. The occasional transitions from diffusive to static binding probably represent engagement of more FAB domains. The low frequency of transitions suggests that steric constraints limit the ability of all four FAB domains in a tetramer to contact one filament. This interpretation also fits with the fact that VASP tetramers bind more strongly to closely apposed pairs of filaments (Fig. S5, A-D; Movie 8), since a second filament provides additional FAB binding sites. Also, the flexibility of VASP means that the orientation of the overlapping filaments (parallel versus anti-parallel) makes little difference (Fig. S5 D).

The GAB domain also contributes to diffusive binding and the diffusion along a filament likely reflects binding and unbinding of FAB domains under

conditions where the weak interaction of the GAB domains is sufficient to keep the VASP tetramer from diffusing away before another FAB domain binds. The flexibility of VASP and the four FAB domains in a tetramer mean that re-binding will likely occur on a different subunit of the filament, producing a diffusive, random walk.

The mechanism of processive interaction with growing barbed ends.

Monomeric actin destabilizes side-binding modes and stabilizes the interaction of VASP with filament ends. This result suggests that the GAB domain uses the same residues to bind monomers and filaments and that it does not interfere with the ability of a bound monomer to interact with a filament barbed end. We propose that, similar to diffusive side binding, processive barbed end binding is driven by a combination of GAB and FAB domains. When the GAB domains are bound to monomeric actin they cannot contribute to filament tethering unless the VASP tetramer is located near the barbed end of the filament. At the barbed end, the GAB domains can contribute their bound monomers to the growing filament and maintain the VASP tetramer in the vicinity of the filament end. The affinity of the GAB domain for actin monomers appears to be higher than for filaments so (similar to WH2 domains and profilin) incorporation of a bound monomer into the filament promotes dissociation of the GAB domain and frees it up to bind another monomer. The GAB domain is related to WH2 domains found in other actin regulatory proteins (Chereau et al., 2005; Ferron et al., 2007) and, consistent with our results, Co et al. (2007) found that WH2 domains from N-WASP can

interact with barbed ends of actin filaments and recruit the molecule to sites with a high density of free barbed ends. In a VASP tetramer, the multiple GAB domains tethered near the end of the filament likely increase the rate of filament elongation by capturing actin monomers at a higher rate than a barbed end by itself (Fig. 7). The participation of the FAB domain in polymerase activity and the fact that VASP localizes only to tips of filopodial bundles *in vivo* suggest to us that the strong bundling activity of VASP observed *in vitro* is not related to all of the *in vivo* function of the molecule. Bundling of filament ends at the tips of filopodia likely requires higher-order oligomerization of VASP, perhaps mediated by proteins such as Lamellipodin (Krause *et al.*, 2004).

In vivo relevance.

Previous *in vivo* studies indicate that recruitment of VASP to the plasma membrane significantly increases the average length of the membrane-proximal actin filaments (Bear *et al.*, 2002). This has been interpreted as evidence that VASP prevents or postpones capping of actin filaments and enables them to grow for longer periods of time (Bear and Gertler, 2009). Such results are, however, also consistent with VASP-dependent acceleration of actin assembly. Our data indicate that, even though the lifetime of VASP on the end of an actin filament (1.5 sec) is much shorter than the lifetime of capping protein (~30 min *in vitro*; Kuhn and Pollard, 2007), VASP can delay the binding of capping protein to filament ends, producing a 6.3-fold decrease in the association rate constant for capping protein. The effectiveness of this competition relies on the very fast

association rate of VASP ($75 \mu\text{M}^{-1} \text{sec}^{-1}$) which gives it nanomolar affinity for barbed ends. Observation made by Breitsprecher et al. (2008), suggest that clustering of VASP molecules into dense foci is likely to further enhance this effect. More work is required to measure the densities of VASP molecules at various locations in various cell types and to quantify the relationship between VASP density and anti-capping activity.

Previous experiments using cytochalasin D and RNAi knockdown demonstrated that VASP is recruited to the leading edge by both free barbed ends and by membrane associated proteins such as *Mig-10/RIAM/Lamellipodin* or *CXCR2* (Krause et al., 2004; Lacayo et al., 2007; Neel et al., 2009). Based on our results the contribution of barbed ends to localization is analogous to the WH2-dependent recruitment of N-WASP to free barbed ends (Co et al., 2007). Svitkina et al. (2003) reported that the intensity of GFP-VASP increases locally at sites on the plasma membrane that subsequently give rise to filopodia. At present it is unclear whether convergence of actin filament barbed ends and/or clustering of VASP tetramers is sufficient to drive filopodia formation. Other activities, such as nucleation by formin-family proteins or bundling by fascin are likely required (Vignjevic *et al.*, 2006). Reconstituting the interplay between these factors will lead to a better understanding of how cells dynamically regulate the architecture of functional actin networks.

Single molecule imaging of GFP-VASP in vivo suggests that the majority of the proteins are rapidly binding and then dissociating from actin (Miyoshi et al., 2007). In light of our results, we believe this population of protein represent

transient interaction with the sides of actin filament in the lamellipod. However, a smaller fraction of the molecules have lifetimes that are greater than 5 sec. Interestingly, the proteins with the long lifetimes are localized to the leading edge or membrane of a polarized cell.

Materials and Methods

Molecular biology

Human VASP^{1-380aa} and derivatives were cloned into a modified pET vector containing an N-terminal his₆ tag with a TEV protease cleavage site (HHHHHDYDIPTTENLYFQ--GS...). A Gly-Ser remains N-terminal post-TEV-cleavage. Quick change site directed mutagenesis was used to mutate cysteines, GAB, FAB, and poly-proline domain residues of human VASP. The following point mutations in hVASP were made to generate the “cysteine light” version: C7S, C64S, C334A. Mutation C334S caused VASP to be proteolyzed during expression in *E. coli*, while C334A did not. Primer sequences are available upon request. We made the constitutive VASP dimer by replacing the C-terminal coiled-coil with the leucine zipper derived from *S. cerevisiae*, Gcn4 (KQLEDKVEELASKNYHLENEVARLKKLV) (Tomishige et al., 2002).

Protein purification and labeling

Expression of his₆-TEV-hVASP and his₆-TEV-KCK-hVASP^{CCC-SSA} constructs was performed using BL21 Rosetta *E. coli*, induced with 50 μM IPTG at 18⁰C for 16 hours. Cultures were harvested, spun down, and stored at -80⁰C prior to lysis. Using a microfluidizer, bacteria were lysed into 50 mM NaH₂PO₄, 300 mM NaCl, 10 mM imidazole, 10 mM beta-mercaptoethanol, 1 mM PMSF, pH 8. High speed supernatant was then batch bound to Qiagen Ni-NTA resin. Resin was washed with lysis buffer containing 20 mM imidazole and eluted with lysis buffer containing 500 mM imidazole. TEV protease was then added and the protein was

dialyzed overnight in 50 mM NaH₂PO₄ pH 8, 300 mM NaCl, 10 mM β-ME. Cleaved VASP was then dialyzed into 10 mM HEPES pH 7.5, 50 mM KCl, 0.5 mM TCEP to precipitate uncleaved his₆-VASP. We find that his₆-VASP is mostly insoluble in buffers containing 50mM KCl. Precipitant was removed by syringe filtration or ultracentrifugation. Protein was then flowed over DEAE resin to remove high molecular weight contaminants and Ni-NTA resin (Qiagen) to remove uncleaved his₆-VASP and TEV protease. VASP tetramers were further purified using a Superdex200 gel filtration column, followed by a cation exchange (MonoS column). Based on sedimentation equilibrium, VASP was a soluble tetramer (162 kDa measured molecular weight compared to 161 kDa expected for a VASP tetramer). Pure untagged hVASP^{1-380aa} was dialyzed into storage buffer (10 mM HEPES pH 7.5, 1 mM TCEP, 50 mM KCl, 25% glycerol) and frozen with liquid nitrogen before -80⁰C storage. As judged by pyrene actin polymerization assay, single actin filament TIRF microscopy, and cosedimentation with filamentous actin, freezing did not reduce the activity of VASP. The extinction coefficient for VASP was determine from a SYPRO Red (Molecular Probes) stained quantitative gel ($\epsilon_{280} = 36565 \text{ M}^{-1} \text{ cm}^{-1}$).

Labeling was achieved by combining reduced GS-KCK-hVASP^{1-380aa} with 5 molar excess Cy3-maleimide (GE Healthcare, CAT# PA13131) on ice for 15 minutes before quenching with 10 mM DTT. Insoluble material was then removed by high speed ultracentrifugation, while soluble free dye was removed with a G25 Sephadex column. Labeling efficiency was assessed with a spectrophotometer. The contribution of Cy3 to the A₂₈₀ signal (8.6%) was subtracted to accurately

calculate the final protein concentration. A labeling efficiency of 85-95% was typical achieved.

Cytoplasmic actin was purified from *Acanthamoeba castellanii* based on the methods described in Gordon et al. (1976). Gel filtered monomeric actin was stored in buffer containing 2 mM Tris pH 8.0, 0.5 mM TCEP, 0.1 mM CaCl₂, and 0.2 mM ATP. Actin was labeled on Cys-374 with Alexa488-maleimide (Molecular Probes CAT# A-10254) using the same method employed for labeling KCK-VASP. Human profilin I, hProl^{H133S}, and hProl^{Y59A} were purified using established protocols (Kaiser, 1989; Lu and Pollard, 2001). Recombinant mouse capping protein was purified using a protocol adapted from Palmgren et al. (2001). Heavy meromyosin (HMM) was a gift from Roger Cooke. We biotinylated HMM with EZ-link maleimide-PEO₁₁-biotin (Pierce, Cat# 21911).

Actin cosedimentation assay

4 μM (2x final concentration) *A. castellanii* G-actin was polymerized for 60 minutes in KMEI (50 mM KCl, 1 mM MgCl₂, 1 mM EDTA, 10 mM imidazole pH 7), plus equal molar concentration of dark phalloidin. A 2-fold serial dilution of 10 μM VASP (diluted in KMEI) was combined with an equal volume of F-actin to obtain the final concentrations of 2 μM F-actin, plus 0.31-5 μM VASP (2-fold dilutions; monomeric concentrations). F-actin and VASP were allowed to equilibrate for 60 minutes at room temperature in 7x20 mm Beckman PC tubes before ultracentrifugation in a TLA100 rotor for 30 minutes, 48000 rpm (102611x g), at 25°C. Supernatants were removed and pellets were resuspended in 1x sample

buffer. To normalize for gel loading differences, a no spin load of known actin and VASP concentrations was used to quantify the amount VASP that cosedimented with F-actin. SDS-PAGE gels were stained with SyproRed and scanned with a Typhoon gel imaging system (532nm/580nm; EX/EM).

Pyrene Actin Polymerization Assay

Actin purified from *A. castellani* was labeled with pyrene iodoacetamide as previously described (Cooper *et al.*, 1983). Polymerization reactions were performed in 1x KMEI (50 mM KCl, 1 mM MgCl₂, 1 mM EGTA, 10 mM imidazole pH 7.0) and initiated by converting Ca²⁺-ATP-actin to Mg²⁺-ATP-actin with 10X ME (0.5 mM MgCl₂, 2 mM EGTA). A final concentration of 2 μM Mg-ATP-actin (5% pyrene labeled) was polymerized in the presence or absence of 63 nM tetrameric VASP (250 nM monomeric concentration). Pyrene fluorescence was measured with an ISS PCI/K2 fluorimeter.

Preparation of glass

Coverslips were sonicated in Coplin jars for 20 minutes in ethanol, 0.5 M KOH, and ethanol with milliQ washes in between each step. Glass was then washed with isopropanol before a 30 minute sonication in silane solution (95% isopropanol, 1 mM glacial acetic acid, 3% 3-aminopropyltriethoxysilane (Sigma), and 2% milliQ water). Slides were washed with isopropanol and then baked at 90°C for ≥ 8 hours. Baked slides were then sonicated twice in ethanol for 20 minutes before being stored in 100% ethanol. Before pegylation, glass was

washed with MilliQ water and oven dried for 10 minutes. PEGylation of silanized slides required assembly of flow cells with double stick tape to create a 10 μ L volume flow space. Flow cells were washed with 100 mM HEPES pH 8, before adding a 10 mg/mL solution containing 90% PEG-NHS and 10% Biotin-PEG-NHS (JenKem Technology USA Cat#M-SCM-5000 and BIOTIN-PEG5000-NHS respectively). Three rounds of PEGylation were performed at room temperature in a humidity chamber over the course of 90 minutes. Flow cells were then washed with MilliQ water and stored hydrated at 4⁰C for up to one week.

Single actin filament TIRF assays

Pegylated TIRF chambers were incubated with 1 μ M streptavidin (Rockland CAT# S000-01), followed by an incubation with 1 μ M biotin (0.8 μ M free biotin, plus 0.2 μ M biotinylated heavy meromyosin). For barbed end polymerization experiments we followed procedures outlined in Kuhn and Pollard, (2005) with modifications. In brief, we combined 9 μ L of 4.44 μ M Actin (30% Alexa488 labeled) with 1 μ L of 10x ME (0.5 mM MgCl₂, 2 mM EGTA) for 2 minutes. Followed by the addition of a solution containing 10 μ L Cy3-VASP (1x KMEI, 1 mg/mL BSA), plus 20 μ L of 2x TIRF buffer (75 mM KCl, 1.5 mM MgCl₂, 1.5 mM EGTA, 15 mM imidazole pH 7.0, 2 mM DTT, 0.2 mM ATP, 0.4% methycellulose cP400, 1 mg/mL BSA 200 μ M n-propyl gallate, 4 mM Trolox, 2 mM 3,4-Dihydroxybenzoic acid (PCA), and 100 nM Protocatechuate 3,4-Dioxygenase). For polymerization off actin filament barbed ends, the polymerization was performed in a TIRF chamber containing phalloidin stabilized Alexa488 actin

filaments. For experiments involving profilin-actin, we used 10% Alexa488-actin because Cys-374 labeled actin has a reduced affinity for profilin (Vinson *et al.*, 1998). Profilin-actin was always combine in equal stoichiometry for TIRF experiments. Unless noted in the figure legends, the final KMEI buffer composition was 10 mM imidazole pH 7.0, 50 mM KCl, 1 mM MgCl₂, and 1 mM EGTA for all single actin filament TIRF assays. All concentrations of VASP mentioned in the manuscript represent the tetramer, unless otherwise noted. The details of the oxygen scavenging system are described in Aitken et al., (2008) and Rasnik et al., (2006).

Dual colored actin filaments were generated by polymerizing 0.5 μ M monomeric actin (40% Alexa488 labeled; green) in the presence of 20 nM Alexa568-phalloidin stabilized actin filaments (red) for 4 minutes. Dual colored seeds were then flowed into the TIRF chamber, captured by biotin-HMM, and chased with 1 μ M dark phalloidin to prevent barbed end depolymerization.

Capping protein-VASP barbed end competition

Small phalloidin stabilized actin filament seeds (50% Alexa488 labeled, ~2-3 μ m length) were immobilized in TIRF chamber. Separately, 2 μ M monomeric actin (10% Alexa 488), 2 μ M profilin, 0-20 nM MmCP α 1 β 2, 50 nM VASP, and buffers were combined and flowed into chamber. Elapsed time was approximately 60 seconds between mixing and imaging. Only filaments that appeared in the first frame (t= 60 sec) were followed throughout the experiment. This approach ensured that only the free barbed ends at the start of the experiment were scored

for filament length ($t = 5$ min) and the time at which growth was terminated by capping protein. If filaments were capped at the start of image acquisition, the time at which growth was terminate was calculate from the length of new growth and the average barbed end polymerization rate for a given condition. Filaments falling from solution onto the coverslip (polymerization history unknown) or new filaments appearing due to spontaneous nucleation (results in an underestimate of average filament length) impose artifacts. These filaments were not scored in our analysis of VASP anti-capping. Lengths of ≥ 150 filaments were measured from ≥ 3 slides.

Analytical ultracentrifugation

For sedimentation equilibrium experiments, full length Cy3-VASP or Cy3VASP^{1-240aa} were buffer exchanged into 1x KMEI containing 1mM TCEP and then spun at 70,000 rpm in a TLA100.4 to remove protein aggregates. A final concentration of 3-7 μ M Cy3-VASP was then combined with increasing concentration of human profilin I (30, 60, 90 μ M).. Samples were loaded into a 6-well chamber, placed in an AN-60 rotor, and spun at three different speeds (e.g. 10, 14, and 20K rpm) in a Beckman XL-I ultracentrifuge (16-20 hours per speed). Continuous scans were acquired every 2 hours at 527/550nm to monitor the sedimentation of Cy3-VASP constructs. Extinction coefficient of 150,000 $M^{-1} cm^{-1}$ were used to determine the Cy3-VASP protein concentration from the absorbance at 550 nm. Global fitting of three equilibrium traces (e.g. 10, 14, 20K rpm) for each condition was performed

using NIH Sedphit and Sedphat software. More complex data analysis of actin monomer binding to VASP was performed using MatLab (refer to Fig. S 6).

Microscopy, software, and data analysis

All microscopy was performed on a NIKON Eclipse TE2000-E microscope with Nikon Perfect Focus at 23⁰C. All images were acquired using an ANDOR iXon cooled EM CCD camera and Micromanager 3.0 software (Stuurman et al., 2007). Fluorophores were excited through a 100x Nikon Apo TIRF objective (NA 1.49) using either a 40mW 488/514 Argon Ion laser or 40mW 542 crystal laser. For rapid dual color imaging of Alexa488 actin and Cy3-VASP we used a hybrid Chroma/Shemrock dual bandpass filter. For image analysis of microscopy data, we used ImageJ. An ImageJ Kymograph plugin, designed by J. Rietdorf (FMI Basel) and A. Seitz (EMBL Heidelberg), was used to measure barbed end polymerization rates of single actin filaments. Since VASP is a potent actin bundler, we limited our measurements of barbed end growth to single actin filaments. Error bars for all actin filament growth rates are standard deviations ($n \geq 30$ filaments from ≥ 2 slides for each condition). Error bars for dwell times are standard error of measurement (s.e.m.) from curve fitting. Burst phase image sequences of Cy3-VASP were collected for 50-100 seconds at a frame rate of 50-100 milliseconds. Processivity of single Cy3-VASP barbed end association events were visualized by superimposing the path of actin filament growth onto the Cy3-VASP burst phase image sequence. Cy3-VASP molecules falling on the diagonal of the kymograph were scored as barbed end association events. This

method of analysis was previously used by Bieling et al., (2007) to measure the lifetime of microtubule plus-end tracking proteins. Dwell times for single Cy3-VASP tetramers was determined by fitting 1-cumulative frequency to a single exponential equation, $f(x) = x_0 \cdot \exp(-x/\tau_1)$, or a double exponential equation, $f(x) = x_0 \cdot \exp(-x/\tau_1) + (1-x_0) \cdot \exp(-x/\tau_2)$. All curve fitting and data plots were made in KaleidaGraph. Final figures were generated with Adobe Photoshop CS3 and Illustrator CS3.

Acknowledgements

We thank Orkun Akin for technical support, reagents, and demonstrating how to be a meticulous scientist; Brad Zuchero and Peter Beiling for critical reading of the manuscript; Roger Cooke and Kathy Franks-Skiba for heavy meromyosin; Bethany Simmons for assistance with MatLab; and members of the Mullins, Vale, and Weiner labs for reagents and feedback. Scott Hansen dedicates this work to Dr. Galen George, Gary Decicco, and Dennis Fujita for teaching him chemistry at Santa Rosa Junior College. This work was supported by grants from the National Institute of Health (R.D.M., ROI #GM61010), UCSF/UC Berkeley Nanomedicine Development Center (NDC), and the National Science Foundation (S.D.H.).

Abbreviations

GAB domain, Globular actin binding domain; FAB domain, Filamentous actin binding domain; Ena/VASP, Enabled/vasodilator stimulated phosphoprotein; TIRF, Total internal reflection fluorescence.

References

- Aitken, C.E., R.A. Marshall, and J.D. Puglisi. 2008. An Oxygen Scavenging System for Improvement of Dye Stability in Single-Molecule Fluorescence Experiments. *Biophysical Journal*. v94:1826-35.
- Akin, O. and R.D. Mullins. 2008. Capping protein increases the rate of actin-based motility by promoting filament nucleation by the Arp2/3 complex. *Cell*. 133, 841-851.
- Adler, C.E., R.D. Fetter, and C.I. Bargmann. 2006. UNC-6/Netrin induces neuronal asymmetry and defines the site of axon formation. *Nature Neuroscience*. 9(4):511-518.
- Applewhite, D.A., M. Barzik, S. Kojima, T.M. Svitkina, F.B. Gertler, and G.G. Borisy. 2007. Ena/VASP proteins have an anti-capping independent function in filopodia formation. *Mol. Biol. Cell*. 18, 2579-2591.
- Bachmann, C., L. Fischer, U. Walter, and M. Reinhard. 1999. The EVH2 domain of the vasodilator-stimulated phosphoprotein mediates tetramerization, F-actin binding, and actin bundle formation. *J. Biol. Chem*. 274, 23549-23557.
- Barzik, M., T.I. Kotova, H.N. Higgs, L. Hazelwood, D. Hanein, F.B. Gertler, and D.A. Schafer. 2005. Ena/VASP proteins enhance actin polymerization in the presence of barbed end capping proteins. *J. Biol. Chem*. 280, 28653-28662.
- Bear, J.E., T.M. Svitkina, M. Krause, D.A. Schafer, J.J. Loureiro, G.A. Strasser, I.V. Maly, O.Y. Chaga, J.A. Cooper, and G.G. Borisy. 2002. Antagonism between Ena/VASP proteins and actin filament capping regulates fibroblast motility. *Cell*. 109, 509-521.
- Bear, J.E. and F.B. Gertler. 2009. Ena/VASP: towards resolving a pointed controversy at the barbed end. *J. Cell Sci*. 122, 1947-1953.
- Bieling, P., L. Laan, H. Schek, E.L. Munteanu, L. Sandblad, M. Dogterom, D. Brunner, and T. Surrey. 2007. Reconstitution of a microtubule plus-end tracking system *in vitro*. *Nature*. 450(13):1100-1105.
- Blanchion, L. and T.D. Pollard. 1999. Mechanism of interaction of Acanthamoeba actophorin (ADF/Cofilin) with actin filaments. *J. Biol. Chem*. 274(22): 15538-46.
- Boeda, B., D.C. Briggs, T. Higgins, B.K. Garvalov, A.J. Fadden, N.Q. McDonald, and M. Way. 2007. Tes, a specific Mena interacting partner, breaks the rules for EVH1 binding. *Mol. Cell*. 28, 1071-1082.

Breitsprecher, D., A.K. Kieseewetter, J. Linkner, C. Urbanke, G.P. Resch, J.V. Small, and J. Faix. 2008. Clustering of VASP actively drives processive, WH2 domain mediated actin filament elongation. *EMBO J.* 27, 2943-2954.

Chereau, D. and R. Dominguez. 2006. Understanding the role of the G-actin-binding domain of Ena/VASP in actin assembly. *J. Struct. Biol.* 155, 195-201.

Co, C., D.T. Wong, S. Gierke, V. Chang, and J. Taunton. 2007. Mechanism of actin network attachment to moving membranes: barbed end capture by N-WASP WH2 domains. *Cell.* 128, 901-913.

Cooper, J.A., S.B. Walker, and T.D. Pollard. 1983. Pyrene actin: documentation of the validity of a sensitive assay for actin polymerization. *J. Muscle Res. Cell Motil.* 4, 253-262.

Dent, E.W., A.V. Kwiatkowski, L.M. Mebane, U. Philippar, M. Barzik, D.A. Rubinson, S. Gupton, J.E. Van Veen, C. Furman, and J. Zhang. 2007. Filopodia are required for cortical neurite initiation. *Nat. Cell Biol.* 9, 1347-1359.

Ferron, F., G. Rebowksi, S.H. Lee, and R. Dominguez. 2007. Structural basis for the recruitment of profilin-actin complexes during filament elongation by Ena/VASP. *EMBO J.* 26, 4597-4606.

Fletcher, D.A. and R.D. Mullins. 2010. Cell Mechanics and the cytoskeleton. *Nature.* 463, 485-492.

Gertler, F.B., J.S. Doctor, and F.M. Hoffmann. 1990. Genetic suppression of mutations in the *Drosophila* *abl* proto-oncogene homolog. *Science.* 18; 248(4957):857-860.

Gertler, F.B., K. Niebuhr, M. Reinhard, J. Wehland, and P. Soriano. 1996. Mena, a relative of VASP and *Drosophila* Enabled, is implicated in the control of microfilament dynamics. *Cell.* 87, 227-239.

Gordon, D.J., E. Eisenberg, and E.D. Korn. 1976. Characterization of cytoplasmic actin isolated from *Acanthamoeba castellanii* by a new method. *J. Biol. Chem.* 251, 4778-4786.

Halbrugge, M and U. Walter. 1989. Purification of a vasodilator-regulated phosphoprotein from human platelets. *Eur. J. of Biochem.* v185:41-50.

Halbrugge, M., C. Friedrich, M. Eigenthaler, P. Schanzenbacher, and U. Walter. 1990. Stoichiometric and reversible phosphorylation of a 46-kDa protein in human platelets in response to cGMP- and cAMP-elevating vasodilators. *J. Biol. Chem.* 265(6):3088-3093.

Huttelmaier, S., H. Harbeck, N.O. Steffens, T. MeBerschmidt, S. Illenberger, and B.M. Jockusch, 1999. Characterization of the actin binding properties of the vasodilator-stimulated phosphoprotein VASP. *FEBS letters*. v451:68-74.

Iwasa, J.H. and R.D. Mullins. 2007. Spatial and temporal relationships between actin-filament nucleation, capping, and disassembly. *Curr. Bio*. 17(5):395-406.

Kaiser, D.A., P.J. Goldschmidt-Clermont, B.A. Levine, and T.D. Pollard. 1989. Characterization of renatured profilin purified by urea elution from poly-L-proline agarose columns. *Cell Motil Cytoskeleton* 14, 251-262.

Kaiser, D.A., V.K. Vinson, D.B. Murphy, and T.D. Pollard. 1999. Profilin is predominantly associated with monomeric actin in *Acanthamoeba*. *J. Cell Sci*, 112 (Pt 21):3779–3790.

Kovar, D.R., E.S. Harris, R. Mahaffy, H.N. Higgs, and T.D. Pollard. 2006. Control of the assembly of ATP- and ADP-actin by formins and profilin. *Cell*. 124: 423–435.

Krause, M., J.D. Leslie, M. Stewart, E.M. Lafuente, F. Valderrama, R. Jagannathan, G.A. Strasser, D.A. Rubinson, H. Liu, and M. Way. 2004. Lamellipodin, an Ena/VASP ligand, is implicated in the regulation of lamellipodial dynamics. *Dev. Cell*. 7, 571-583.

Kuhn, J.R. and T.D. Pollard. 2005. Real-Time Measurements of Actin Filament Polymerization by Total Internal Reflection Fluorescence Microscopy. *Biophys. J*. 88:1387-1402.

Kuhn, J.R. and T.D. Pollard. 2007. Single Molecule Kinetic Analysis of Actin Filament Capping. *J. Bio. Chem*. 282(38):28014-28024.

Kuhnel, K., T. Jarchau, E. Wolf, I. Schlichting, U. Walter, A. Wittinghofer, and S.V. Strelkov. 2004. The VASP tetramerization domain is a right-handed coiled coil based on a 15-residue repeat. *PNAS*. 101(49);17027-17032.

Kwiatkowski, A.V., D.A. Rubinson, E.W. Dent, J. Edward van Veen, J.D. Leslie, J. Zhang, L.M. Mebane, U. Philippar, E.M. Pinheiro, and A.A. Burds. 2007. Ena/VASP Is Required for neuritogenesis in the developing cortex. *Neuron*. 56, 441-455.

Lacayo, C.I., Z. Pincus, M.M. VanDuijn, C.A. Wilson, D.A. Fletcher, F.B. Gertler, A. Mogilner, and J.A. Theriot. 2007. Emergence of large-scale cell morphology and movement from local actin filament growth dynamics. *PLoS Biol*. 5,e233.

Lanier, L.M., M.A. Gates, W. Witke, A.S. Mezies, A.M. Wehman, J.D. Macklis, D.

Kwiatkowski, P. Soriano, and F.B. Gertler. 1999. Mena is required for neurulation and commissure formation. *Neuron*. 22(2): 313-25.

Loureiro, J.J., D.A. Rubinson, J.E. Bear, G.A. Baltus, A.V. Kwiatkowski, and F.B. Gertler. 2002. Critical roles of phosphorylation and actin binding motifs, but not the central proline-rich region, for Ena/Vasodilator-stimulated phosphoprotein (VASP) function during cell migration. *Mol. Bio. Cell*. 13: 2533-2546.

Lu, J. and T.D. Pollard. 2001. Profilin Binding to Poly-L-Proline and Actin Monomers along with Ability to Catalyze Actin Nucleotide Exchange Is Required for Viability of Fission Yeast. *Mol. Biol. Cell*. 12, 1161-1175.

Mahaffy, R.E. and T.D. Pollard. 2006. Kinetics of the formation and dissociation of actin filament branches mediated by Arp2/3 complex. *Biophysical Journal*. v91: 3519-3528.

Mahoney, N.M., P.A. Janmey, and S.C. Almo. 1997. Structure of the profilin poly-L-proline complex involved in morphogenesis and cytoskeletal regulation. *Nature Struct. Biol*. 4:953–960.

Mejillano, M.R., S. Kojima, D.A. Applewhite, F.B. Gertler, T.M. Svitkina, and G.G. Borisy. 2004. Lamellipodial versus Filopodial mode of the actin nanomachinery: Pivotal role of the filament barbed end. *Cell*. v118:363-373.

Melki, R., Fievez, S., and M.F. Carlier. 1996. Continuous monitoring of Pi release following nucleotide hydrolysis in actin or tubulin assembly using 2-amino-6-mercapto-7-methylpurine ribonucleoside and purine-nucleoside phosphorylase as an enzyme-linked assay. *Biochemistry*. 17; 35(37): 12038-45.

Miyoshi, T., T. Tsuji, C. Higashida, M. Hertzog, A. Fujita, S. Narumiya, G. Scita, and N. Watanabe. 2006. Actin turnover-dependent fast dissociation of capping protein in the dendritic nucleation actin network: evidence of frequent filament severing. *J. Cell Biol*. 175(6):947-955.

Mogilner, A. and B. Rubinstein. 2005. The physics of filopodial protrusions. *Biophys. J*. 89(2):782-95.

Neel, N.F., M. Barzik, D. Raman, T. Sobolik-Delmaire, J. Sai, A.J. Ham, R.L. Mernaugh, F.B. Gertler, and A. Richmond. 2009. VASP is a CXCR2-interacting protein that regulates CXCR2-mediated polarization and chemotaxis *J. Cell Sci.* 122. 1882-1894.

Palmgren, S., P.J. Ojala, M.A. Wear, J.A. Cooper, and P. Lappalainen. 2001. Interactions with PIP₂, ADP-actin monomers, and capping protein regulate the activity and localization of yeast twinfilin. *J. Cell Biol*. v155(2):251-60

- Pasic, L., T. Kotova, and D.A. Schafer. 2008. Ena/VASP proteins capture actin filament barbed ends. *J. Biol. Chem.* 283, 9814-9819.
- Petrella, E.C., Machesky, L.M., Kaiser, D.A. and T.D. Pollard. 1996. Structural requirements and thermodynamics of the interaction of proline peptides with profilin. *Biochemistry.* 35(51):16535-43.
- Pollard, T.D., L. Blanchoin, and R.D. Mullins. 2001. Actin dynamics. *J. Cell Sci.* 114, 3-4.
- Pollard, T.D. and G.G. Borisy. 2003. Cellular motility driven by assembly and disassembly of actin filaments: integration of signals to the Arp2/3 complex. *Cell.* 112, 453–465.
- Prehoda. K.E., D.J. Lee, and W.A. Lim. 1999. Structure of the Enabled/VASP Homology 1 Domain–Peptide Complex: A Key Component in the Spatial Control of Actin Assembly. *Cell.* 97, 471-480.
- Rasnik, I., S.A. McKinney, and T. Ha. 2006. Nonblinking and long-lasting single-molecule fluorescence imaging. *Nature Methods.* 3(11), 891-893.
- Rottner, K., B. Behrendt, J.V. Small, and J. Wehland. 1999. VASP dynamics during lamellipodia protrusion. *Nature Cell Biol.* 1: 321–322
- Stuurman, N., N. Amodaj, and R.D. Vale. 2007. μ Manager: Open Source software for light microscope imaging. *Microscopy Today* 15: 42-43.
- Svitkina, T.M., E.A. Bulanova, O.Y. Chaga, D.M. Vignjevic, S. Kojima, J.M. Vasiliev, and G.G. Borisy. 2003. Mechanism of filopodia initiation by reorganization of a dendritic network. *J. Cell Biol.* v160(3): 409-421.
- Tomishige, M., D.R. Klopfenstein, and R.D. Vale. 2002. Conversion of Unc104/KIF1A Kinesin into a Processive Motor After Dimerization. *Science.* 297.
- Vignjevic, D., S.I. Kojima, Y. Aratyn, O. Danciu, T.M. Svitkina, and G.G. Borisy. 2006. Role of fascin in filopodial protrusion. *J Cell Biol.* 174(6), 863-875.
- Vinson, V.K., De La Cruz, E.M., Higgs, H.N., and T.D. Pollard. 1998. Interactions of *Acanthamoeba* profilin with actin and nucleotide bound to actin. *Biochemistry.* 37(31):10871-80.
- Welch, M.D. and R.D. Mullins. 2002. Cellular control of actin nucleation. *Annu. Rev. Cell Dev. Biol.* 18:247–88.

Figure Legends

Figure 1

Cy3-KCK-hVASP^{CCC-SSA} and unlabeled hVASP are functionally equivalent.

(A) Domain architecture of Cy3-KCK-hVASP^{1-380aa} (C7S, C64S, C334A). (B) Cosedimentation of 2 μ M filamentous actin with VASP, KCK-VASP, or Cy3-KCK-VASP (0-5 μ M monomeric concentrations). (C) As judged by pyrene fluorescence, VASP and Cy3-VASP (63 nM tetrameric/250 nM monomeric) equally enhance the polymerization of 2 μ M actin (5% pyrene labeled). (D) Concentration dependent increase in the barbed end polymerization rate of 1 μ M Mg-ATP-actin (30% Alexa488, 50-100 mM KCl) in the presence of VASP or Cy3-VASP. Error bars indicate standard deviation ($n \geq 30$ filaments from ≥ 2 slides).

Figure 2

Mechanisms regulating the interaction between VASP and filamentous actin.

(A) Localization of single Cy3-VASP tetramers (arrows) binding to phalloidin stabilized Alexa488 actin filaments. Bottom panel shows the maximum intensity projection (*M.I.P*) of 0.25 nM Cy3-VASP (500 frames) bound to filamentous actin. Scale bar = 5 μ m. (B) Multi-step photobleaching of a Cy3-VASP tetramer ($\tau_1=11.5\pm 0.07$ sec for a single Cy3 fluorophore, $n=229$ molecules; data not shown). (C) Kymograph of 0.25 nM tetrameric Cy3-VASP bound to an actin filament in TIRF buffer plus oxygen scavenger (see Methods). Vertical scale bar = 2 sec. Horizontal scale bar = 5 μ m. (D-E) Dwell times for Cy3-VASP binding to

filamentous actin. **(D)** Double exponential fit of 1-cumulative frequency (C.F.) for all binding modes. **(E)** Single exponential fit of molecules exhibiting diffusive binding mode. **(F)** Localization of 0.25 nM Cy3-VASP (*M.I.P.*), wild-type and mutants, binding to phalloidin stabilized Alexa488 actin filaments. Scale bar = 5 μm . **(G)** Kymographs of 0.25 nM Cy3-VASP, GAB mutants (Cy3-VASP^{L226A,I230A,L235A} and Cy3-VASP^{R236E,K237E}), and Cy3-VASP plus 2 μM Mg-ATP-actin (+10 μM Latrunculin B) binding to actin filaments. Vertical scale bar = 2 sec. Horizontal scale bar = 5 μm . **(H)** Double exponential fits of 1-C.F. for GAB mutants and Cy3-VASP plus 2 μM Mg-ATP-actin (+LatB). Percentage of molecules with each characteristic dwell time are printed in parentheses.

Figure 3

Mechanism for VASP barbed end capture.

(A) Kymograph showing Cy3-VASP barbed end association in the absence (left) or presence (right) of 2 μM Mg-ATP-actin (+10 μM LatB). Vertical scale bar = 1 sec. Horizontal scale bar = 2.5 μm . **(B)** Barbed end localization of single Cy3-VASP tetramer (arrowhead) in the presence of 2 μM Mg-ATP-actin/LatB. Scale bar = 2.5 μm . **(C)** Binding frequencies for Cy3-VASP at different filament positions in the presence or absence of 2 μM Mg-ATP-actin/LatB and/or 5 nM *MmCP*. VASP (V); Actin (A); capping protein (CP). Pixel position 1 is the apparent barbed end; positions 2-10 are actin filament sides. For experiments including *MmCP*, filaments were capped for 5 min before adding Cy3-VASP and 5 nM *MmCP* (≥ 200 events scored per condition). **(D)** Dwell times for 0.25 nM

Cy3-VASP binding to the apparent barbed end versus the sides of actin filaments in the presence of 2 μM actin/LatB, plus or minus 5 nM *MmCP*. (E) Life history of a single actin filament elongating in the presence of 0.75 μM actin (30% Alexa488). Scale bar = 10 μm . (F) The binding frequency of 0.25 nM Cy3-VASP ($n=1045$ molecules) is independent of the probability of the ADP- P_i nucleotide state at each position. (G) Single molecule dwell times for 0.25 nM Cy3-VASP binding to regions of filamentous actin with $p(\text{ADP-}\text{P}_i) \geq 0.5$ or $p(\text{ADP-}\text{P}_i) \leq 0.5$ were fit to a single exponential ($p(\text{ADP-}\text{P}_i) \geq 0.5$, $\tau_1 = 0.93 \pm 0.01$ sec, $n=235$; $p(\text{ADP-}\text{P}_i) \leq 0.5$, $\tau_1 = 1.0 \pm 0.01$ sec, $n=1135$). (H) Localization of 2.5 nM Cy3-VASP bound to an ADP- P_i /ADP actin filament (3-17 min old). Scale bar = 10 μm . (I) Intensity profile of Cy3-VASP bound to actin filament in (H), overlaid with probability distribution of the ADP- P_i nucleotide state. The probability distribution of each nucleotide state was solved numerically in MatLab (Fig. S 4A).

Figure 4

Processivity of barbed end associated VASP tetramers.

(A) Actin filament lengths before and after burst phase imaging of 0.25 nM Cy3-VASP in the presence of 1 μM Mg-ATP-actin (30% Alexa488). Maximum intensity projections of 0.25 nM Cy3-VASP (1000 frames) superimposed on the Alexa488 actin filament ($t=100$ sec). Scale bar = 5 μm . (B). Barbed end localization of Cy3-VASP (middle image; white arrow) merged with maximum intensity projection of Cy3-VASP actin filament binding (frames 1-387; top image). Two molecules are also laterally bound to the actin filament (white

arrowheads). Scale bar = 5 μm . (C) Representative kymographs showing single Cy3-VASP tetramers processively tracking on actin filament barbed ends. Kymographs from left to right show molecules with increasing processivity. The dashed line connecting two processive VASP tetramers has a slope equivalent to a ~ 10 sub/sec barbed end elongation rate in the absence of VASP. Arrowheads point to molecules transiently binding to ATP/ADP- P_i actin, near barbed ends ($\tau_1=0.22\pm 0.01$ sec, $n=280$). Vertical scale bar = 5 sec. (D) Magnification of dashed line box in (C) showing: (1) side binding, (2) diffusion toward barbed end, and (3) barbed end attachment and surfing of Cy3-VASP. Horizontal scale bar = 2 μm . Vertical scale bar = 2.5 sec. (E) Histogram of barbed end dwell times measured in the presence of 0.25 nM Cy3-VASP and 1 μM actin (30% Alexa488). Inset plot is an exponential fit of 1-C.F. ($\tau_1=1.45\pm 0.02$ sec, $n=1166$). (F) Time series for a highly processive Cy3-VASP tetramer tracking an actin filament barbed end. (G) Barbed end growth rates measured in the presence of 1 μM Mg-ATP-actin (30% Alexa488), plus varying concentrations of VASP. Data fit to Michaelis-Menten equation with a y-axis offset of 10 ($K_d= 9.2\pm 1.4$ nM). (H) Barbed end polymerization rates in the presence of 0-50 nM VASP, plus 0.25-2 μM Mg-ATP-actin (30% Alexa488). (I) Barbed end dwell times for 0.25 nM Cy3-VASP in the presence of 0.5-2 μM Mg-ATP-actin. The number of actin monomers delivered to the barbed end by single VASP tetramers is the product of the barbed end dwell time and the polymerization rate from (H).

Figure 5

VASP enhances barbed end polymerization in the presence of profilin-actin.

(A) Interaction between Cy3-VASP^{1-240aa} and human profilin I measured by sedimentation equilibrium. Equilibrium traces from left to right: 5 μ M Cy3-VASP^{1-240aa} plus 30, 60, or 90 μ M hProI. A predicted size of 24.8 kDa for Cy3-VASP^{1-240aa} alone, closely matched the observed MW = 24.5 kDa (data not shown). Based on a global fit of all traces, Cy3-VASP^{1-240aa} interacts with two hProI proteins (MW_{pred} = 15 kDa per hProI). (B) Barbed end growth rates measured in the presence of 1, 1.5, 2 μ M profilin-actin (10% Alexa488), plus 50 nM VASP. Mutations made to profilin or VASP are indicated with yellow stars. From left to right: (1) hPro1-Actin alone, (2) hPro1^{H133S}-Actin, (3) hPro1-Actin-VASP, (4) hPro1^{H133S}-Actin-VASP, (5) hPro1-Actin-VASP^{PPPLPAP-8A}, (6) hPro1-Actin-VASP^{GAB*(LIL-AAA)}, (7) hPro1^{H133S}-Actin-VASP^{GAB*(LIL-AAA)}, (8) hPro1-Actin-VASP^{FAB*(RRRK-4E)}. (C) Barbed end filament growth rates in the presence of 2 μ M Profilin-actin, 100 mM KCl, and 0-50 nM VASP. (D-E) Barbed end dwell times for Cy3-VASP measured in the presence hPro1-actin and hPro1^{H133S}-actin. (E) The number of actin monomers delivered to the barbed end equals the product of the polymerization rate (Fig. 5 B) and dwell time (Fig. 5 D).

Figure 6

VASP antagonizes capping protein barbed end association in the presence of profilin-actin.

(A) Actin filament length distribution after 5 min of barbed end growth in the presence of 2 μM Mg-ATP-actin (10% Alexa488), 2 μM hPro1, 0-20 nM MmCP, and 0-50 nM VASP. Scale bar = 10 μm . (B) Average number of actin subunits delivered to barbed end before termination of growth by MmCP. The dash line represents the predicted actin filament length if the filaments had been elongating 2.4-times faster than 2 μM profilin-actin alone ($n \geq 100$ filaments). (C) Rate of actin filament capping in the presence of 2 μM Mg-ATP-actin (10% Alexa488), 2 μM hPro1, 2-4 nM MmCP, and 0-50 nM VASP. Calculation of K_{obs} was achieved by fitting data to $[\text{BE}]_{\text{free}} \cdot \exp^{(-k/\tau_1)}$ equation in KaleidaGraph ($n \geq 150$ filaments tracked). (D) Plot of K_{obs} (sec^{-1}) versus MmCP concentration. The slope gave an capping protein association rate constant of 12 $\mu\text{M}^{-1} \text{sec}^{-1}$ and 1.9 $\mu\text{M}^{-1} \text{sec}^{-1}$, in the absence or presence of 50 nM VASP respectively.

Figure 7

Model for VASP barbed end association.

In the absence of monomeric actin (right side) the GAB and FAB domains of VASP contribute to actin filament binding. VASP binds with equal affinity along the sides and near the ends of the filament. Apparent barbed end association of VASP alone is indistinguishable from lateral interaction with filamentous actin. When the GAB domain is bound to monomeric actin (left side), binding to the sides of filaments is weakened and the bound actin monomer allows VASP to capture an actin filament barbed end. Note: Although the mechanism described occurs in the context of a VASP tetramer, a single subunit is drawn for simplicity.

Supplemental Figure 1

Cy3-VASP GAB and FAB domain mutants.

(A) Cartoon of VASP structure highlighting the GAB and FAB domain amino acid sequences. Point mutations made for this study are shown in red print. (B) G-actin or F-actin binding domain mutants (50nM VASP) do not enhance barbed end filament elongation in the presence of 1 μ M actin (30% Alexa488). (C-D) Localization of 2.5 nM Cy3-VASP (wild-type or mutants) on phalloidin stabilized Alexa488 actin filaments. (C) Colocalization of the Cy3-VASP (maximum intensity projection, 500 frames) with Alexa488 actin. (D) Kymograph of Cy3-VASP or mutants bound to an actin filament. (E-H) Localization of 5 nM Cy3-VASP (wild-type or mutants) to sites of filament overlap during polymerization of 1 μ M Actin (30% Alexa488) (E) Cy3-VASP, (F) Cy3-VASP^{L226A,I230A,L235A}, (G) VASP^{R236E,K237E}, (H) VASP^{RRRK—EEEE}. Scale bar = 5 μ m.

Supplemental Figure 2

Salt dependence of Cy3-VASP actin filament binding, barbed end polymerization, and anti-capping.

(A-C) Interactions between Cy3VASP and filamentous actin are weakened in high ionic strength buffers. (A) Top image is phalloidin stabilized Alexa488 actin filament. Scale bar = 5 μ m. Below are maximum intensity projections (1000 frames, 50 ms intervals) of 0.5 nM tetrameric Cy3-VASP binding to the side of an actin filament. Starting with 100 mM KCl, 0.5 nM Cy3-VASP was flowed into the TIRF chamber and imaged. Sequentially, 0.5 nM Cy3-VASP diluted into TIRF

buffer containing a lower KCl concentrations was flowed into the TIRF cell. The concentration of the Cy3-VASP remain constant throughout the experiment. (B) Kymographs of 0.5 nM Cy3-VASP binding to the side of the actin filament shown in (A), at different KCl concentrations (1-100 mM). Vertical scale bar = 1 sec. Horizontal scale bar = 5 μ m. (C) Localization of 10nM Cy3-VASP to sites of filament bundling in the presence of 50 mM or 100 mM KCl. Cy3-VASP localizes to the sides of single filaments and bundles in the presence of 50 mM KCl. In the presence of 100 mM KCl, an interaction between Cy3-VASP and single actin filaments is difficult to detected. Localization to sites of filament bundling were still visible in high salt, but to a lesser extent. Arrowheads mark filament bundles, while asterisks mark single actin filaments. Scale bar = 20 μ m. (D) VASP antagonizes capping protein barbed end association in the presence of 100 mM KCl. (i). Average filament length distribution after 5 min of barbed end growth in the presence of 2 μ M monomeric actin (10% Alexa488), 2 μ M profilin, 0-20 nM MmCP α 1 β 2, and 0-50 nM VASP. Scale bar = 10 μ m. The dash line represents the predicted actin filament length if the filaments had been elongating 1.9-times faster than 2 μ M profilin-actin alone ($n \geq 100$ filaments were measured for each condition). (ii) Plot of K_{obs} (sec^{-1}) versus the concentration of MmCP α 1 β 2. The slope produced a capping protein association rate constant of 10 $\mu\text{M}^{-1}\text{sec}^{-1}$ and 3.7 $\mu\text{M}^{-1}\text{sec}^{-1}$, in the absence or presence of 50 nM VASP respectively. (iii-iiii) Plots showing the fraction of capped barbed end over time in the presence of 2 μ M monomeric actin (10% Alexa488), 2 μ M profilin, 1-8 nM MmCP, and 0-50 nM VASP. Calculation of K_{obs} was achieved by fitting data to $[\text{BE}]_{\text{free}} * \exp^{(-k/ \tau)}$

exponential equation in KaleidaGraph ($n \geq 150$ filaments tracked for each condition).

Supplemental Figure 3

Cy3-VASP C-terminal fragment does not capture barbed ends.

(A) Compared localization for 50 nM tetrameric Cy3-VASP, Cy3-VASP^{280-380aa}, GST-Cy3-VASP^{280-380aa}, and Cy3-VASP^{(L226A,I230A,L235A)/(RRRK-4A)} binding to the side of Alexa488 actin filaments. Scale bar = 5 μ m. (B) Schematic showing how Cy3-VASP barbed end association events were visualized. Field of dual colored actin filaments (red, Alexa568 phalloidin stabilized seeds; green, 40% Alexa488 actin filaments). Dual colored seeds were generated by polymerizing 0.5 μ M monomeric actin (40% Alexa488 labeled; green) off 20 nM Alexa568-phalloidin stabilized actin filaments (red) for 3 min. Dual colored seeds were then flowed into the TIRF chamber, captured by biotin-HMM, and chased with 1 μ M dark phalloidin to prevent barbed end depolymerization. Next, 0.5 nM Cy3-VASP was flowed into the TIRF chambers and imaged. Using the 488/568 F-actin image, we determine contour of the actin filament and then generated a kymograph of the Cy3-VASP time series at those positions. (C) Cy3-VASP^{280-380aa} does not capture actin filament barbed end. Kymograph showing the localization of Cy3-VASP^{280-380aa} compared to Cy3-VASP binding to the side of the actin filament. Dual colored actin filaments, as in (B), were used for these experiments. Vertical scale bar = 5 sec. Horizontal scale bar = 2.5 μ m. (D) The rate of barbed end filament growth is not inhibited by VASP C-terminal fragment or GAB/FAB double

mutant. 1.5 μM actin (30% Alexa488 labeled) was polymerized in the presence of 50 nM VASP, Cy3-VASP, Cy3-VASP^{280-380aa}, GST-Cy3-VASP^{280-380aa}, or Cy3-VASP^{(LIL-3A)/(RRRK-4A)}. Error bars indicate standard deviation ($n \geq 20$ filaments).

Supplemental Figure 4

Nucleotide dependence of VASP binding to filamentous actin.

(A) Model of nucleotide hydrolysis and inorganic phosphate release from filamentous actin. Rate constants: $k_1 = 0.035 \text{ sec}^{-1}$ (ATP hydrolysis) and $k_2 = 0.0026 \text{ sec}^{-1}$ (phosphate release) were obtained from Melki et al., (1996). Using MatLab, a half-life of 296 seconds was calculated for release of inorganic phosphate following ATP hydrolysis. (B) Representative images of actin filaments polymerizing in the presence of 0.75 μM Actin (30% Alexa 488 labeled). Following ~20 minutes of actin filament growth, filaments were washed and capped with 5 nM MmCP $\alpha 1\beta 2$. Subsequently, 0.25 nM Cy3-VASP and 5 nM MmCP $\alpha 1\beta 2$ were flowed into the TIRF chamber. The localization of laterally associated Cy3-VASP was followed by burst phase imaging. Scale bar = 20 μm . (C) Representative kymograph of 0.25 nM Cy3-VASP binding to actin filaments described in (B). Based on the (x,y) coordinates of the Cy3-VASP landing position, we calculated position along the length of the filament (x) and extra time between filament growth and binding of Cy3-VASP in the kymograph (y). From the sum of the filament age, time from filament capping to burst imaging, and the Cy3-VASP landing time (y-axis in kymograph) we calculated the filament age at the time of Cy3-VASP binding. The age of the filament was then correlated to the

probability of the ADP-P_i or ADP nucleotide state at each position. Vertical scale bar = 5 sec. Horizontal scale bar = 10 μm.

Supplemental Figure 5

Localization of Cy3VASP during actin filament bundling.

(A-B) Localization of Cy3-VASP during actin filament bundling. 1 μM actin (30% Alexa488) was polymerized in the presence of 5 nM Cy3-VASP. (A) Parallel and (B) anti-parallel filament bundles. Arrows marks the barbed ends and direction of filament elongation. Scale bar = 5μm. (C) Line scan of Cy3-VASP intensity on a single and bundled actin filaments. (D) Quantification of Cy3-VASP intensity on single verses bundled actin filaments. The fold increase per filament was determined by measuring the peak pixel intensity and then subtracting the background signal directly adjacent to the filament of interest. Compared to single filaments, we observe a 28-30% increase in Cy3-VASP fluorescence per filament at sites of bundling.

Supplemental Figure 6

VASP binding capacity for monomeric actin.

Sedimentation equilibrium data. (A) Model for effect of occupancy on binding of successive actin monomers to one VASP tetramer. (B) The change in mean squared error (MSE) between raw data and model fit (compared to the minimum MSE) as a function of both K_a and b. (left) Three dimensional plot. (right) Contour plot of the MSE versus K_a and b. The optimum values of the two

parameters are $K_a=1.11$ and $b=0.2125$. Converting the affinity to units of concentration yields K_d s for the four sites of: 0.43, 2.0, 9.5, and 45 μM . **(C)** Best fit of the binding model to data collected at three speeds with 2 μM and 25 μM monomeric actin.

Figure 1

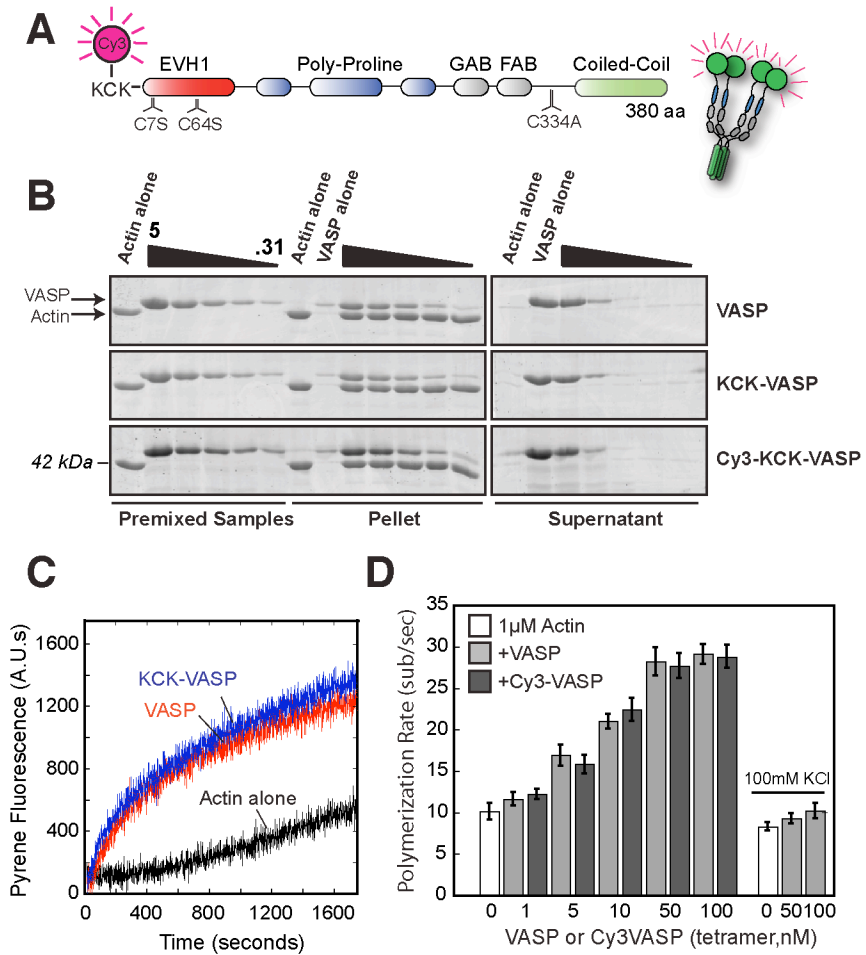


Figure 2

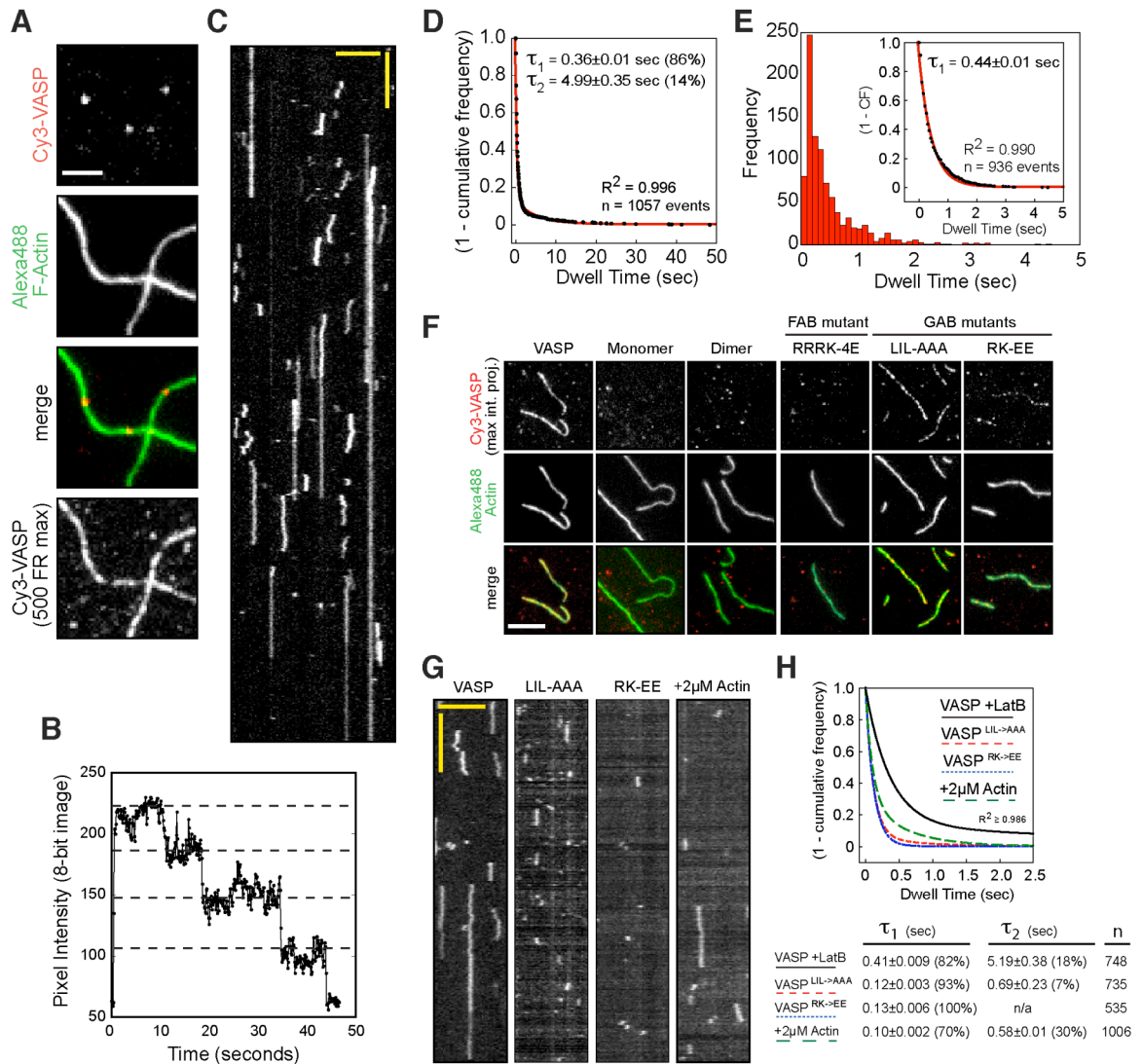


Figure 3

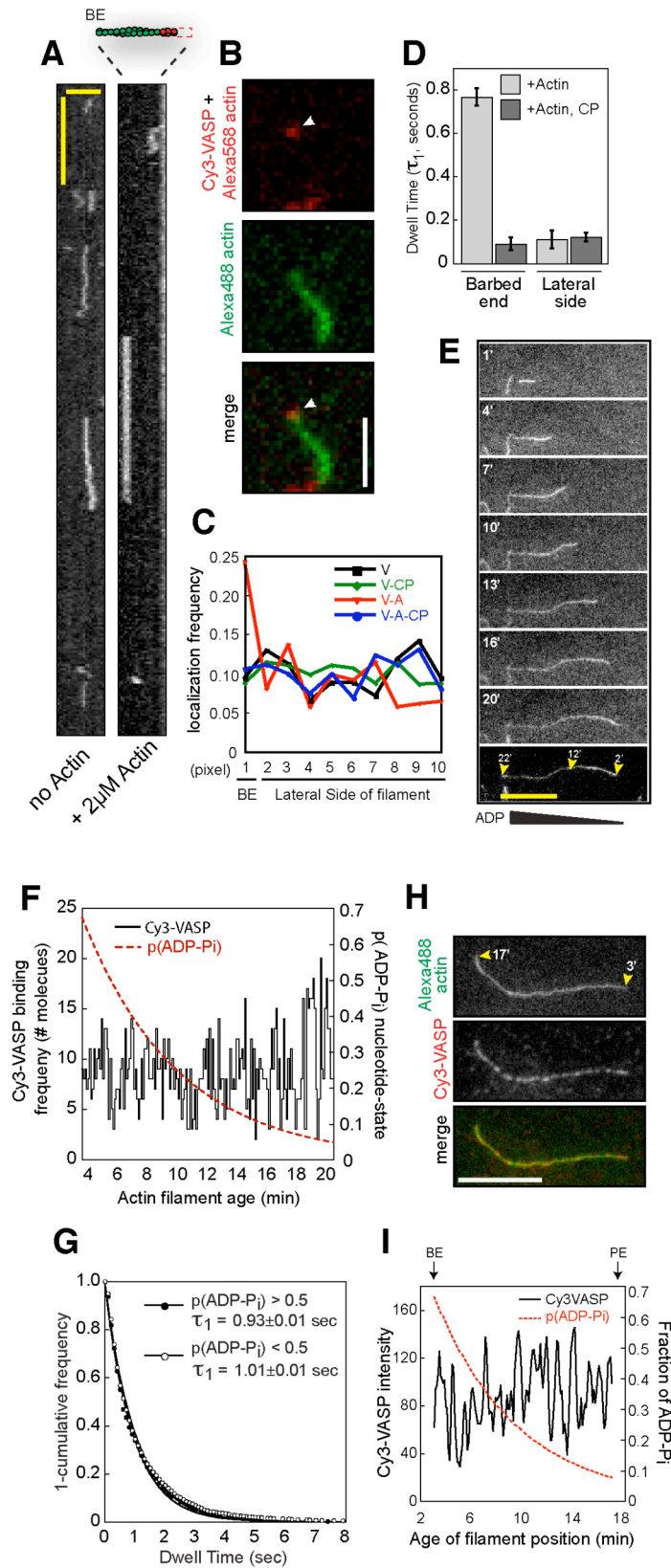


Figure 4

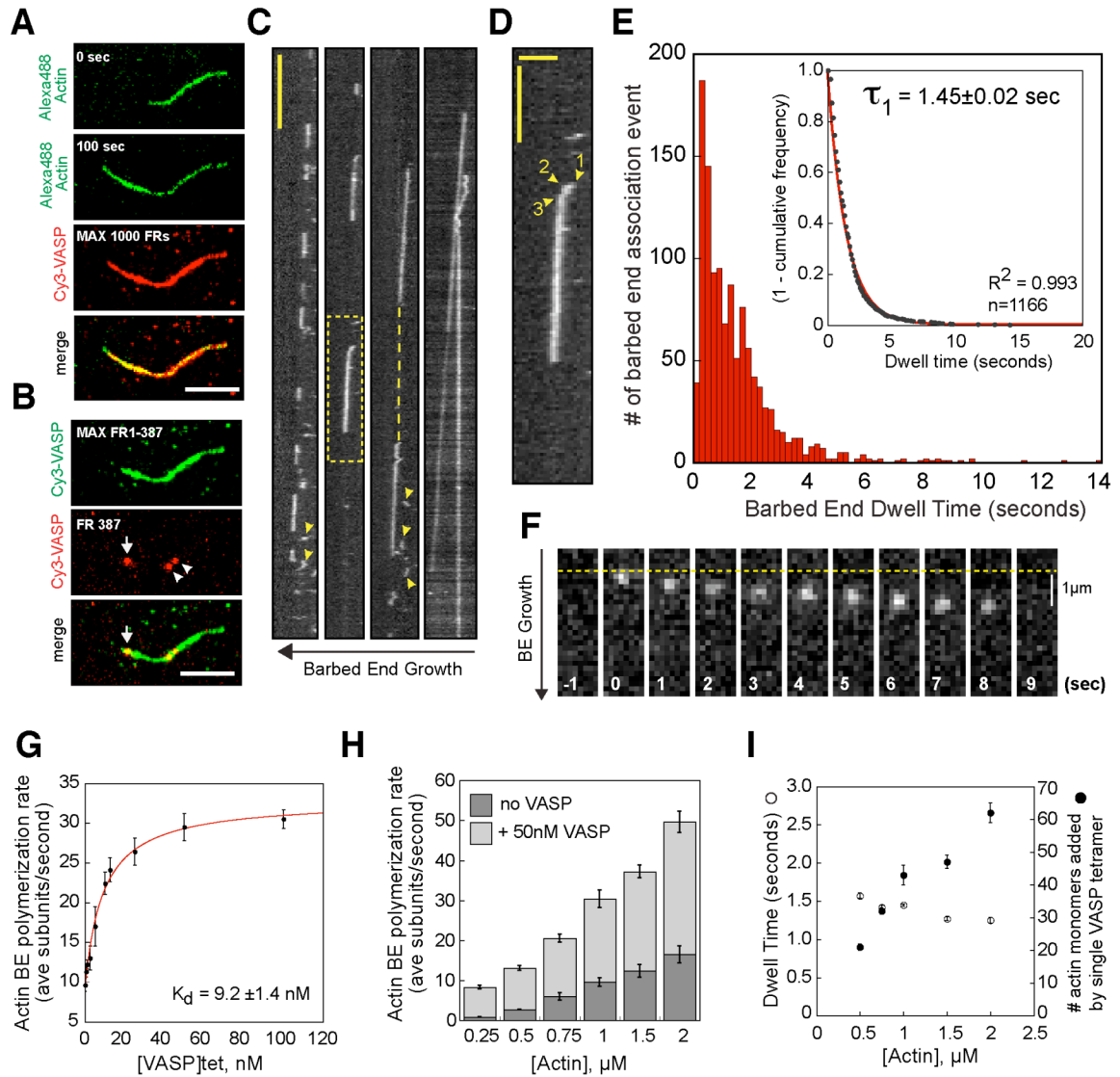


Figure 5

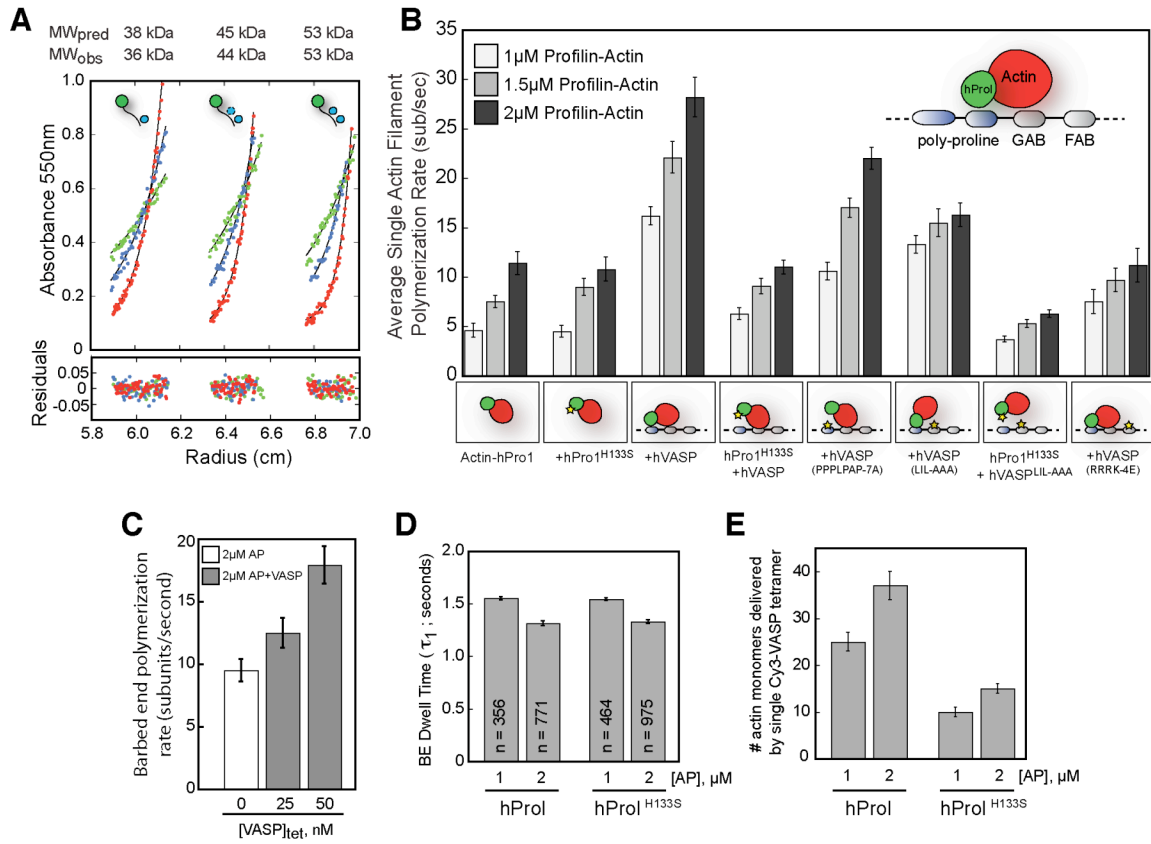


Figure 6

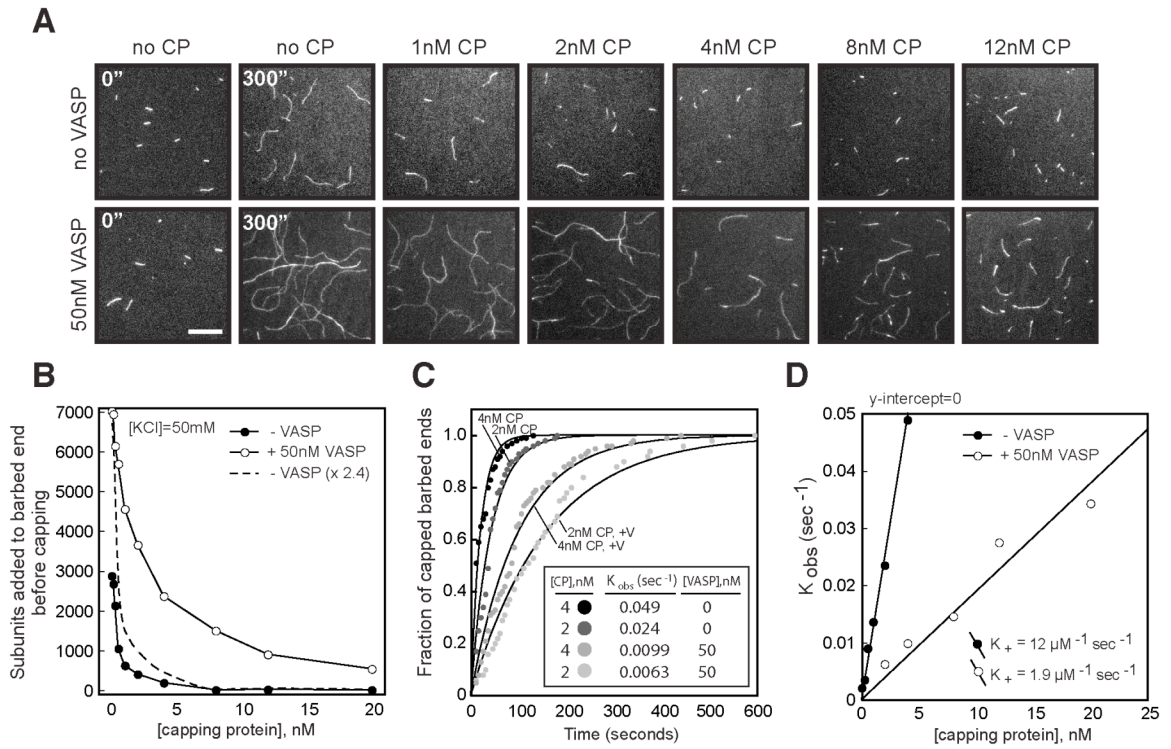


Figure 7

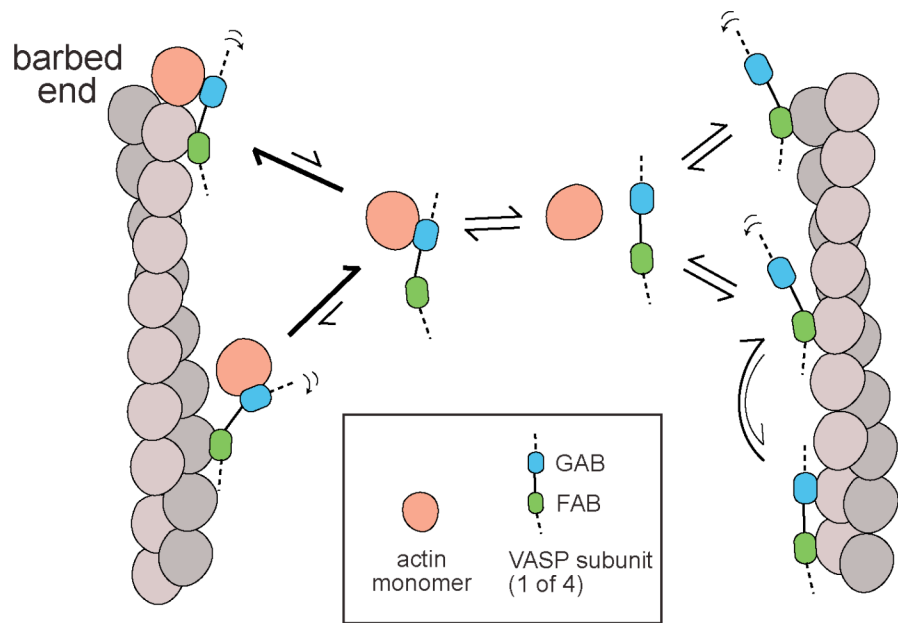


Figure S1

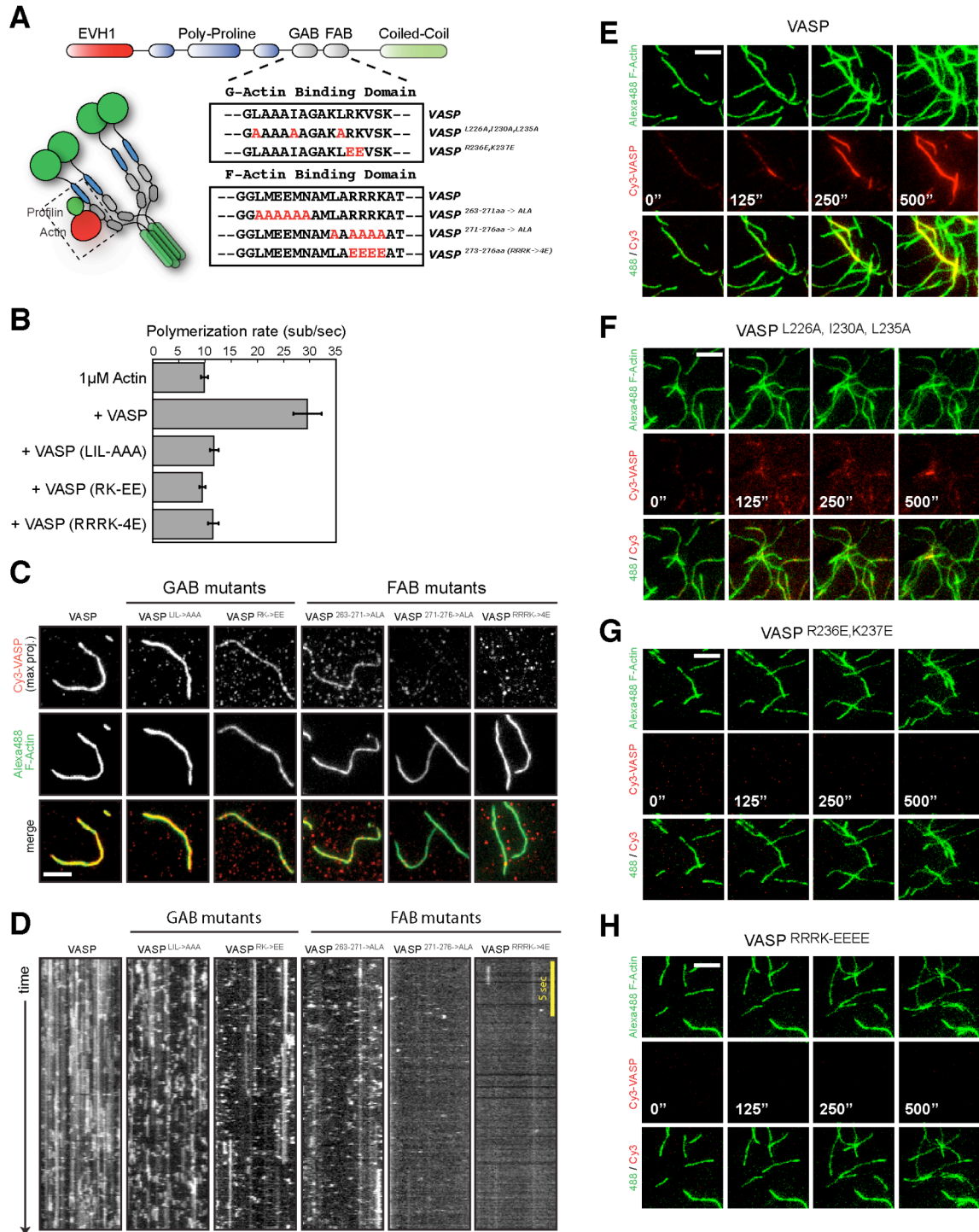


Figure S2

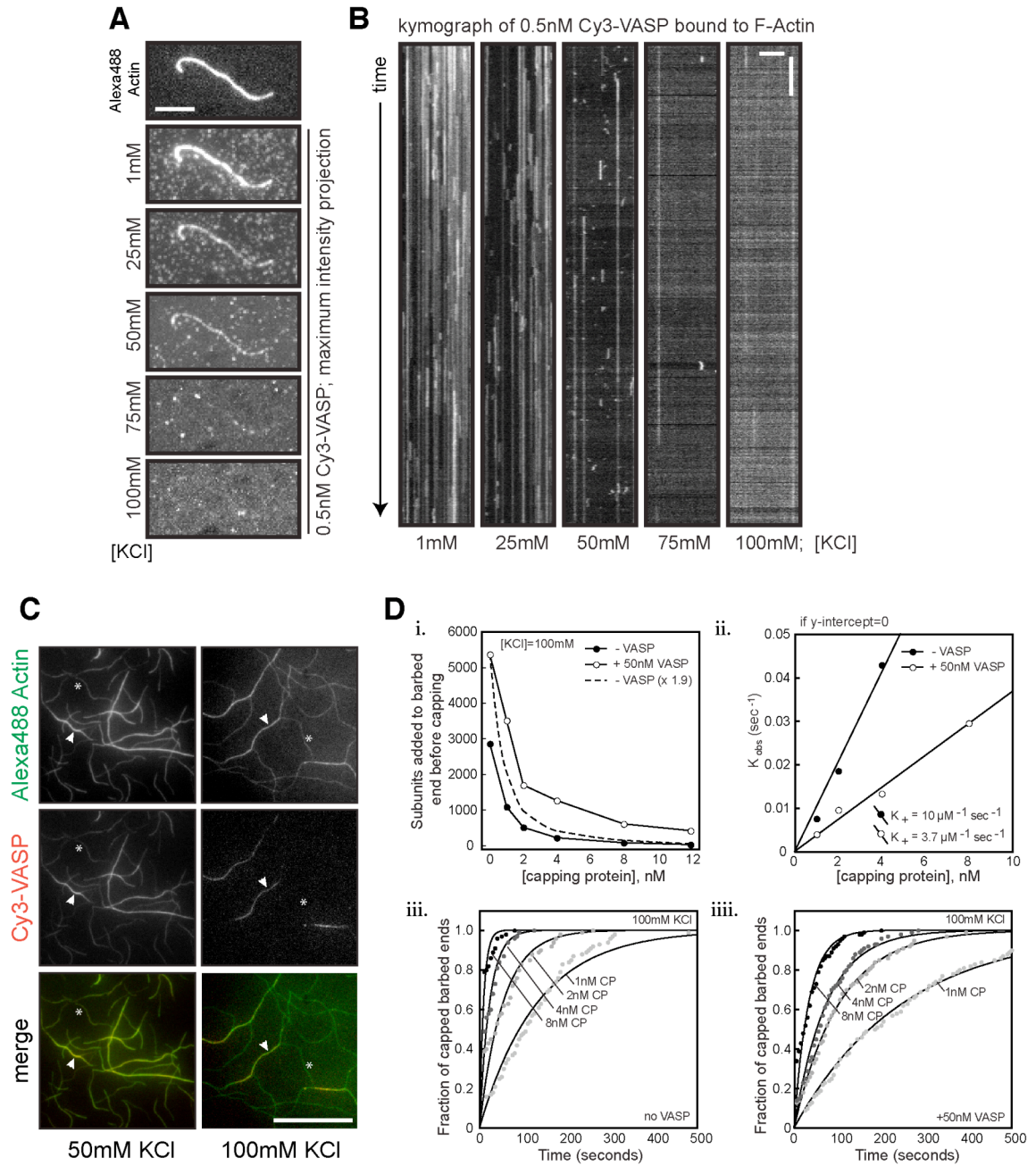


Figure S3

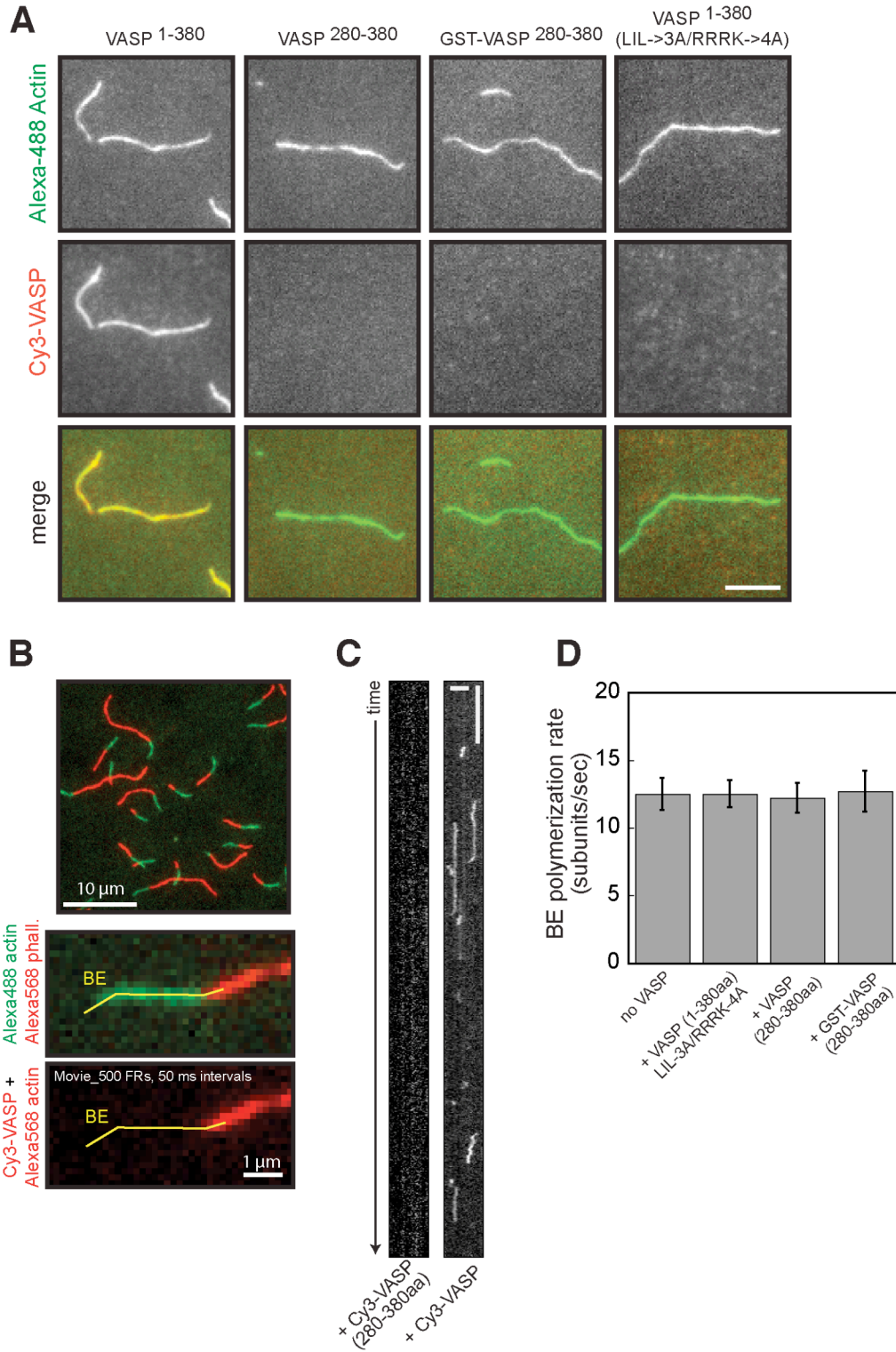


Figure S4

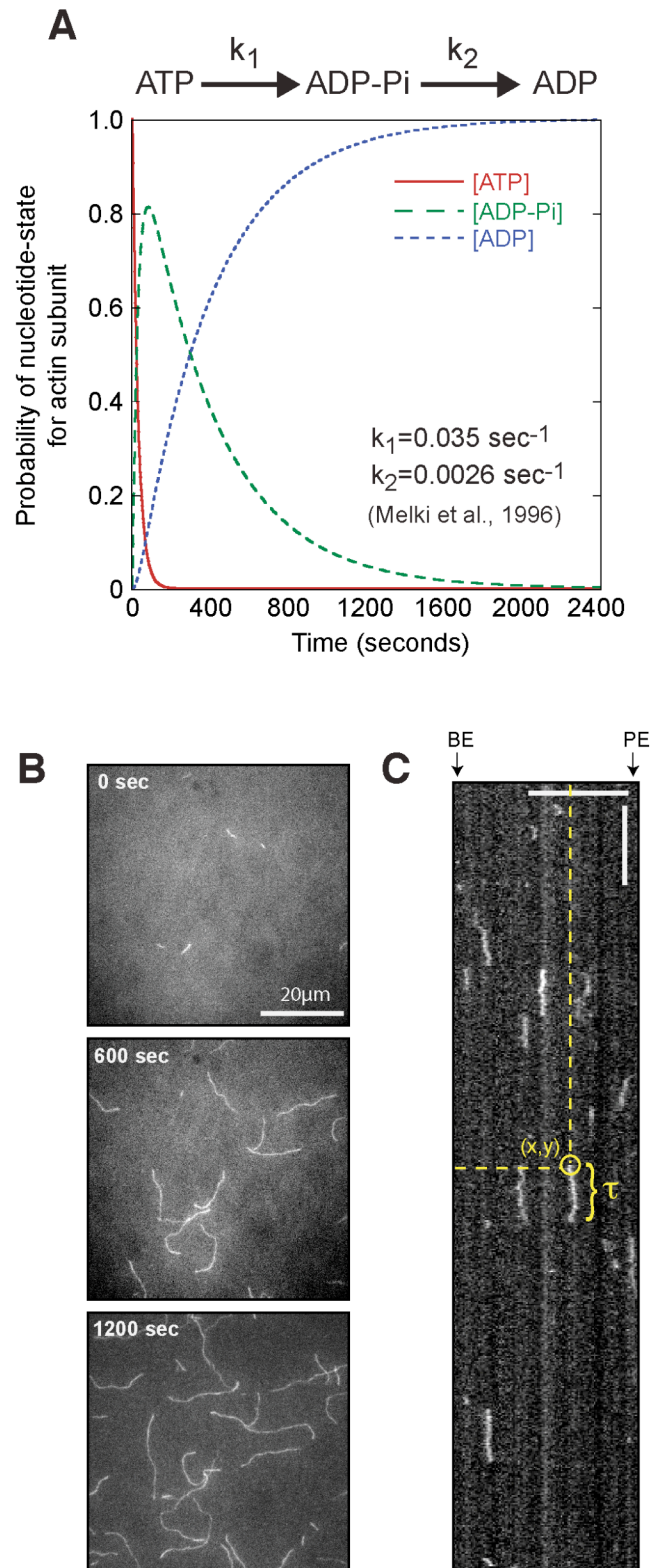
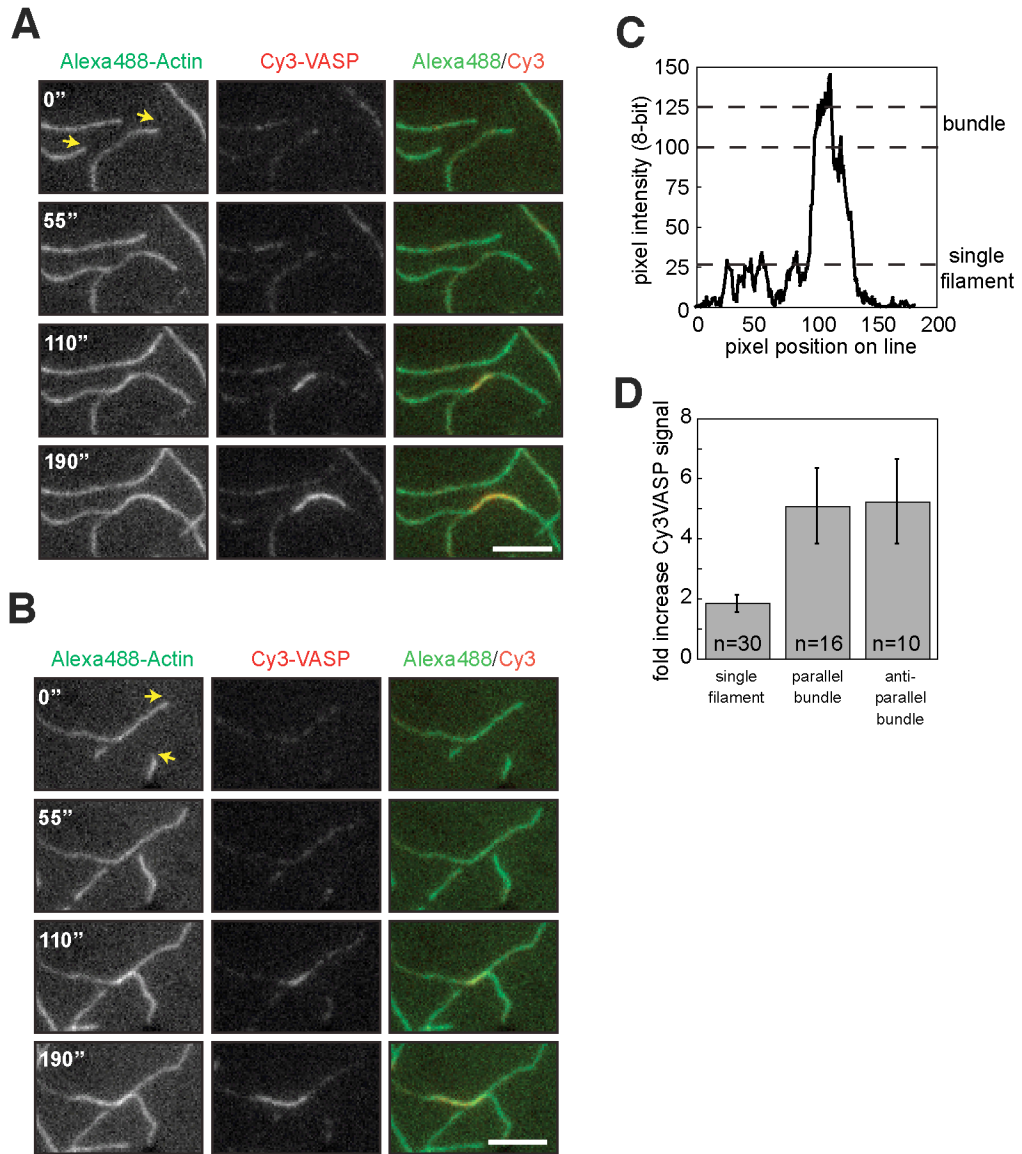


Figure S5



Chapter 3

Modulation of Ena/VASP processivity by a membrane tethered
actin binding protein

Scott D. Hansen and R. Dyche Mullins

In preparation for submission to *Journal of Cell Biology*

Abstract

Actin polymerases of the Ena/VASP protein family promote actin filament barbed end elongation. They are dynamically localized to leading edge membranes where they play an important role in determining the architecture of the underlying actin network. Although Ena/VASP proteins are intrinsically processive actin barbed end polymerases *in vitro*, this activity is not sufficient for membrane targeting *in vivo*. Instead, the combined presence of growing actin filament barbed ends together with a membrane tethering protein are required for persistent membrane association of Ena/VASP proteins *in vivo*. The molecular mechanisms by which growing barbed ends and membrane tethering proteins synergistically contribute to Ena/VASP protein localization, lifetime, and/or activity at the plasma membrane, however, remain unclear. We present evidence that Lamellipodin, a membrane-associated Ena/VASP tethering protein, can autonomously bind to and organize actin filaments *in vitro*. In addition, Lamellipodin can enhance Ena/VASP barbed end processivity *in vitro* by a clustering independent mechanism that requires the interaction with filamentous actin. We propose that the filament binding activity of Lamellipodin acts as part of a “barbed end sensor” that rapidly and efficiently delivers Ena/VASP proteins to growing filament ends. To test this hypothesis, we characterized interactions between Lamellipodin, VASP, and actin filaments *in vivo* and *in vitro*, using biomimetic assays of varying degrees of complexity. This work provides insight about how membrane tethered actin barbed end polymerases control the assembly of the actin cytoskeleton during cell migration and morphogenesis.

Introduction

Assembly of the actin cytoskeleton during polarized cell migration and morphogenesis is largely dependent on the spatiotemporal localization of proteins at the plasma membrane. At the barbed end attachment zone, competition between actin filament elongation factors and capping protein regulates the organization of the actin cytoskeleton. Changes in the lifetime, activity, and concentration of these proteins determines whether filaments persistently elongate or are terminated shortly after nucleation. Regulation of such proteins can result in changes in the actin filament length distribution and branch density. Although actin barbed end polymerases of the Ena/VASP protein family can antagonize capping protein *in vivo* and *in vitro* (Bear et al., 2002; Barzik et al., 2005; Breitsprecher et al., 2008; Hansen and Mullins, 2010), little is known about how their localization, lifetime, and activity are regulated at the plasma membrane.

Actin barbed end polymerases of the Ena/VASP protein family function to orient, elongate, and protect growing actin filament ends from capping protein. The extent to which these proteins localize to the plasma membrane can dramatically affect the architecture of the underlying actin cytoskeleton (Bear *et al.*, 2002; Lacayo *et al.*, 2007). Constitutive plasma membrane localization of Ena/VASP proteins produces long-linear actin filaments, which negatively regulate the membrane protrusion frequency and the speed by which fibroblast migrate (Bear et al., 2000). Similarly, overexpression of MENA or VASP can

result in a dose dependent decrease in cell migration speed (Bear et al., 2000). Conversely, recruitment of Ena/VASP proteins away from the plasma membrane, via a FPPPP-mitochondrial targeting peptide, increases membrane protrusion and cell migration speeds (Bear et al., 2000). Depending on the lifetime, concentration, and activity of Ena/VASP proteins at the plasma membrane different actin network architectures and cell migration behaviors can be observed.

Although Ena/VASP proteins are intrinsically processive actin barbed end polymerases *in vitro* (Hansen and Mullins, 2010), cell biological data suggests that a combination of free actin filament barbed ends and a membrane tethering protein are required for persistent plasma membrane localization. *In vivo*, pharmacological capping of actin filament barbed ends with cytochalasin D, rapidly delocalizes plasma membrane associated Ena/VASP proteins (Krause et al., 2005; Lacayo et al., 2007; Neel et al., 2009). In addition, removal of the N-terminal EVH1 domain of Ena/VASP results in loss of focal adhesion and plasma membrane localization in fibroblasts (Loureiro et al., 2002). Interestingly, monomeric GFP-EVH1 weakly localizing to the leading edge and focal adhesions in Rat2 and Ena/VASP null MV^{D7} cells (Bear et al., 2000). This leading edge localization of GFP-EVH1 can also be observed in the presence of ≤ 400 nM cytochalasin D and is therefore independent of actin filament barbed ends (Bear et al., 2002). In contrast, the minimal domain that can support Ena/VASP barbed end processivity, GFP-EVH2, fails to localize at focal adhesions and is broadly distributed across the lamellipodial actin network without being concentrated at

the plasma membrane (Bear et al., 2002). Although the EVH2 domain is sufficient for localization to the lamellipod, sustained and concentrated localization to the plasma membrane requires the N-terminal EVH1 domain (Loureiro et al., 2002; Applewhite et al., 2007). Together, these results demonstrate that neither membrane targeting of the EVH1 domain or barbed end filament attachment of the EVH2 domain alone are sufficient for persistent plasma membrane localization of Ena/VASP proteins *in vivo*.

In eukaryotic cells, the localization of Ena/VASP proteins are regulated by at least two classes of proteins. The canonical Ena/VASP binding proteins contain D/E FPPPPXD peptide sequences (Niebuhr et al., 1997), which can bind to the hydrophobic groove on the N-terminal Ena/VASP homology 1 (EVH1) domain (Prehoda *et al.*, 1999). The acidic residues flanking the phenylalanine residues stabilize the interaction (Carl et al., 1999). Canonical Ena/VASP binding proteins include ActA (*Listeria*), the MRL (*Mig-10*, RIAM, Lamellipodin) protein family (Krause et al., 2004; Lafuente et al., 2004), PREL1 (Jenzora et al., 2005), Vinculin, Zyxin, Fyb/SLAP T-cell receptor signaling proteins (Krause et al., 2000), and the Robo/Sax-3 axon guidance factors (Bashaw et al., 2000). These proteins are expressed in a tissue specific manner and localize to either focal adhesions or the plasma membrane. A subclass of canonical Ena/VASP binding partners contain non-optimal LPPPPP motifs. These include several formin proteins (i.e. mDia2, FODH1) and the WAVE complex subunit, Abi2 (see Chapter 6, unpublished data). Although interactions between VASP and these proteins have been reported, the interaction are most likely transient and low affinity. The

non-canonical Ena/VASP binding partners, which lack the FPPPP peptide sequence(s), include integrins (Gupton et al., 2012), Tes (Broeda *et al.*, 2007), and the G-protein coupled receptor, CXCR2, in neutrophils (Neel *et al.*, 2009). Tes specifically binds to the EVH1 domain of MENA, but interacts with residues that are discrete from those which bind FPPPP peptides. Conversely, the cytoplasmic tail of CXCR2 interacts with the EVH2 domain of VASP by a mechanism that is hypothesized to phosphorylation dependent.

In fibroblasts, breast cancer cells, and hippocampal neurons Ena/VASP proteins colocalize with the plasma membrane associated protein, Lamellipodin (Krause *et al.*, 2005; Bae et al., 2010; Michael *et al.*, 2010). Similar to the *Listeria* protein, ActA, Lamellipodin contains six 'FPPPP' motifs which interact with the EVH1 domain of Ena/VASP proteins (Niebuhr et al., 1997; Krause et al., 2004). Lamellipodin contains a tandem Ras association and pleckstrin homology (RA-PH) domain, which is structurally homologous to the growth factor receptor-binding proteins Grb7, Grb10, and Grb14 (Depetris et al., 2009). Although a Ras GTPase binding partner has not been identified (Rodriguez-Viciano et al., 2004), Lamellipodin has been shown to interact with Rac1 GTPase in lysate in the nucleotide dependent manner (Quinn et al., 2008). In addition, the PH domain of Lamellipodin has been shown to binds specifically bind to PI(3,4)P₂ *in vitro* (Rodriguez-Viciano et al., 2004; Krause et al., 2004). Although published data suggests a role for Lamellipodin in regulating the localization of the Ena/VASP proteins to the plasma membrane, it is unknown whether Lamellipodin can modulate Ena/VASP function or autonomously regulates actin network assembly.

The MRL protein family has been implicated in regulating cell proliferation. The *Drosophila* MRL ortholog, *pico*, functions in epithelial cell proliferation through activation of the serum response factor (SRF) (Lyulcheva et al., 2009). Knockdown of *pico* results in a cell growth and proliferation defect. It is hypothesized that MRL proteins link global regulation of actin assembly to transcriptional regulation of cell proliferation. Supporting this hypothesis, Lamellipodin expression was recently correlated with SRF activity and the ability of cells to sense the ratio of monomeric and polymeric actin *in vivo* (Pinheiro et al., 2011). Disruption of this pathway during corticogenesis perturbs pyramidal cell migration in the cortex of the developing mouse brain. Similarly, mutations in the *C. elegans* Lamellipodin homolog, *mig-10*, results in the neuronal cell migration defect that epistatic to mutations in VASP (Manser et al., 1997; Forrester et al., 1997). How genetic interactions between Lamellipodin and the actin cytoskeleton translates to physical interactions, if any, remains unknown.

In this study we characterized the interactions between VASP and Lamellipodin *in vitro*, to test the hypothesis that a membrane tethered protein and the free actin filament barbed ends are required to reconstitute the dynamics of Ena/VASP function in actin based motility. Surprisingly, we found that Lamellipodin interacts directly with filamentous actin in the presence and absence of Ena/VASP proteins. *In vivo*, membrane tethered Lamellipodin localizes to the leading edge plasma membrane and appears to interact with dynamic actin filaments independent of its interaction with Ena/VASP proteins. By simultaneously interacting with Ena/VASP proteins and actin filaments,

Lamellipodin can increase the processivity of barbed end associated VASP tetramers *in vitro*. Together these results provide the first example of a membrane tethered actin binding protein that can modulate the barbed end processivity of Ena/VASP proteins.

Results

Membrane tethered Lamellipodin organizing actin filaments in vitro

Based on the *in vivo* requirements for Ena/VASP plasma membrane localization, we hypothesized that persistent plasma membrane localization requires a membrane tethering protein and free actin filament barbed ends. We characterized these requirements *in vitro* by reconstituting actin network assembly on lipid coated glass beads in the presence of Lamellipodin and VASP. Previously, the nucleation promoting factor, N-WASP, was shown to asymmetrically localize on lipid vesicles with actin comet tails *Xenopus* extract (Co et al., 2007). Similarly, the fluidity of the lipid bilayer on the glass microspheres allowed us to visualize and quantify actin dependent changes in the localization of proteins on the bead surface. First, we characterized the spatial distribution of the membrane tethered nucleation promotion factor, his₁₀Cherry-SCAR. In the absence of an actin network, his₁₀Cherry-SCAR was uniformly distributed across lipid coated bead surfaces (Supplemental Figure 1A). With the addition of monomeric actin, Arp2/3, and capping protein, actin comet tails rapidly assembled on the lipid coated beads in a his₁₀Cherry-SCAR dependent manner (Supplemental Figure 1B). Shortly after the actin network assembly was initiated, his₁₀Cherry-SCAR became asymmetrically distributed across bead surfaces with the highest concentration localized to the barbed end attachment zone (Supplemental Figure 1C-E).

To test whether Lamellipodin (Lpd) alters actin network assembly *in vitro* we generated actin comet tails on lipid coated beads with two different mixtures

of his₁₀ tagged proteins (Figure 1A). Both mixtures contained a 50% molar ratio of his₁₀Cherry-SCAR tethered to the bead surface. The second half of the membrane tethered proteins were either his₁₀GFP or his₁₀-GFP-Lpd^(850-1250aa). To directly compare how these membrane tethered proteins regulate actin network assembly we froze actin comet tail growth at different time points using a Latrunculin B/phalloidin cocktail (Akin and Mullins, 2008) and then measured the actin comet tail lengths. Surprisingly, when his₁₀-GFP-Lpd^(850-1250aa) was tethered to the bead surface actin comet tail grew much slower than bead coated with his₁₀GFP (Figure 1B). Visualization of membrane tethered his₁₀-GFP-Lpd^(850-1250aa) revealed that Lamellipodin, like SCAR, was predominantly localized to the barbed end attachment zone (Figure 1C). Conversely, his₁₀GFP was excluded from the barbed end attachment zone (Figure 1C). Localization of his₁₀-GFP-Lpd^(850-1250aa) to the barbed end attachment zone suggested that the C-terminus of Lamellipodin interacts with filamentous actin in the absence of Ena/VASP proteins. The differences in actin comet tail growth velocity were not simply caused by his₁₀-GFP-Lpd^(850-1250aa) reducing the density of the nucleation promoting factor. We find that lower densities of his₁₀Cherry-SCAR cause the actin network to grow faster (Supplemental Figure 1). Titrating the concentration of the membrane tethered proteins revealed that low densities of the Lpd (\leq 20% molar ratio) were capable of inhibiting actin network assembly.

Lamellipodin binds to filamentous actin in vitro

The C-terminal tail of Lamellipodin has an isoelectric point of 10.07. Although this domain shares no homology with known actin binding proteins, the high number of basic amino acid residues suggest that Lpd could interact with filamentous actin by electrostatic interactions (Supplemental Figure 2). The distribution of these residues is evolutionarily conserved among Lamellipodin homologs, but not RIAM or other FPPPP containing Ena/VASP interacting proteins (Supplemental Figure 2 and Supplemental Table 1). We tested whether the C-terminus of Lpd interacts directly with filamentous actin *in vitro* by visualizing the localization of monomeric GFP-Lpd^(850-1250aa) on single actin filaments using TIRF microscopy. In the presence of 50 mM KCl, GFP-Lpd^(850-1250aa) uniformly decorated single actin filaments with a measured dissociation rate constant of 255 ± 2 nM (Figure 2A-B). Supporting a mechanism of actin binding that is dependent of weak electrostatic interactions, Lpd weakly associated with actin filaments in the presence of 75-100 mM KCl (Figure 2C).

Since monomeric GFP-Lpd^(850-1250aa) has a weak affinity for filamentous actin *in vitro*, we hypothesized that oligomerization of GFP-Lpd^(850-1250aa) could enhance actin filament binding. The native oligomeric state of Lpd is unknown and neither are the protein interactions that could influence oligomerization. However, based on structural homology to the growth factor receptor-binding proteins (Grb protein family), the tandem Ras-associating (RA) and pleckstrin-homology (PH) domain of Lamellipodin is predicted to be a weak dimer in solution (Depetris et al., 2009); dimerization might be enhanced by membrane association and other protein interactions. In addition, Lpd has been shown to

localize to the tips of filopodia where it exists as a concentrated focus (Krause et al., 2004). To study how the oligomerization state affects actin filament binding of Lamellipodin, we characterized the binding interactions of dimeric and multivalent GFP-Lpd construct. To test whether dimerization of Lpd enhances actin filament binding *in vitro* we introduced a leucine zipper into the GFP-Lpd^(850-1250aa) protein. Compared to monomeric Lpd, dimeric protein GFP-LZ-Lpd bound to filamentous actin in the presence of 100 mM KCl (Figure 2F). We also purified larger Lpd oligomeric species (i.e. trimers/tetramers) by size exclusion chromatography and found that they had an enhanced actin filament binding activity (Figure 2D). When we visualized this subpopulation of clustered his₁₀-GFP-Lpd^(850-1250aa) at single molecule resolution, we could observe molecules bind and diffuse along the sides of actin filaments (Figure 2G). We observed a similar enhanced affinity for filamentous actin when we coupled his₁₀-GFP-Lpd^(850-1250aa) to 50 nm small containing unilamellar vesicles (SUVs) (Figure 2H). GFP-Lpd coated SUVs tightly bound to single actin filaments *in vitro*, suggesting that clustering of Lpd actin filament association.

Although Lpd showed no preference for ADP/ADP-Pi versus phalloidin stabilized actin filaments (Supplemental Figure 3A), we found that the interaction with filamentous actin was much weaker under during actin filament elongation. Systematic dissection of the TIRF assay buffer components also revealed that (1) MgCl₂ antagonizes Lpd binding, (2) ATP alone clusters and promotes actin filament binding, and (3) balanced Mg-ATP has a neutral effect (Supplemental Figure 3B). More importantly we found that Lpd actin filament binding by was

greatly reduced in the presence of nonpolymerizable monomeric actin (4 μ M actin, plus Latrunculin B). This effect occurred in the presence or absence of profilin (Supplemental Figure 3C). Inhibition of the filament binding was also independent of the oligomerization state of GFP-Lpd^(850-1250aa) (data not shown).

Lamellipodin can simultaneously bind Ena/VASP proteins and actin filaments

To characterize the complexity of interactions between Lamellipodin and VASP, we used sedimentation equilibrium ultracentrifugation to determine how many EVH1 domains can bind to the C-terminus of Lpd. For these experiments we monitored the sedimentation of GFP-Lpd^(850-1250aa), containing all six 'FPPPP' peptide sequences in the presence of excess monomeric VASP EVH1 domain (1-115 aa). We found that GFP-Lpd^(850-1250aa) sediments as a monomer with an apparent molecular weight of 60 kDa. In the presence of the VASP EVH1 domain we observed a dose dependent increase in the apparent molecular weight; binding saturated at 100 μ M VASP EVH1 and a ceiling molecular weight 200 kDa. This apparent molecular weight suggests that four EVH1 domains can bind to monomeric GFP-Lpd^(850-1250aa) in solution.

The C-terminus of Lamellipodin contains six 'FPPPP' motifs that interact with the N-terminal EVH1 domain of Ena/VASP proteins (Supplemental Figure 4A). Flanking each 'FPPPP' motifs are several positively charged amino acids that mediate electrostatic interactions with filamentous actin (Supplemental Figure 2). Although these domains do not appear to overlap, binding to

Ena/VASP proteins and filamentous actin could be mutually exclusive. In the presence of 500 nM Cy3-VASP EVH1 domain (1-114aa) or tetrameric VASP actin binding mutants, we detected no interaction between the VASP proteins and filamentous actin by TIRF microscopy (Figure 3A). However, with the addition of 500 nM GFP-Lpd^(850-1250aa), we observed recruitment of monomeric and tetrameric VASP EVH1 domains to the sides of actin filaments (Figure 3B). In the case of tetrameric Cy3-VASP^(RRRK-4A), the interaction with Lpd resulted in a high degree of protein clustering that was visible on the sides of actin filaments (Figure 3B). We have observed a similar clustering phenomenon when we combine Cy3-VASP and ActA^(255-392aa) (Figure 3C).

Lamellipodin C-terminal domain can localize to the barbed end attachment zone in vivo

In vivo, Lamellipodin localizes to actin based membrane protrusions in the absence of Ena/VASP proteins and free actin filament barbed ends (Krause et al., 2004). Based on our *in vitro* observations, Lamellipodin binds directly to actin filaments in the absence and presence of Ena/VASP proteins. To test whether membrane localization of Lpd requires dynamic actin filaments *in vivo*, we visualized the localization of GFP-Lpd^{1-1250aa} in XTC cells (Figure 4A). Lamellipodin localized to the leading off cells spread on poly-L-lysine. Single molecule expression of GFP-Lpd^{1-1250aa} revealed that protein bind and dissociate from the plasma membrane on a time scale of approximately 50-200 milliseconds (data not shown). We found that actin assembly and disassembly

was required for maintenance of Lpd leading edge localization (data not shown). When acutely treated cells with a drug cocktail that stops actin assembly and disassembly, we observed a rapid loss in membrane localization of GFP-Lpd^{1-1250aa} (data not shown). Consistent with Krause et al. (2004), only a fraction of membrane localized GFP-Lpd^{1-1250aa} was delocalized when cells were treated with low concentrations of Cytochalasin D to cap the barbed ends (data not shown).

Currently, the upstream binding partners of Lamellipodin are not well characterized and could therefore be responsible for loss of full length Lpd membrane localization following pharmacological inhibition of actin dynamics. To simplify our interpretation that membrane tethered Lpd binds directly to actin filaments at the leading edge, we tested whether the C-terminal domain of Lpd was sufficient for actin filament binding *in vivo*, as observed *in vitro*. For these experiments, we constitutively tethered GFP-Lpd^(850-1250aa) to the plasma membrane by fusing it to the Lyn₁₁ palmitoylation sequence derived from Src (Figure 4B). Similar to what has previously been observed for membrane tethered ActA-FPPPP-CAAX (Bear et al., 2000; Bear et al., 2002), Lyn-GFP-Lpd^(850-1250aa) localized to the leading edge of actin based membrane protrusions (Figure 4C). A second population of membrane tethered Lyn-GFP-Lpd^(850-1250aa) localized to focal adhesions (Figure 4C). Conversely, Lyn-GFP was uniformly distributed throughout the plasma membrane and did not localize to the barbed end attachment zone (Figure 4C).

The C-terminal domain of Lpd contains six FPPPP peptide sequences and can interact with four EVH1 domains as measured by analytical ultracentrifugation sedimentation equilibrium (Supplemental Figure 4B-D). To test whether leading edge localization Lyn-GFP-Lpd^(850-1250aa) was dependent on the interaction with Ena/VASP proteins, we mutated all six FPPPP motifs in the C-terminus of Lpd and expressed the protein as a Lyn-GFP fusion. *In vitro*, we found that mutating all the FPPPP motifs abolished the interaction with Ena/VASP proteins (Supplemental Figure 5A-B). However, plasma membrane localization of Lyn-GFP-Lpd^(850-1250aa) containing mutations in all six FPPPP motifs was indistinguishable from the localization of wild-type Lyn-GFP-Lpd^(850-1250aa) (Figure 4C). There was however a modest decrease in the amount of Lyn-GFP-Lpd^(850-1250aa) localized to focal adhesions (Figure 4C). Since localization of Lyn-GFP-Lpd^(850-1250aa) to the barbed end attachment zone was independent of the interaction with Ena/VASP proteins, we hypothesized that an interaction with the actin cytoskeleton was required. In contrast to Lpd, plasma membrane localization of ActA-FPPPP-CAAX requires the interaction with Ena/VASP proteins (Bear et al., 2000; Bear et al., 2002).

To test whether the leading edge localization of Lyn-GFP-Lpd^(850-1250aa) requires a dynamic actin cytoskeleton we used a cocktail of Jasplakinolide, Latrunculin B, and a Rock kinase inhibitor (Y27632) to freeze actin assembly and disassembly in cells (Peng et al., 2011). This drug cocktail stops actin assembly and disassembly within 30 seconds as judged by the immobilization of GFP-actin speckles in spread cells (unpublished data). When cells expressing wild type or

(AAPPP)_{x6} mutant Lyn-GFP-Lpd^(850-1250aa) were treated with this cocktail we observed rapid loss of leading edge localization within 10 seconds (Figure 4F-H). Since loss of Lyn-GFP-Lpd^(850-1250aa) localization at the barbed end attachment zone was Ena/VASP independent, this change in localization was due to a change in the actin network dynamics.

Lamellipodin enhances VASP barbed end processivity by a clustering independent mechanism

Ena/VASP proteins are weakly processive actin barbed end polymerases (Hansen and Mullins, 2010). Interactions with membrane tethering proteins could thought to regulate organelle localization, protein density, and activity of Ena/VASP proteins. Currently, profilin and actin, are the only proteins known to modulate Ena/VASP barbed end processivity. Since Lamellipodin can simultaneously interact with VASP and filamentous actin, we hypothesized that Lpd could modulate the processivity of Ena/VASP proteins by providing a lateral interaction to filamentous actin. To test our hypothesis, we imaged dynamic actin filament barbed end elongation in the presence of clustered his₁₀-GFP-Lpd^(850-1250aa) and Cy3-VASP. Under these conditions we discovered that both proteins, in complex, can track growing actin filament barbed ends (Figure 5A). The dwell time for the VASP-Lpd tip complex was significantly longer than single VASP tetramers.

Clustering Ena/VASP proteins on polystyrene beads can promote processive barbed end attachment and elongation of single actin filaments

(Breitspfecher et al., 2008). Since clustered his₁₀-GFP-Lpd^(850-1250aa) binds multiple Cy3-VASP tetramers *in vitro*, it is possible that the observed processivity enhancement was solely caused by protein oligomerization. To test this hypothesis, we measured the polymerase activity of a non-processive VASP mutant, FAB 2R-2A, in the presence of Lpd. We found that his₁₀-GFP-Lpd^(850-1250aa) rescued processivity of the VASP F-actin binding mutant and was indistinguishable from wild-type VASP (Figure 5B).

Since these experiments do not eliminate the contribution of Lpd dependent VASP oligomerization to the enhanced processivity, we measured the lifetime of clustered VASP tetramers in the absence of Lpd. For these experiments wild-type biotinylated-VASP was attached to streptavidin quantum dots (SA-Q). In the presence of 1-2 μ M monomeric actin and free barbed ends, we observed VASP coated Qdots processively tracking the growing ends of actin filaments (Figure 6A-B). Conversely, SA-Qdots coated with biotin-VASP^(3R-3A) were unable to processively track growing filament ends, supporting a hypothesis that Lpd rescued processivity of the VASP F-actin binding mutant by interaction with filamentous actin.

Discussion

There are several proposed mechanisms for how Ena/VASP barbed end processivity is regulated. These include (1) post-translational modifications of the EVH2 domain, (2) expression of different splice isoforms of the EVH2 domain, (3) profilin-actin isoforms specificity, and (4) clustering Ena/VASP tetramers. Post-translational modifications, such as phosphorylation, have been shown to change Ena/VASP protein affinity for filamentous actin (Barzik et al., 2005). Splicing and expression of different Ena/VASP isoforms has been shown to affect cancer cell metastasis by a mechanism that may be related to the activity of the VASP EVH2 domain (Philippar et al., 2009). Expression of different profilin-actin isoforms could limit or hyperactivate a particular Ena/VASP paralog in a tissue specific manner. *In vitro*, clustering has proven to be an effective mechanism for enhancing barbed end processivity by the formation of a collaborative Ena/VASP tip complex (Breitsprecher et al., 2008).

Currently there is no method for measuring barbed end processivity of Ena/VASP proteins *in vivo*. This makes it difficult to prove that the single molecule lifetimes measured for barbed end associated VASP tetramers *in vitro* represent how Ena/VASP proteins function in cells. However, the single molecule barbed end dwell times measured *in vitro* indicate that Ena/VASP proteins have shorter dwell times in solution relative to the turnover rates for plasma membrane associated Ena/VASP proteins. *In vivo*, full length tetrameric GFP-Ena/VASP proteins are been reported to have half-lives of recovery that range from 8.4-17.4 seconds as measured by FRAP (Applewhite et al., 2006; Vitriol et al., 2007; Lai

et al., 2008). The differences in lifetime measurements *in vivo* and *in vitro* suggest that additional protein interactions extend the lifetime of plasma membrane targeted Ena/VASP proteins and possibly modulate the barbed end processivity.

Although we have not been able to determine how Lamellipodin contributes to the overall lifetime of plasma membrane associated Ena/VASP proteins, the *in vitro* activity indicate that Lamellipodin would extend the lifetime of membrane targeted Ena/VASP protein. We find that Lamellipodin modulates VASP barbed end processivity by an unexpected mechanism involving the coordinated actin filament binding and Ena/VASP binding activities. Lamellipodin is not isolated example of an Ena/VASP membrane targeting proteins. It is plausible that non-FPPPP containing proteins contribute to the plasma membrane localization of Ena/VASP proteins. This model is supported by the observation showing that expression of FPPPP-cyto is not sufficient to antagonize Ena/VASP plasma membrane localization (Bear *et al.*, 2000). If Ena/VASP protein interact with the WAVE complex

In vitro, the F-actin binding domain of Ena/VASP proteins are required for actin filament side binding, barbed end capture, and processivity during barbed end filament elongation (Hansen and Mullins, 2010). Although Ena/VASP FAB mutants still localize to focal adhesions *in vivo*, mutants are not targeted to the leading edge plasma membrane (Loureiro *et al.*, 2002). In Ena/VASP null cells, MV^{D7}, the FAB mutant fails to localize to the leading edge membrane. Since the FAB domain is required for barbed end association, this suggests that plasma

membrane localization, more than focal adhesion targeting is dependent on actin filament barbed ends. Can Lamellipodin rescue the VASP FAB mutant phenotype *in vivo*, considering that Lamellipodin rescues barbed end processivity *in vitro*? Although this question is difficult to answer with the redundant mechanism regulating Ena/VASP plasma membrane localization, Lamellipodin could stabilize Ena/VASP barbed end association in specific contexts.

Although a Ras GTPase binding partner is yet to be identified, it has been shown that Rac1 can pull-down *Mig-10*/Lamellopodin in HEK293 lysate (Quinn et al., 2008). This interaction with Rac1 was GTP dependent and was not observed for the paralog, human RIAM (Quinn et al., 2008). Although unpublished, there is emerging evidence that VASP binds directly to Rac1 and the WAVE complex. Therefore, it is possible the interaction between Rac1 and Lamellipodin is indirect and mediated by Ena/VASP proteins. In *C. elegans*, *Mig-10*/Lamellipodin is epistatic to *ced-10*/Rac1 during synapse formation in the subset of neuroblast cells.

Based on *in vitro* characterization of Lamellipodin PH domain phospholipid interactions, localization of Lpd to the plasma membrane is PI(3,4)P₂ dependent (Krause et al., 2004). Implicated in regulating PI(3,4)P₂ production is the PI(3,4,5)P₃ phosphatase, SHIP-2 (Dyson et al., 2001). SHIP-2 localizes to the lamellipodia upon EGF treatment (Dyson et al., 2001). Amplification of the PI(3,4)P₂ signal could increase the concentration of Lamellipodin at the leading edge of polarized cells, thus providing a mechanism for spatial and temporal regulation of Lamellipodin plasma membrane localization.

Acknowledgements

We thank Peter Bieling for his 10-Cherry-SCAR protein and advice about glass surface chemistry; Matthias Krause (King's College, London) for the Lamellipodin plasmid; Roger Cooke and Kathy Franks-Skiba for heavy meromyosin (University of California at San Francisco); Dave Richmond (Fletcher Lab, University of California at Berkeley) for liposome preparation protocols; and members of the Mullins, Vale, and Weiner labs for reagents and feedback. Special thanks to Leslie Weaver, Stephanie Nowotarski, and Uri Manor for their help with the quantum dot experiment during the Woods Hole Physiology course (2010). This work was supported by grants from the National Institute of Health (R.D.M., ROI #GM61010) and the National Science Foundation (S.D.H.).

Materials and Methods

Molecular Biology

Lamellipodin clones were derived from a plasmid encoding human Lpd^{1-1251aa} (pBSII-SK(+)) vector) provided by Matthias Krause (King's College London). his₁₀-TEV-EGFP^(A207K)-Lpd^{850-1251aa} was cloned into a modified pETM-11 vector (EMBL Protein Expression and Purification Facility; Heidelberg, Germany). All GFP/Cherry cell expression vectors were cloned into the pDeltaCMV-EGFP vector (Clontech) provided by Naoki Watanabe (Tohoku University, Japan) and Orion Weiner (University of California at San Francisco, CVRI Department). All of our constructs contained a monomeric EGFP variant with an A207K point mutation. We added a Lyn palmytolation sequence (GCIKSKGKDSA) derived from Src (Inone et al., 2005) to the pDeltaCMV-EGFP^(A207K) to generate the Lyn-GFP expression construct. Lyn-GFP-Lpd^(850-1251aa) (AAPPP)_{x6} mutations were introduced using Pfu Turbo DNA polymerase and standard site-directed mutagenesis techniques. We made the constitutive GFP-Lpd dimer by inserting a leucine zipper derived from *S. cerevisiae*, Gcn4 (KQLEDKVEELASKNYHLENEVARLKKLV) between the GFP and Lpd protein sequences (Tomishige et al., 2002). The isoelectric points for Lamellipodin homologs was calculated with EXPASY ProtParam (Gasteiger et al., 2005).

Protein Expression and purification

BL21 Star pRARE bacteria (kanamycin and chloramphenicol resistant) were induced to express his₁₀-TEV-EGFP^{A207K}-Lpd^{850-1250aa} by the addition of

0.25 mM IPTG at OD600 = 0.75. Bacteria were then shifted from 37°C to 25°C and allowed to express for 6 hours before harvesting. Cells were lysed using microfluidizer in the presence of 50 mM Na₂PO₄ [pH 8], 300 mM NaCl, 0.5 mM BME, 50 µg/mL benzamidine, 1 mM PMSF (added 2-3x), and DNase. Spin in Ti45 for 30 minutes, 20000 rpm. High speed supernatant was then pump over a 5mL Hi-Trap Cobalt charged column, washed [50 mM Na₂PO₄ [pH 8.0], 300 mM NaCl, 10 mM imidazole 0.5 mM BME], and the eluted [50 mM Na₂PO₄ [pH 8.0], 300 mM NaCl, 500 mM imidazole 0.5 mM BME]. When appropriate, we used TEV protease to cleave the his₁₀ tag. Eluate was then dialyzed overnight into 10 mM HEPES [pH 7.5], 200 mM NaCl, 5 mM BME. After 20-24 hrs, dialysate was flowed back over Ni-NTA resin to remove uncleaved protein before applying to a 323mL Superdex200 gel filtration column equilibrated with 10 mM HEPES [pH 7.5], 200 mM NaCl, 1 mM TCEP. Peak fractions were then combined 1:1 with 10 mM HEPES [pH 7.5], 1 mM TCEP and applied to a MonoS cationic exchange column equilibrated with 10 mM HEPES [pH 7.5], 100 mM NaCl, 1 mM TCEP. Bound EGFP-Lpd^{850-1250aa} was then eluted using a 100-300 mM NaCl salt gradient over 35 CV (1 CV = 1 mL) at a flow rate of 1 mL/min. his₁₀-EGFP-Lpd^{850-1250aa} elutes at ~220 mM NaCl; EGFP^{A207K}-Lpd^{850-1250aa} elutes at ~170 mM NaCl. After the MonoS column, peak fractions of his₁₀-EGFP-Lpd, but not EGFP-Lpd contained a small fraction of oligomers. Freezing in glycerol, sucrose, arginine-glutamate, or without cryo-protection also caused his₁₀-EGFP-Lpd protein to oligomerize. Consequently, we gel filtered small aliquots of his₁₀-EGFP-Lpd with a Superdex200 column equilibrated with 10 mM HEPES [pH 7.5],

200 mM NaCl, and 1 mM TCEP before bead motility and TIRF microscopy experiments. Gel filtered his₁₀-EGFP-Lpd showed no signs to proteolysis or aggregation for at least a week on ice.

Cytoplasmic actin was purified from *Acanthamoeba castellanii* as described by Gordon et al. (1976) and Zuchero (2009). Actin was stored at 4⁰C in 2 mM Tris [pH 8.0], 0.5 mM TCEP, 0.1 mM CaCl₂, 0.2 mM ATP, 0.01% azide, and used within 6 months. Monomeric actin was labeled on Cys-374 with with 3-7 molar excess Alexa488-maleimide (Invitrogen), Cy3-maleimide (GE Healthcare), or Cy5-maleimide (GE Healthcare) on ice in the absence of reducing agent for 5-15 minutes. The reaction was quenched with 10 mM DTT and then centrifuged at 346716 x *g* (TLA 100.4 rotor, Beckman Coulter) to remove insoluble/aggregated protein and dye. Labeled actin was then polymerized at room temperature by the addition of KMEI polymerization buffer (final concentration of 10 mM imidazole [pH 7.0], 50 mM KCl, 1 mM MgCl₂, 1 mM EGTA). Polymerized actin was then pelleted, washed, and then resuspended in G-buffer (2 mM Tris [pH 8.0], 0.5 mM TCEP, 0.1 mM CaCl₂, 0.2 mM ATP, 0.01% azide) to depolymerize. Following dialysis in G-buffer for 3-5 days, actin was hard spun, and then gel filtered (Superdex 75). We typical observed a 50-60% labeling efficiency.

Ena/VASP proteins were expressed and purified as previously described by Hansen and Mullins (2010). The Arp2/3 complex, capping protein, and profilin were purified and handled as previously described by Akin and Mullins (2008).

Analytical ultracentrifugation

For sedimentation equilibrium experiments, GFP-Lpd^{850-1250aa} and VASP^{1-114aa} (monomeric EVH1 domain) were diluted into 20 mM HEPES [pH 7], 100 mM KCl, 1 mM TCEP and then centrifuged at 346716 x *g* (TLA 100.4 rotor, Beckman Coulter) for 20 minutes to remove potentially aggregated protein. GFP-Lpd^{850-1250aa} was then combined with 0-100 μ M VASP^{1-114aa}, loaded into a 6-well Teflon chambers with quartz window and placed in an AN-60 rotor. Samples were centrifuged at 7000, 10000, and 14000 rpm in a Beckman XL-I centrifuge for 14-18 hours per speed or until equilibrium was reached. Continuous scans were acquired every 2 hours at 488 nm to monitor the sedimentation of GFP-Lpd^{850-1250aa}. Extinction coefficient of 55,000 M⁻¹ cm⁻¹ was used to calculate the protein concentration from the absorbance at 488 nm. Global fitting of three equilibrium traces from all speeds (i.e. 7, 10, 14K rpm) for each condition was performed using NIH Sedphit and Sedphat software (Peter Schuck, NIH).

Pegylation of coverslips

Glass was functionalized as described by Bieling et al. (2010) with some modifications. In brief, coverglass (Corning No. 1.5, 18x18 mm sq.) was cleaned by sonication in 3M NaOH, followed by Piranha etching (40% hydrogen peroxide, 60% sulfuric acid). Coverslip sandwich were then incubated with undiluted 3-glycidyloxypropyl-trimetoxy silane (GOPTS, Sigma 440167) for 30 minutes at 75^oC. Glass was then washed with anhydrous acetone (Electron Microscopy Sciences; RT 10016) to remove excess silane and rapidly dried with an in house

manufactured coverslip spin drier. Next, hydroxyl-PEG_{3000 Da}-NH₂ (95%) and CH₃O-Biotin-PEG_{3000 Da}-NH₂ (5%) powders (Cat # 10-3000-20 and 10-3000-25-20 respectively; Rapp Polymere) and dissolved in anhydrous acetone. Silanized coverslips were assembled into sandwiches with 75 μ L of dissolved amino-PEG/amino-PEG-biotin used per coverslip sandwich. The pegylation reaction was performed at 75⁰C in glass weigh jars (Fisher, Cat# 03-420-5C) for \geq 2 hours. Glass was then washed with copious amounts of MilliQ water before spin drying and storing at room temperature in a dust free container.

Single actin filament TIRF assay

Counterglass slides placed in coplin jars were bath sonicated in 3M NaOH. Glass was rinsed with water, bath sonicated in 100% ethanol, and then dried. To minimize protein depletion in the TIRF experiments, the counterglass was coated with poly-L-lysine-PEG (PLL-PEG), which was dried onto the glass surface before rinsing with water. Synthesis of PLL-PEG was performed as previously described by Huang et al. (2001) and Bieling et al. (2010). PEG/biotin-PEG functionalized coverslips were then attached to PLL-PEG coated counterglass with double sided tape (Tesa). To reduce nonspecific binding to the PEG functionalized surface the imaging chamber was washed with a 1x PBS solution pH 7.2 containing 1% Pluronic F-127 and 100 μ g/mL kappa casein. Glass was then washed with buffer containing 20 mM HEPES pH 7, 1 mM DTT, 200 mM KCl, 100 μ g/mL beta-casein (wash buffer). Glass was subsequently incubated for 1 minute with 50 nM streptavidin, followed by 50nM biotin-PEG₁₁

heavy meromyosin diluted in wash buffer.

The single actin filament TIRF assay was performed as described by Hansen and Mullins (2010). Phalloidin stabilized actin filaments were generated by copolymerizing 2 μM actin (20% Cy3 or Cy5 labeled) with 1 μM dark phalloidin at room temperature for 2-3 hours in 10 mM imidazole [pH 7], 50 mM KCl, 1 mM EGTA, and 1 mM MgCl_2 containing buffer. In brief, actin polymerization reactions were initiated by combining 1 μL of 10x ME (10mM EGTA, 10mM MgCl_2) with 9 μL of 4.44 μM monomeric actin (5-10% Cy3 or Cy5 labeled). Actin was then combined with 2x TIRF imaging buffer and 4x protein (i.e. VASP, profilin, Lpd) to create a final buffer composition of 20 mM HEPES [pH 7], 50-100 mM KCl, 1.5 mM MgCl_2 , 1 mM EGTA, 0.2 % methylcellulose cP400, 1 mg/mL BSA, 1 mM ATP, 20 mM BME, 20 mM glucose, 125 $\mu\text{g}/\text{mL}$ glucose oxidase, and 20 $\mu\text{g}/\text{mL}$ catalase. A final reaction volume of 40 μL was wicked through a PEG/biotin-PEG glass flow cell and imaged at 23-25 $^\circ\text{C}$.

For experiments involving streptavidin quantum dots (655 nm emission), biotinylated proteins were combined in 10-40 molar excess to the SA-Q655 concentration. Biotinylated proteins and quantum dots were diluted in buffer containing 20 mM HEPES [pH 7], 100 mM KCl, 1 mg/mL BSA, and 1 mM DTT. We added 1 μM free biotin to the TIRF buffer to quench free streptavidin on the Qdots, which dramatically reduced the amount of non specific binding to the PEG/biotin-PEG glass surfaces. A final concentration of 0.125-0.25 nM Qdots were typically used in the actin polymerization, barbed end tracking experiments.

Preparation of liposomes

The following lipids were used to make liposomes: 18:1 (Δ^9 -Cis) PC (DOPC) 1,2-dioleoyl-*sn*-glycero-3-phosphocholine (Avanti #850375C) and 18:1 DGS-NTA(Ni) [1,2-dioleoyl-*sn*-glycero-3-[(N-(5-amino-1-carboxypentyl)iminodiacetic acid)succinyl] (nickel salt) (Avanti #790404C). All lipids were combined in clean glass vials (National Scientific Glass tubes with PTFE screw cap lid; Fisher 03-391-7B) under a continuous stream of Argon gas. The total amount of lipids used for each liposome prep was 4 μ moles. Lipid mixtures in chloroform were dried to a film under Argon gas, followed by ≥ 2 hours of drying in a vacuum desiccator. Dry lipid films were then hydrated with phosphate buffer saline to concentration of 4 mM and freeze-thawed 10-times using liquid nitrogen and a water bath at ambient temperature. Small unilamellar vesicles were generated by micro-tip sonication (4 x 15 seconds pulses, 20% amplitude) and then microcentrifuged at 4⁰C for 30 minutes at 21130 x *g*. The supernatant was then transferred to a new eppendorf stored on ice and used within 5 days.

Lipid coated glass microspheres

Glass microspheres were acid-washed by diluting a 10% (wt/vol) bead slurry of 2.34 μ m silica beads (Bangs Laboratories, Cat # SS05N) 1/10 in a glass vial containing concentrate nitric acid (Fisher). Glass bead were incubate in nitric acid overnight at room temperature. Acid-washed glass beads were pelleted by centrifugation for 5 minutes and then washed with MilliQ water. This process was

repeated four times. Beads were resuspended in water to 10% (wt/vol) bead slurry.

Lipid bilayers were assembled on acid-washed glass beads by combining 20 μL of 10% bead slurry (vortex/sonicate before aliquoting) with 105 μL 20 mM HEPES [pH 7], 150 mM NaCl (or PBS [pH 7.2]) in an eppendorf. Diluted glass beads were vortexed and then bath sonicated for 5 minutes. Monodisperse glass beads were then combined with 25 μL of 4 mM SUVs (50-100 nm diameter), vortexed briefly, and then rotated at room temperature for 15-30 minutes. After assembling the lipid bilayer, 750 μL of milliQ water was added to each tube and beads were micro-centrifuged for 2 minutes at 200 x *g*. The supernatant was aspirated off the beads and the 750 μL water wash, followed by micro-centrifuged was repeated four times. After the final spin, the supernatant was aspirated leaving ~ 50 μL of water/beads. Beads were then resuspended by vortexing and 150 μL of buffer containing, 20 mM HEPES [pH 7], 200 mM KCl was added. The final bead slurry was ~ 1 % (wt/vol) and contained a total KCl concentration is ~ 150 mM.

To charge lipid coated glass beads with protein, we combined 5 μL of 1 % bead slurry with 45 μL of 111 nM his₁₀ tagged protein (i.e. his₁₀Cherry-SCAR). Proteins were diluted into buffer containing 20 mM HEPES [pH 7], 150 mM KCl, 100 $\mu\text{g}/\text{mL}$ BSA, 0.5 mM TCEP. Before all experiments, we determined the quality of lipid bilayer by charging beads with a mixture of 50 nM his₁₀GFP and 50 nM his₁₀Cherry-SCAR. If the beads are uniformly coated with GFP and Cherry, you can assume the beads have a membrane. However, if you observed

bright cherry fluorescent patches on glass beads that do not colocalize with GFP, incomplete bilayers formed. We found that his₁₀Cherry-SCAR, but not his₁₀GFP binds to naked glass under these conditions.

Actin bead motility assay

The reconstituted actin bead motility mix is based on Akin and Mullins (2008) and Co *et al.*, (2007). Our assay contained 20 mM HEPES pH 7, 100 mM KCl, 1 mM MgCl₂, 1 mM EGTA, 1 mM ATP, 0.2% methylcellulose (cP 400), 2.5 mg/mL BSA, 15 mM TCEP-HCl, 50 mM KOH (to neutralize TCEP-HCl), 7.5 μM cytoplasmic actin (*A. castellani*), 50-125 nM mouse capping protein (recombinant), 100-150 nM Arp2/3 (native, *A. castellani*), 3-5 μM human profilin I (recombinant), 3-5 μM human cofilin (recombinant), and ~0.1% (wt/vol) 2.3 μm lipid coated glass beads charged with 100 nM his₁₀-Cherry-SCAR^{APVCA} for 15-30 minutes. After reactants, samples were with quench or immediately flowed in to glass coverslip chamber, which was then sealed with VALAP (vasoline, lanolin, paraffin; 1:1:1). Quenching actin assembly and disassembly was achieved by combine equal volumes of reaction and 37.5 μM LatB-phalloidin that was diluted into 20 mM HEPES [pH 7], 100 mM KCl, 100 μg/mL BSA, 0.5 mM TCEP. Imaging chamber for the bead motility assay were assembled with glass silanized with a 2% solution of diethyldichlorosilane (Gelest) in isopropanol (pH 4.5 with acetic acid) (Akin and Mullins, 2008).

Tissue Culture and Live cell imaging

XTC *Xenopus* fibroblasts were maintained at 25⁰C (without CO₂) in 70% diluted Leibovitz L-15 media (Invitrogen/GIBCO) containing 10% heat inactivated fetal bovine serum (Gibco) and penicillin/streptomycin (Watanabe and Mitchinson, 2004). Cells that were 70% confluent in 24-well plastic dishes containing complete media were transiently transfected with 500 ng of plasmid DNA and 1.5 μL Lipofectamine LTX with 1 μL PLUS reagent (Invitrogen). After 5 hours of transfection, media was exchanged. Prior to live cell imaging, XTC cells were trypsinized and plated in 70% L-15 media lacking phenol red and FBS. XTC cells were plated onto a glass bottom 96-well plate (Matrical Bioscience, MGB096-1-2-LG) which cleaned with 3M NaOH for 1 hour and subsequently coated with 0.01% poly-L-lysine (Sigma, P-8920) for 20-30 minutes at 23-25⁰C. Cells were imaged on a Nikon TIRF microscope at 23-25⁰C.

For experiments in which we froze actin assembly and disassembly with the JLY cocktail, cells were allowed to spread on poly-L-lysine coated glass for 30 minutes in the presence of 10μM Rock kinase inhibitor (Y27632). Cells were then treated with 10 μM Jasplakinolide (CalBiochem, 420107), 8 μM Latrunculin B (Enzo Life Science, T110-0001), and 10 μM Y27632 Rock kinase inhibitor (CalBiochem, 688001) to freeze actin dynamics (Peng et al., 2011). All drugs were diluted with 70% L-15 media lacking serum and penicillin/streptomycin.

Microscopy and image processing

All images were collected on an inverted Nikon Eclipse TIRF microscope using a 100x oil objective with a 1.49 NA (Nikon) at 23-25⁰C. We employed the Nikon Perfect Focus instrument to maintain the focal plan throughout each experiment. GFP/Alexa488, Cy3, and Cy5 fluorophore were excited with 491 nm, 561 nm, and 638 nm laser light respectively. Laser power was modulated by neutral density filters, an AOTF, and exposure settings such that 1-2 mW of laser power was delivered to the sample. We used a single filter cube containing a multipass excitation and dichroic filter (Chroma). A Sutter Instruments filter wheel containing the appropriate emission filters was placed in front of the camera. Images were collected on a cooled Andor Xion EM-CCD camera. The microscope, camera, and lasers were controlled using Micromanager 1.4 (Stuurman et al., 2007). Image processing and data analysis was performed with ImageJ. Figures for the manuscript were made with Adobe Illustrator and Photoshop CS3.

References

- Akin, O. and R.D. Mullins. 2008. Capping protein increases the rate of actin-based motility by promoting filament nucleation by the Arp2/3 complex. *Cell*. 133, 841-851.
- Applewhite, D.A., M. Barzik, S. Kojima, T.M. Svitkina, F.B. Gertler, and G.G. Borisy. 2007. Ena/VASP proteins have an anti-capping independent function in filopodia formation. *Mol. Biol. Cell*. 18, 2579-2591.
- Barzik, M., T.I. Kotova, H.N. Higgs, L. Hazelwood, D. Hanein, F.B. Gertler, and D.A. Schafer. 2005. Ena/VASP proteins enhance actin polymerization in the presence of barbed end capping proteins. *J. Biol. Chem*. 280, 28653-28662.
- Bae, Y.H., Z. Ding, T. Das, A. Wells, F.B. Gertler, and P. Roy. 2010. Profilin I regulates PI(3,4)P₂ and lamellipodin accumulation at the leading edge thus influencing motility of MDA-MB-231 cells. *PNAS*. 107(50): 21547-21552.
- Bear, J.E., T.M. Svitkina, M. Krause, D.A. Schafer, J.J. Loureiro, G.A. Strasser, I.V. Maly, O.Y. Chaga, J.A. Cooper, and G.G. Borisy. 2002. Antagonism between Ena/VASP proteins and actin filament capping regulates fibroblast motility. *Cell*. 109, 509-521.
- Bear, J.E. and F.B. Gertler. 2009. Ena/VASP: towards resolving a pointed controversy at the barbed end. *J. Cell Sci*. 122, 1947-1953.
- Bieling, P., Telley, I.A., Hentrich, C., Piehler, J., and T. Surrey. (2010). Fluorescence Microscopy Assays on Chemically Functionalized Surfaces for Quantitative Imaging of Microtubule, Motor, and +TIP Dynamics. *Methods in Cell Biology*. v.95.
- Boeda, B., D.C. Briggs, T. Higgins, B.K. Garvalov, A.J. Fadden, N.Q. McDonald, and M. Way. 2007. Tes, a specific Mena interacting partner, breaks the rules for EVH1 binding. *Mol. Cell*. 28, 1071-1082.
- Breitsprecher, D., A.K. Kieseewetter, J. Linkner, C. Urbanke, G.P. Resch, J.V. Small, and J. Faix. 2008. Clustering of VASP actively drives processive, WH2 domain mediated actin filament elongation. *EMBO J*. 27, 2943-2954.
- Carl, U.D., M. Polimann, E. Orr, F.B. Gertler, T. Chakraborty, and J. Wehland. 1999. Aromatic and basic residues within the EVH1 domain of VASP specify its interaction with proline-rich ligands. *Current Biology*. 9(13): 715-718.
- Co, C., D.T. Wong, S. Gierke, V. Chang, and J. Taunton. 2007. Mechanism of actin network attachment to moving membranes: barbed end capture by N-WASP WH2 domains. *Cell*. 128, 901-913.

- Depetris, R.S., J. Wu, and S.R. Hubbard. 2009. Structural and functional studies of the Ras-associating and pleckstrin-homology domains of Grb10 and Grb14. *Nature Structure Molecular Biology*. 16(8): 833-840.
- Dyson, J.M., C.J. O'Malley, J. Becanovic, A.D. Munday, M.C. Berndt, I.D. Coghill, H.H. Nandurkar, L.M. Ooms, and C.A. Mitchell. 2001. The SH2-containing inositol polyphosphate 5-phosphatase, SHIP-2, binds filamin and regulates submembraneous actin. *Journal of Cell Biology*. 155(6): 1065-1079.
- Forrester, W.C., and G. Garriga. 1997. Genes necessary for *C. elegans* cell and growth cone migrations. *Development*. 124, 1831-1843.
- Gasteiger E., C. Hoogland, A. Gattiker, S. Duvaud, M.R. Wilkins, R.D. Appel, and A. Bairoch. 2005. *Protein Identification and Analysis Tools on the ExPASy Server*; (In) John M. Walker (ed): The Proteomics Protocols Handbook, Humana Press. pp. 571-607.
- Gordon, D.J., E. Eisenberg, and E.D. Korn. 1976. Characterization of cytoplasmic actin isolated from *Acanthamoeba castellanii* by a new method. *J. Biol. Chem*. 251, 4778-4786.
- Gupton, S.L., D. Riquelme, S.K. Hughes-Alford, J. Tadros, S.S. Rudina, R. O Hynes, D. Lauffenburger, and F.B. Gertler. 2012. Mena binds $\alpha 5$ integrin directly and modulates $\alpha 5\beta 1$ function. *Journal for Cell Biology*. 198(4): 657-676.
- Hansen, S.D. and Mullins, R.D. (2010). VASP is a processive actin polymerase that requires monomeric actin for barbed end association. *Journal of Cell Biology*. 191(3):571-84.
- Hermanson, G.T. 1996. Bioconjugate Techniques. San Diego: Academic Press (pp. 266-272). (Product # 20002T).
- Huang, N.-P., R. Michel, J. Voros, M. Textor, R. Hofer, A. Rossi, D.L. Elbert, J.A. Hubbell, and N.D. Spencer. 2000. Poly(l-lysine)-g-poly(ethylene glycol) Layers on Metal Oxide Surfaces: Surface Analytical Characterization and Resistance to Serum and Fibrinogen Adsorption. *Langmuir*. 17:489-498.
- Inoue, T., W.D. Heo, J.S. Grimley, T.J. Wandless, and T. Meyer. 2005. An inducible translocation strategy to rapidly activate and inhibit small GTPase signaling pathways. *Nature Methods*. 2, 415-418.
- Jenzora, A., B. Behrendt, J.V. Small, J. Wehland, and T.E. Stradal. 2005. PREL1 provides a link from Ras signalling to the actin cytoskeleton via Ena/VASP proteins. *FEBS Letters*. 579: 455-463.

- Krause, M., A.S. Sechi, M. Konradt, D. Monner, F.B. Gertler, and J. Wehland. 2000. Fyn-binding protein (Fyb)/SLP-76-associated protein (SLAP), Ena/Vasodilator-stimulated phosphoprotein (VASP) proteins and the Arp2/3 complex link T cell receptor (Tcr) signaling to the actin cytoskeleton. *Journal of Cell Biology*. 149(1): 181-194.
- Krause, M., J.D. Leslie, M. Stewart, E.M. Lafuente, F. Valderrama, R. Jagannathan, G.A. Strasser, D.A. Rubinson, H. Liu, and M. Way. 2004. Lamellipodin, an Ena/VASP ligand, is implicated in the regulation of lamellipodial dynamics. *Dev. Cell*. 7, 571-583.
- Lacayo, C.I., Z. Pincus, M.M. VanDuijn, C.A. Wilson, D.A. Fletcher, F.B. Gertler, A. Mogilner, and J.A. Theriot. 2007. Emergence of large-scale cell morphology and movement from local actin filament growth dynamics. *PLoS Biol*. 5,e233.
- Lafuente, E.M., A.A. van Puijenbroek, M. Krause, C.V. Carman, G.J. Freeman, A. Berezovskaya, E. Constantine, T.A. Springer, F.B. Gertler, and V.A. Boussiotis. 2004. RIAM, an Ena/VASP and Profilin ligand, interacts with Rap1-GTP and mediates Rap1-induced adhesion. *Developmental Cell*. 7: 585-595.
- Lai, F.P., M. Szczodrak, J. Block, J. Faix, D. Breitsprecher, H.G. Mannherz, T.E. Stradal, G.A. Dunn, J.V. Small, and K. Rottner. 2008. Arp2/3 complex interactions and actin network turnover in lamellipodia. *EMBO*. 27: 982-992.
- Loureiro, J.J., D.A. Rubinson, J.E. Bear, G.A. Baltus, A.V. Kwiatkowski, and F.B. Gertler. 2002. Critical roles of phosphorylation and actin binding motifs, but not the central proline-rich region, for Ena/Vasodilator-stimulated phosphoprotein (VASP) function during cell migration. *Mol. Bio. Cell*. 13: 2533-2546.
- Lylcheva, E., E. Taylor, M. Michael, A. Vehlow, S. Tan, A. Fletcher, M. Krause, and D. Bennett. 2009. Drosophila pico and its mammalian ortholog lamellipodin activate serum response factor and promote cell proliferation. *Developmental Cell*. 15, 680-690.
- Manser, J., C. Roonprapunt, and B. Margolis. 1997. *C. elegans* cell migration gene *mig-10* shares similarities with a family of SH2 domain proteins and acts cell nonautonomously in excretory canal development. *Developmental Biology*. 184, 150-164.
- Michael, M., A. Vehlow, C. Navarro, and M. Krause. 2010. c-Abl, Lamellipodin, and Ena/VASP proteins cooperate in dorsal ruffling of fibroblasts and axonal morphogenesis. *Current Biology*. 20, 783-791.
- Neel, N.F., M. Barzik, D. Raman, T. Sobolik-Delmaire, J. Sai, A.J. Ham, R.L. Mernaugh, F.B. Gertler, and A. Richmond. 2009. VASP is a CXCR2-interacting protein that regulates CXCR2-mediated polarization and chemotaxis. *J. Cell Sci.*

122. 1882-1894.

Niebuhr, K., F. Ebel, R. Frank, M. Reinhard, E. Domann, U.D. Carl, U. Walter, F.B. Gertler, . Wehland, and T. Chakraborty. 1997. A novel proline-rich motif present in ActA of *Listeria monocytogenes* and cytoskeletal proteins is the ligand for the EVH1 domain, a protein module present in the Ena/VASP family. *The EMBO Journal*. 16(17): 5433-5444.

Pinheiro., E.M., Z. Xie, A.L. Norovich, M. Vidaki, L. Tsai, and F.B. Gertler. 2011. Lpd depletion reveals that SRF specifies radial versus tangential migration of pyramidal neurons. *Nature Cell Biology*. 13(8): 989-995.

Prehoda. K.E., D.J. Lee, and W.A. Lim. 1999. Structure of the Enabled/VASP Homology 1 Domain–Peptide Complex: A Key Component in the Spatial Control of Actin Assembly. *Cell*. 97, 471-480.

Quinn, C.C., D.S. Pfeil, and W.G. Wadsworth. 2008. CED-10/Rac1 mediates axon guidance by regulating the asymmetric distribution of MIG-10/lamellipodin. *Current Biology*. 18, 808-813.

Rasnik, I., S.A. McKinney, and T. Ha. 2006. Nonblinking and long-lasting single-molecule fluorescence imaging. *Nature Methods*. 3(11), 891-893.

Rodriguez-Viciano, P., C. Sabatier, and F. McCormick. 2004. Signaling specificity by Ras family GTPases is determined by the full spectrum of effectors they regulate. *Molecular Biology of the Cell*. 24(11): 4943-4954.

Stuurman, N., N. Amodaj, and R.D. Vale. 2007. μ Manager: Open Source software for light microscope imaging. *Microscopy Today* 15: 42-43.

Tomishige, M., D.R. Klopfenstein, and R.D. Vale. 2002. Conversion of Unc104/KIF1A Kinesin into a Processive Motor After Dimerization. *Science*. 297.

Vitriol, E.A., A.C. Uetrecht, F. Shen, K. Jacobson, and J.E. Bear. 2007. Enhanced EGFP-chromophore-assisted laser inactivation using deficient cells rescued with functional EGFP-fusion proteins. *PNAS*. 104(16): 6702-6707.

Watanabe, N., and T.J. Mitchison. 2004. Single-molecule speckle analysis of actin filament turnover in lamellipodia. *Science*. 295, 1083-1086.

Peng, G.E., S.R. Wilson, and O.D. Weiner. 2011. A pharmacological cocktail for arresting actin dynamics in living cells. *Molecular Biology of the Cell*. 22(21): 3986-3994.

Zuchero, JS. 2009. In vitro actin assembly assays and purification from *Acanthamoeba*. *Methods in Molecular Biology*, vol. 370. Adhesion Protein Protocols, 2nd edition.

Figures Legends

Figure 1

Lamellipodin localizes to the barbed end attachment zone in the absence of VASP

(a). Cartoon diagram of lipid coated glass bead with tethered his₁₀-Cherry-

SCAR^{APVCA}, his₁₀-GFP-Lpd^{850-1250aa}, or his₁₀-GFP attached via that Ni⁽⁺²⁾ lipid.

(b). Representative actin comet tails grown in the presence of 7.5 μM actin (5% Alexa488), 50 nM Arp2/3, 100 nM capping protein and 6 μM hPro1. Lipid coated glass beads (2.3 μm) were charged with 50 nM his₁₀-Cherry-SCAR^{APVCA}, plus 50 nM his₁₀-GFP-Lpd^{850-1250aa} or 50 nM his₁₀-GFP (50% Cherry, 50% GFP). Actin comet tails assembly and disassembly was stopped at the indicated time points by combining the bead motility assay, 1:1, with 37.5 μM LatB-phalloidin. Scale bar is 5 μm.

(c). Spatial distribution of his₁₀-Cherry-SCAR^{APVCA} and his₁₀-GFP during steady state actin tail growth and recycling (30 minute time point). his₁₀-Cherry-SCAR^{APVCA} concentrates on the barbed end dense side of the actin comet tail. his₁₀-GFP is excluded from the zone of concentrated his₁₀-Cherry-SCAR^{APVCA}. Line scans of his₁₀-Cherry-SCAR^{APVCA} and his₁₀-GFP across the lipid coated bead are shown to the right. Scale bar is 5 μm.

(d). Spatial distribution of his₁₀-Cherry-SCAR^{APVCA} and his₁₀-GFP-Lpd^{850-1250aa} during steady state actin tail growth and recycling (30 minute time point). his₁₀-Cherry-SCAR^{APVCA} and his₁₀-GFP-Lpd^{850-1250aa} concentrate on the barbed end dense side of the actin comet tail. iLine scans of his₁₀-Cherry-SCAR^{APVCA} and

his₁₀-GFP-Lpd^{850-1250aa} across the lipid coated bead are shown to the right.

Scale bar is 5 μm.

Figure 2

Lamellipodin is an actin binding protein

(a). GFP-Lpd^{850-1250aa} binds to filamentous actin *in vitro*. Images of GFP-Lpd^{850-1250aa}, 125-500 nM, bound to the sides phalloidin stabilized actin filaments (not shown). Scale bar is 5 μm.

(b). Determination of K_d for GFP-Lpd^{850-1250aa} binding to filamentous actin using GFP fluorescence intensity on bound protein.

(c). Actin filament binding of 500 nM monomeric GFP-Lpd^{850-1250aa} is the presence of 50, 75, or 100 mM KCl. Scale bar is 10 μm.

(d). Purification of GFP-Lpd^{850-1250aa} (monomer), GFP-LZ-Lpd^{850-1250aa} (dimer), and his₁₀-GFP-Lpd^{850-1250aa} (trimer/tetramer) by size exclusion chromatography (24 mL Superdex200 column).

(e). Cartoon showing the different oligomerization states of Lpd purified.

(f). Compared to monomeric GFP-Lpd^{850-1250aa}, GFP-LZ-Lpd^{850-1250aa} (dimers) and his₁₀-GFP-Lpd^{850-1250aa} (oligomers) bind to filamentous actin in the presence of 100 mM KCl.

(g). Kymograph of his₁₀-GFP-Lpd^{850-1250aa} oligomers diffusing along the length of a phalloidin stabilized actin filament. Vertical scale bar is 5 seconds.

(h). Membrane clustered his₁₀-GFP-Lpd^{850-1250aa} binds to filamentous actin. Localization of 50 nm vesicles coated with his₁₀-GFP-Lpd^{850-1250aa} bound to Alexa568 phalloidin stabilized actin filaments. Scale bar is 5 μm.

Figure 3

Lamellipodin can simultaneously bind to filamentous actin and EVH1

(a). VASP EVH1 domains does not interact with filamentous actin *in vitro*. Localization of 200 nM (monomeric concentration) of Cy3-VASP^{1-114aa} (EVH1 domain), Cy3-VASP^{LIL-3A, 3R-3A}, and Cy3-VASP^{RRRK-4E} on phalloidin stabilized actin filaments (20% Cy5 labeled). Buffer contains 20 mM HEPES [pH 7], 50 mM KCl, 1 mg/mL BSA, 1 mM TCEP. Scale bar is 10 μm.

(b). GFP-Lpd^{850-1250aa} can simultaneously interact with filamentous actin and VASP EVH1 domains. Colocalization of 500 nM monomeric GFP-Lpd^{850-1250aa} phalloidin stabilized actin filaments (20% Cy5 labeled) in the presence of 200 nM (monomeric concentration) of Cy3-VASP^{1-114aa} (EVH1 domain), Cy3-VASP^{LIL-3A, 3R-3A}, or Cy3-VASP^{RRRK-4E}. Scale bar is 10 μm.

Figure 4

Lamellipodin C-terminal domain binds to filamentous actin *in vivo*

(a). Localization of mCherry-Lpd^{1-1250aa} at the plasma membrane and focal adhesions in XTC cells. Scale bar is 10 μm.

(b). Localization of GFP-Lpd^{1-1250aa} at the plasma membrane in XTC cells.

Maximum intensity projection of cell expressing single molecule protein levels.

Scale bar is 10 μ m.

(c). Cartoon of palmitoylated Lyn-GFP and Lyn-GFP-Lpd constructs tethered to the plasma membrane.

(d). Constitutively membrane tethered Lyn-GFP-Lpd^{850-1250aa} localizes to the leading edge. Localization of Lyn-GFP-Lpd^{850-1250aa} does not require an interaction with Ena/VASP. Lyn-GFP is uniformly localized on the plasma membrane and does not concentrate at the leading edge. Scale is 10 μ m.

(e). Barbed ends are not required for plasma membrane localization of Lyn-GFP-Lpd^{850-1250aa} or Lyn-GFP-Lpd^{850-1250aa} (AAPPP)_{x6}. Representative localization patterns for cells before and after the addition of 200 nM Cytochalasin D for 10 minutes. Reorganization of the actin network slightly changes the localization of the Lyn-GFP-Lpd proteins. Scale bar is 10 μ m.

(f). Image montage showing rapid loss of Lyn-GFP-Lpd^{850-1250aa} (AAPPP)_{x6} following the addition of actin freeze cocktail JLY (8 μ M Jasplakinolide, 10 μ M Latrunculin B, and 10 μ M Y27632). Scale bar is 5 μ m.

(g). Dynamic actin assembly is required for maintenance of Lyn-GFP-Lpd^{850-1250aa} and Lyn-GFP-Lpd^{850-1250aa} (AAPPP)_{x6} localization at the leading edge.

Kymograph showing loss of Lyn-GFP-Lpd^{850-1250aa} or Lyn-GFP-Lpd^{850-1250aa} (AAPPP)_{x6} leading edge localization following the addition of the JLY cocktail.

Leading edge localization disappears after the addition of JLY. Horizontal scale bar is 2 μ m. Vertical scale bar is 1 minute.

(h). Kymograph showing translocation of membrane tethered Lyn-GFP-Lpd^{850-1250aa} into the cell body, indicative of incomplete myosin inhibition. Horizontal scale bar is 5 μ m. Vertical scale bar is 2 minute.

Figure 5

Lamellipodin enhances VASP barbed end processivity by a clustering independent mechanism

(a). his₁₀-GFP-Lpd^{850-1250aa} increases the barbed end association lifetime of Cy3-VASP. 2 μ M actin (20% Cy5 labeled) was polymerized in the presence of 5 nM Cy3-VASP and 50 nM his₁₀-GFP-Lpd^{850-1250aa}.

(b). his₁₀-GFP-Lpd^{850-1250aa} can rescue processivity of the non-processive filamentous actin binding mutant, Cy3-VASP^{RRR-AAA}.

Figure 6

ActA and Lamellipodin enhance VASP processivity by distinct mechanisms

(a). Biotinylated VASP linked to a streptavidin quantum dot 565nm (SA-Q565) can processively track single actin filament barbed ends. Montage of a single actin filament (30% Alexa488 actin)

(b). Kymographs showing processive Biotin-VASP coupled to SA-Q655 tracking the barbed end in the presence of 2 μ M actin (20% Cy5 labeled actin).

(c). Biotin-VASP^{RRR-AAA} clustered on a SA-Q655 is non-processive in the presence of 2 μ M actin (20% Cy5 labeled actin).

(d). ActA²⁵⁵⁻³⁹²-Biotin coupled to a SA-Q655 recruits Alexa488-VASP to support processive barbed end filament elongation in the presence of 2 μ M actin (20% Cy5 labeled actin).

(e-f). Cartoon Biotin-SNAP-Lpd⁸⁵⁰⁻¹²⁵⁰ bound to SA-Q655 recruits Alexa488-VASP. How processive are these complexes?

Figure 7

Model for Lamellipodin mediated Ena/VASP barbed end processivity

Lamellipodin is recruited to actin based membrane protrusions through interaction with PI(3,4)P₂ and possibly Ras/Rac GTPases. Like the Grb protein family, membrane associated Lamellipodin forms a homo-dimer on the plasma membrane through the interaction between the tandem RA-PH domain.

Oligomerized Lamellipodin can interact with filamentous actin in the absence of Ena/VASP proteins. Ena/VASP protein that associate with free actin filament barbed ends can simultaneously bind to the actin filament binding protein, Lamellipodin. By this mechanism, the lifetime membrane targeted and barbed end associated Ena/VASP proteins are extended.

Supplemental Figure 1

Actin based motility on lipid coated glass beads

(a). Localization of 100 nM his₁₀-Cherry-SCAR^{APVCA} on 2.3 μ m lipid coated glass beads (4% Ni-NTA, 96% DOPC). Scale bar is 10 μ m.

- (b). Montage of actin comet tails frozen at different times point. Actin networks were assembled in the presence of 7.5 μ M actin (5% Alexa488), 50 nM Arp2/3, 100 nM capping protein, 6 μ M hPro1, 3 μ M cofilin. Scale bar is 10 μ m.
- (c). Image of actin comet tails at steady-state in the presence of cofilin dependent network recycling described in (b). Scale bar is 10 μ m.
- (d). Images of asymmetric his₁₀-Cherry-SCAR^{APVCA} localization in the presence of actin comet tail. Scale bar is 5 μ m.
- (e). Line scan across lipid coated bead surface in (d) showing fluorescent intensity of asymmetric his₁₀-Cherry-SCAR^{APVCA}.

Supplemental Figure 2

Sequence of the Lamellipodin actin binding domain

- (a). Protein sequence alignment of the C-terminal protein sequences of human Lamellipodin and homologs. Basic amino acid residue (arginine and lysine) are highlight in blue. Gray boxes mark the location of the EVH1 FPPPP binding domains.
- (b). Cartoon diagram showing that the EVH1 binding domain do not overlap with basic amino acid residues implicated in binding filamentous actin.

Supplemental Figure 3

Parameters that regulate Lamellipodin actin filament binding *in vitro*

- (a). GFP-Lpd^{850-1250aa} binds equally well to ADP/ADP-Pi versus phalloidin stabilized actin filaments.

- (b). Unbalanced Mg-ATP concentrations affects Lpd actin filament binding.
- (c). Monomeric actin and profilin-actin antagonizes Lamellipodin actin filament binding.

Supplemental Figure 4

Sedimentation equilibrium to determine stoichiometry of VASP-Lpd interaction

- (a). Cartoon showing domain organization of human Lamellipodin (1-1250aa).
- (b). Analytical ultracentrifugation sedimentation equilibrium traces for VASP EVH1 binding to GFP-Lpd^{850-1250aa}.
- (c). Table showing the predicted and observed molecular weight of the VASP EVH1 domain binding to GFP-Lpd^{850-1250aa}.
- (d). Cartoon showing the binding of EVH1 domains to the C-terminal tail of Lpd. We hypothesize that steric hinderance allows only a single EVH1 domain to interact with the tandem FPPPP motifs (red triangles).

Supplemental Figure 5

Lamellipodin interaction with Ena/VASP protein requires FPPPP motif and EVH1 domain

- (a-b). Wild-type and mutant protein sequences of Lamellipodin (850-1250aa).
- (c-d). Lamellipodin FPPPP peptide sequences are required to recruit Ena/VASP proteins to the lipid coated glass beads. Lpd mutant containing mutations in all

six FPPPP motifs does not bind to VASP. his₁₀-GFP-Lpd^{850-1250aa} (AAPPP)_{x6} fails to recruit Cy3-VASP^{1-380aa} to the lipid coated bead.

(e). VASP interaction with Lpd is EVH1 domain dependent. Recruitment of Cy3-VASP^{1-380aa}, but not Cy3-VASP^{115-380aa} to lipid coated glass beads charged with his₁₀-GFP-Lpd^{850-1250aa}.

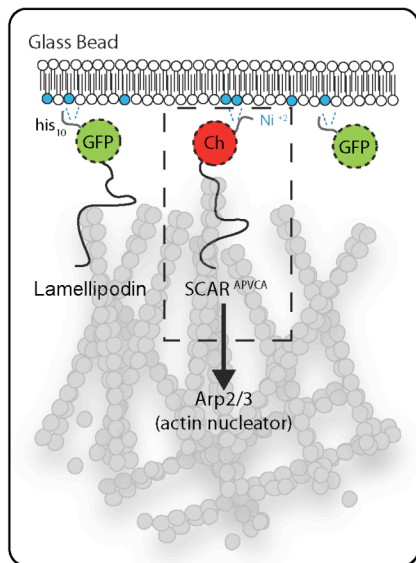
Supplemental Table 1

Defining the actin binding domain of Lamellipodin

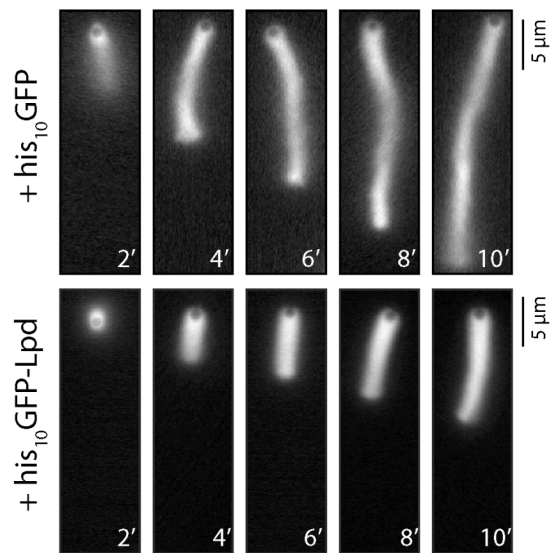
(a). Comparison of Lpd, RIAM, and ActA isoelectric points, number of FPPPP peptide sequences, and total number of basic amino acid residues.

Figure 1

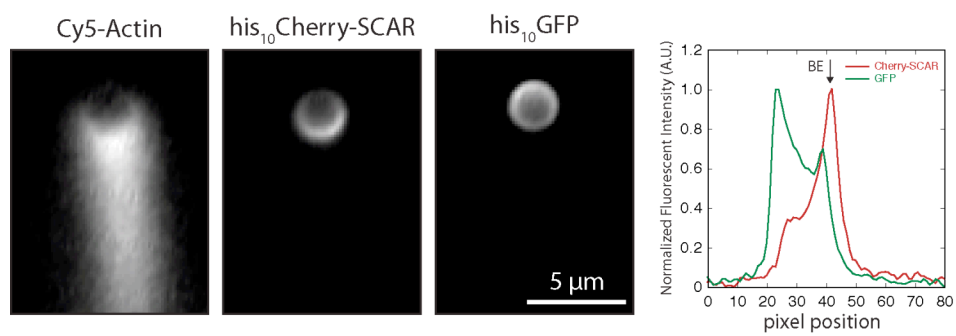
A.



B.



C.



D.

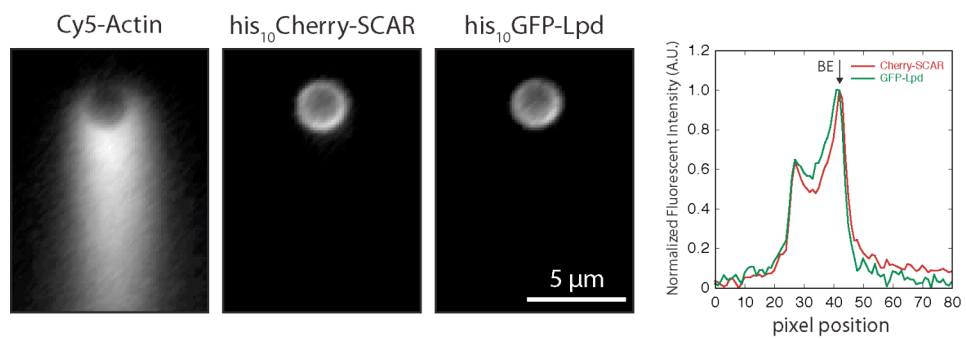


Figure 2

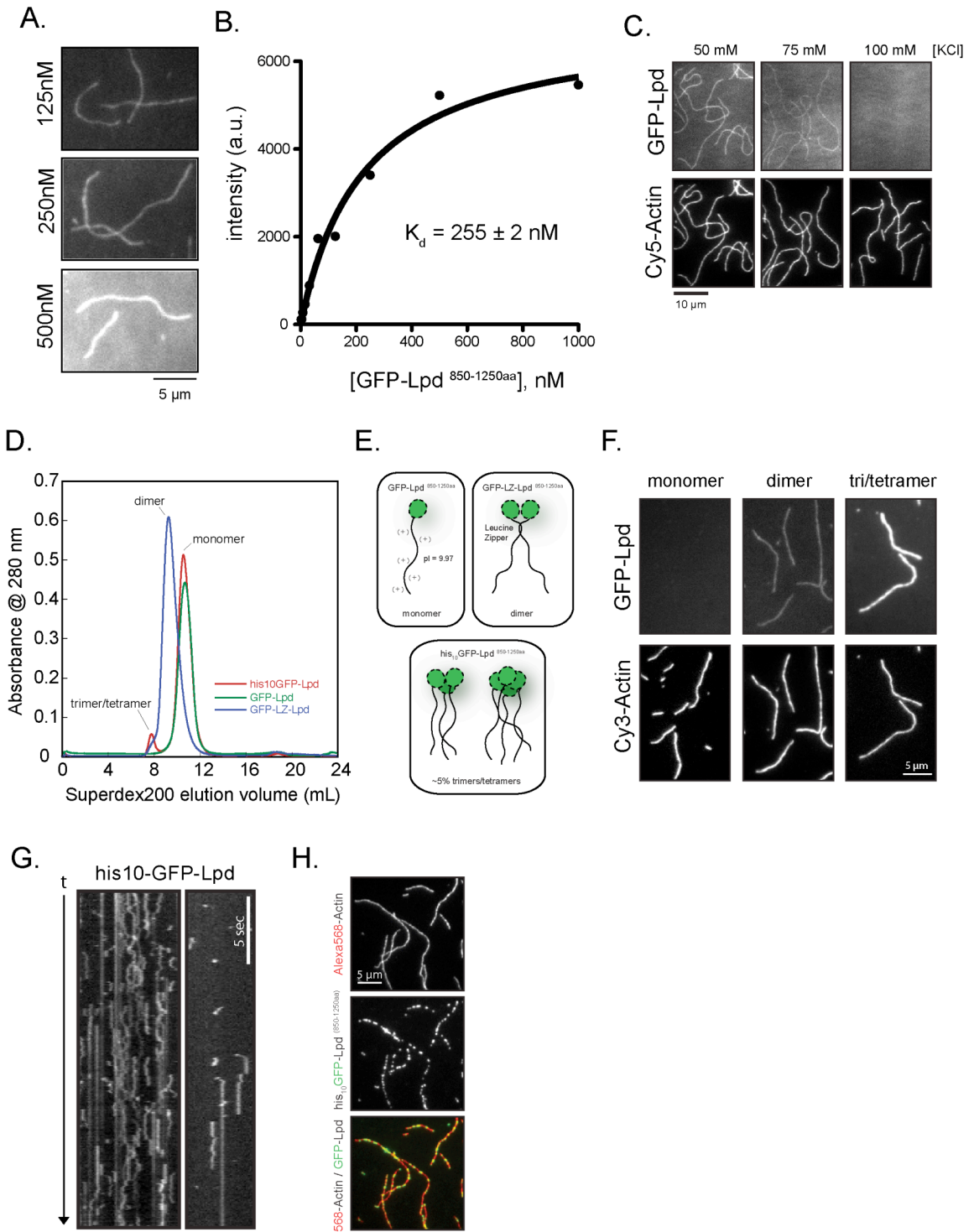
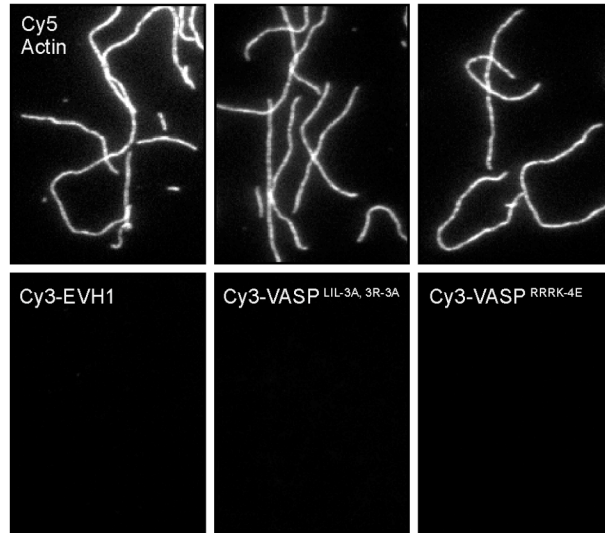


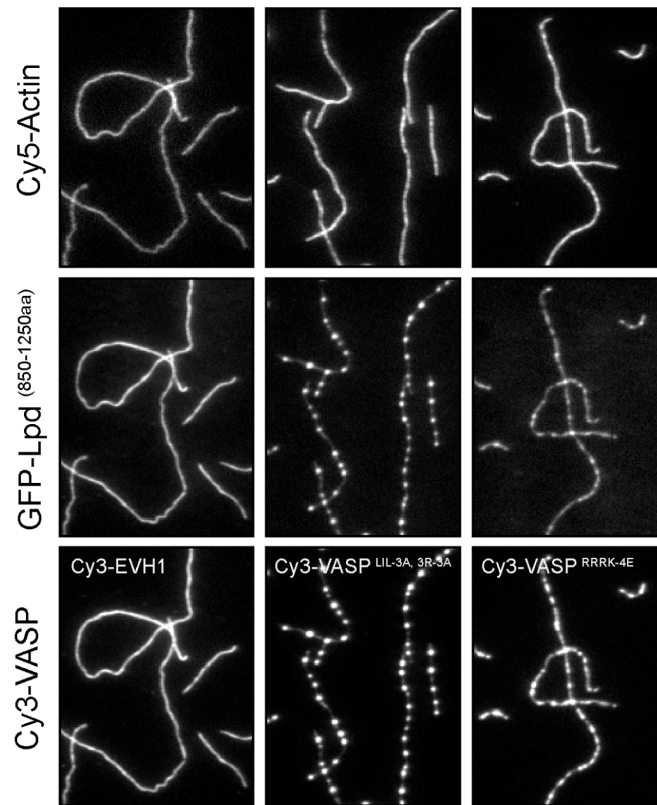
Figure 3

A.



10 μm

B.



10 μm

Figure 4

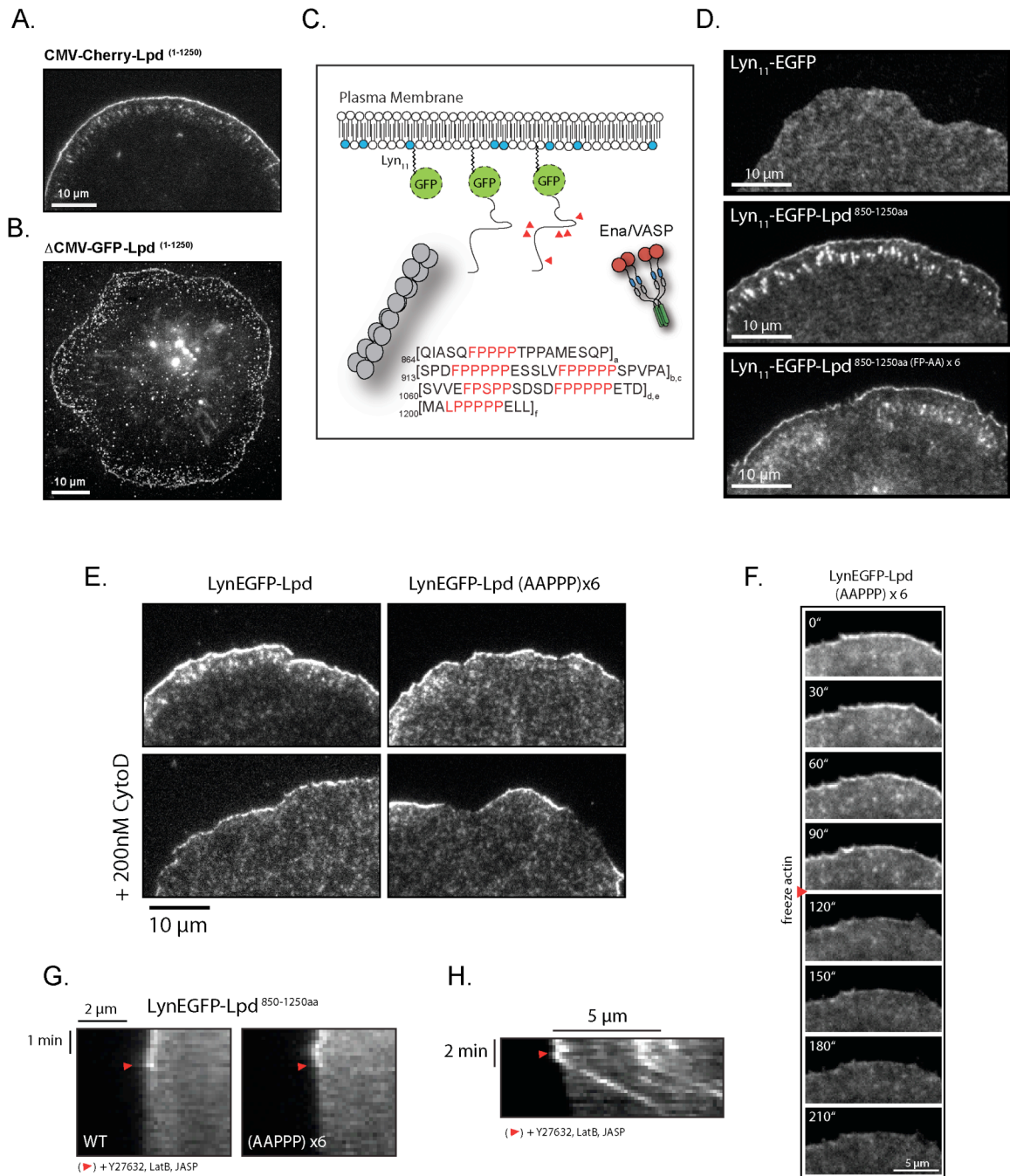


Figure 5

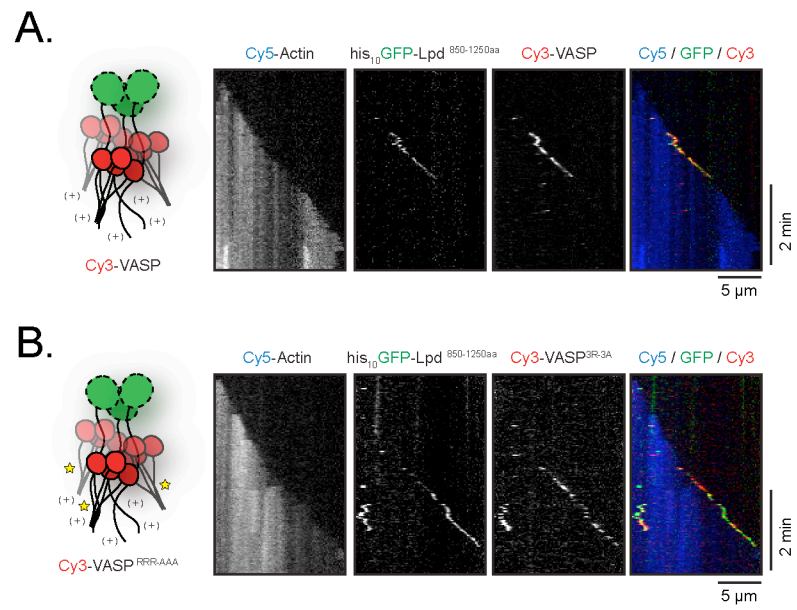


Figure 6

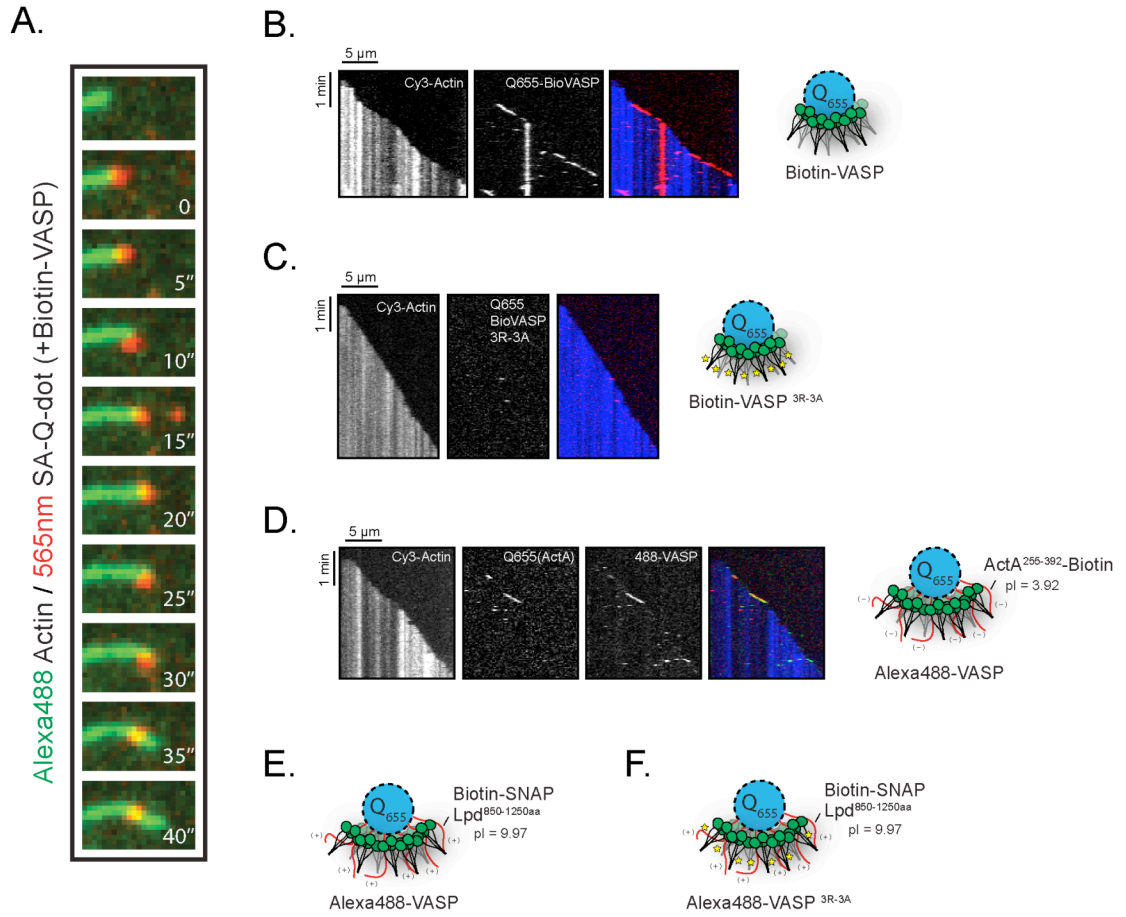
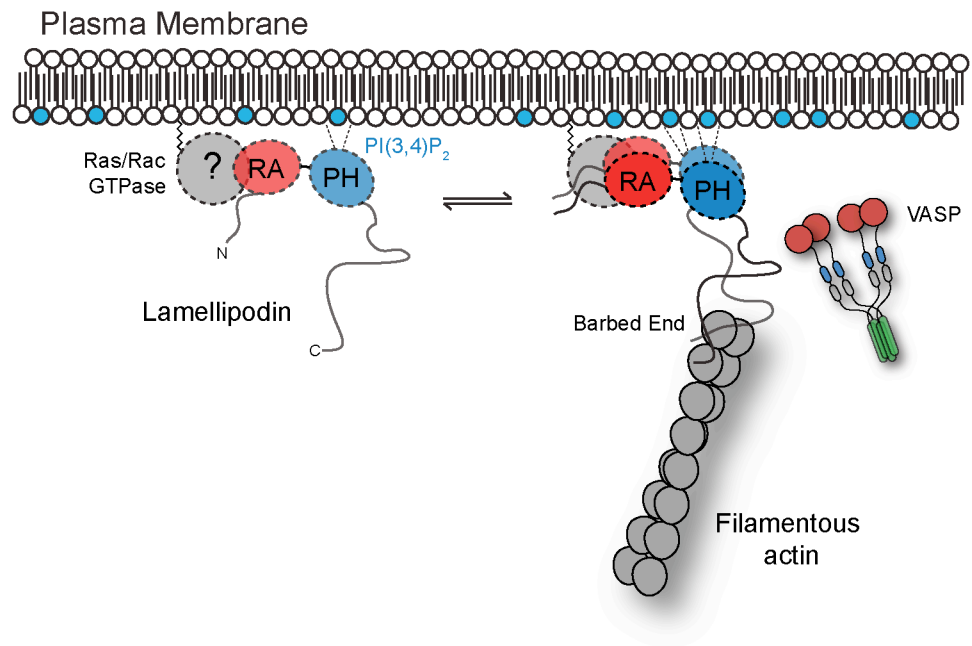
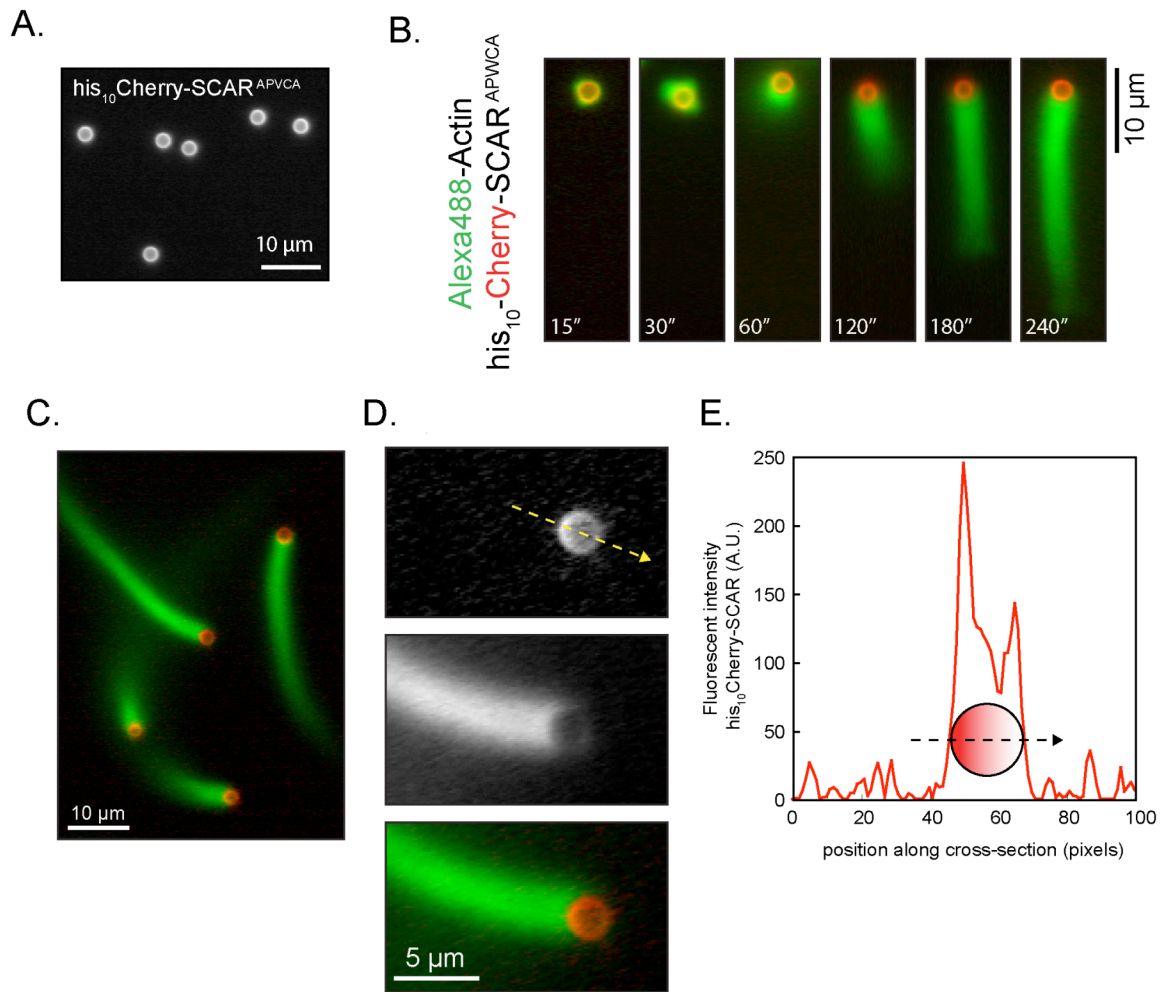


Figure 7

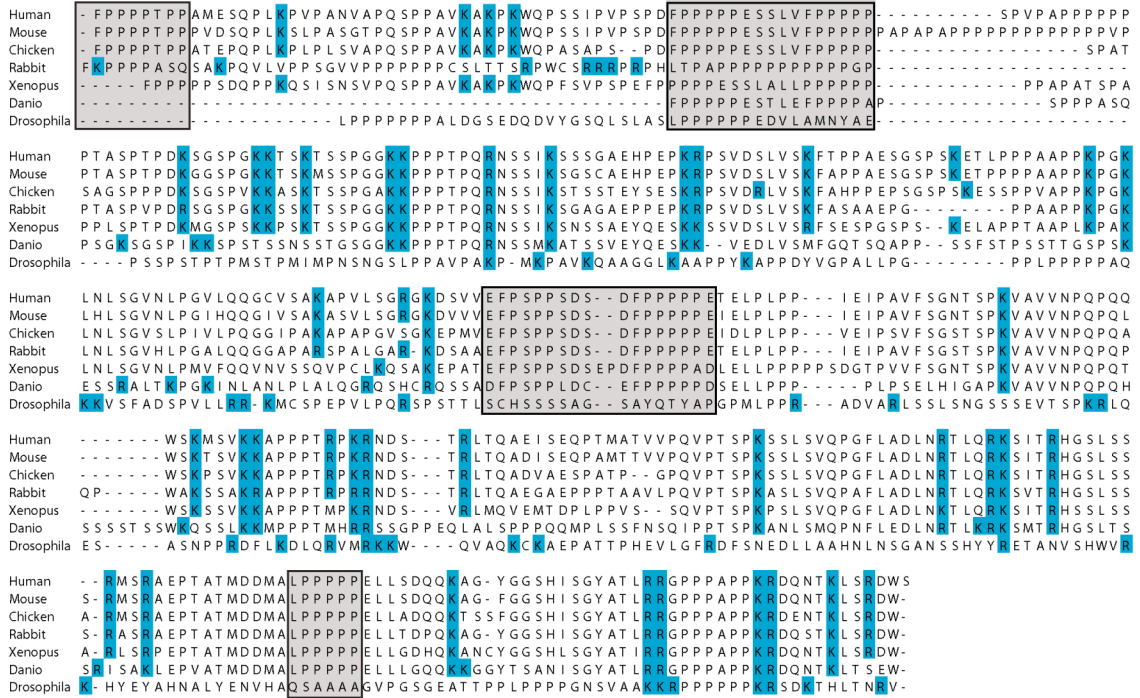


Supplemental Figure 1

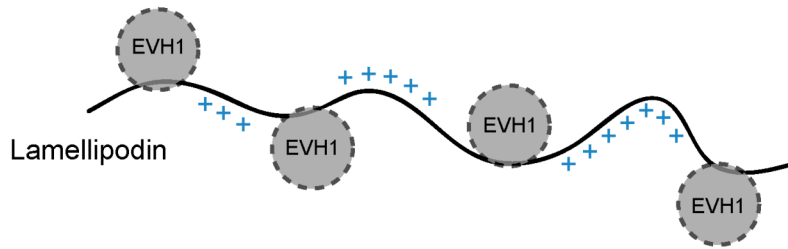


Supplemental Figure 2

A.

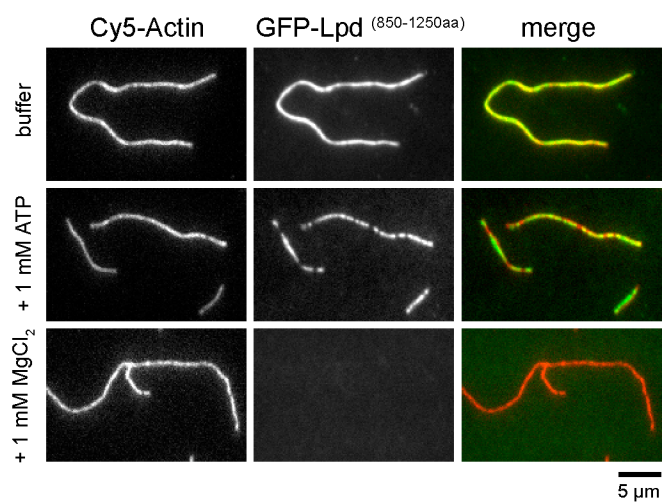


B.



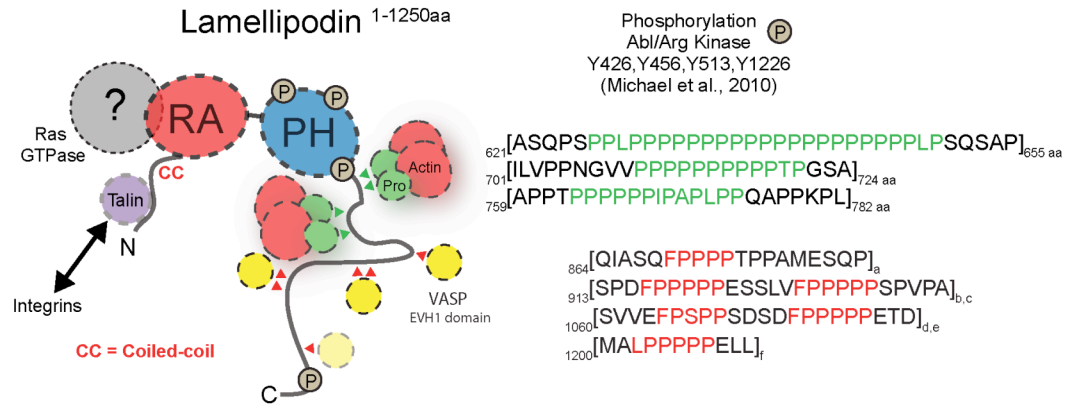
Supplemental Figure 3

A.



Supplemental Figure 4

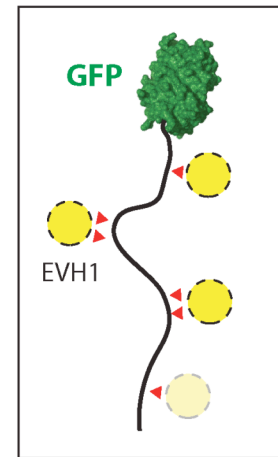
A.



B.

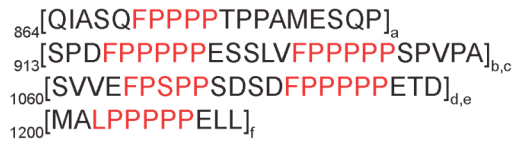
	predicted MW (kDa)	observed MW (kDa)	[EVH1] excess	# EVH1 bound
GFP-Lpd ^{850-1250aa}	69.2	67.1	0	0
+ 25 μ M VASP (EVH1)	--	79.4	2.5	1.0
+ 50 μ M VASP (EVH1)	--	94.4	5.0	2.2
+ 75 μ M VASP (EVH1)	--	104	7.5	2.9
+ 100 μ M VASP (EVH1)	--	110	10	3.4

C.

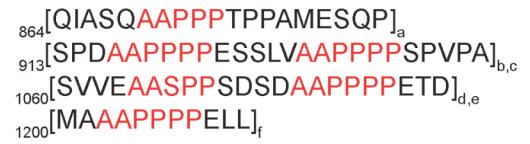


Supplemental Figure 5

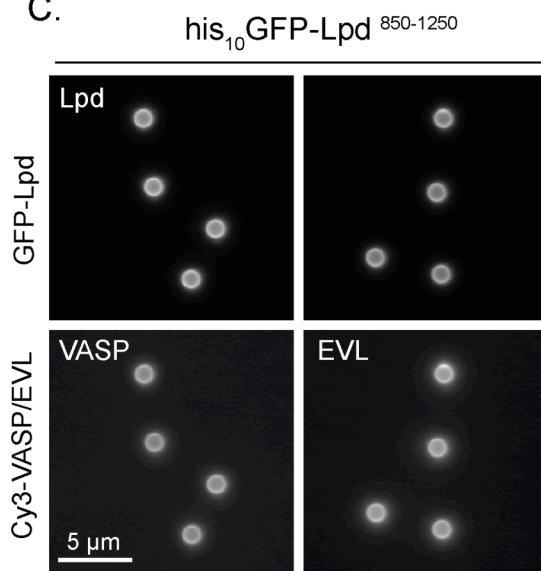
A.



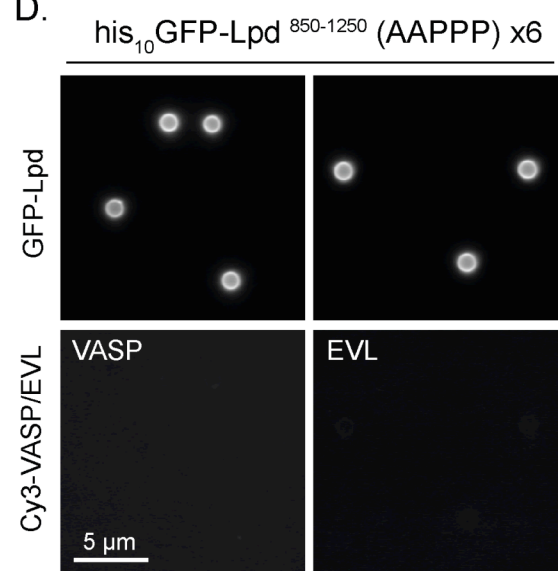
B.



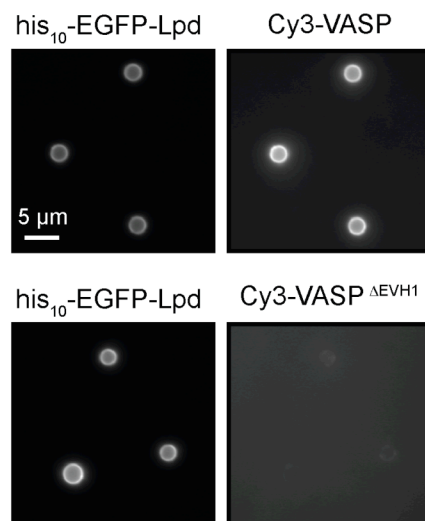
C.



D.



E.



Supplemental Table 1

organism	protein	FL (aa)	FL pI	VASP BD FPPPP	VBD pI	# FPPPP	# residues Arg/Lys^a	% Homology to human Lpd
Human	Lamellipodin/RAPH1	1-1251	8.97	850-1251	9.97	6	44	100
Mouse	Lamellipodin/RAPH1	1-1266	9.08	855-1266	10.00	6	44	91
Rabbit	Lamellipodin/RAPH1	1-1049	8.92	747-1049	10.27	4	38	89
Chicken	Lamellipodin/RAPH1	1-1132	8.88	741-1132	9.97	6	44	83
<i>Xenopus</i>	Lamellipodin/RAPH1	1-1024	8.07	615-1024	9.78	5	44	79
<i>Danio</i>	Lamellipodin/RAPH1	1-1321	8.81	913-1321	9.90	5	43	58
<i>Drosophila</i>	Pico	1-1034	8.63	695-1034	9.38	6	34	23
<i>C. elegans</i>	<i>mig-10</i> (isoform A)	1-667	7.60			1		
<i>C. elegans</i>	<i>mig-10</i> (isoform B)	1-650	8.43			1		
<i>C. elegans</i>	<i>mig-10</i> (isoform C)	1-779	5.20			1		
Human	RIAM	1-665	5.39	542-665	4.61	4	9	
<i>Listeria</i>	ActA	30-612	4.89	255-392	3.95	4	6	
Human	Zyxin	1-572	6.22	1-135	4.26	4	8	
Human	PREL1							

^a The number of arginine and lysine residues were calculated across the 'VASP BD FPPPP' region. The isoelectric point (pI) was calculated in EXPASY.

Chapter 4

A Mechanistic Framework for Actin Cytoskeleton Reorganization

by α -Catenin at Cell-Cell Contacts

Scott D. Hansen^{1,†}, Adam V. Kwiatkowski^{2,†}, Chung-Yueh Ouyang³, HongJun Liu³, Sabine Pokutta⁴, Niels Volkmann³, Dorit Hanein³, William I. Weis^{4,5}, R. Dyche Mullins^{1*} and W. James Nelson^{2,5,*}

¹Department of Cellular and Molecular Pharmacology, University of California, San Francisco School of Medicine, San Francisco, CA 94158

²Department of Biology, Stanford University, Stanford, CA 94305

³Bioinformatics and Systems Biology Program, Sanford Burnham Medical Research Institute, La Jolla, CA 92037

⁴Department of Structural Biology, Stanford University School of Medicine, Stanford, CA 94305

⁵Department of Molecular and Cellular Physiology, Stanford University School of Medicine, Stanford, CA 94305

[†]These authors contributed equally to this work

In preparation for submission to *Journal of Cell Biology*

Abstract

Transitions between cell migration and cell-cell adhesion require remodeling of the actin cytoskeleton. The actin-binding protein α E-catenin may coordinate these events since it organizes actin filaments at cadherin-based cell-cell contacts and negatively regulates actin-based membrane dynamics and cell migration, but the mechanisms are largely unknown. Here we show that the α E-catenin actin binding domain (ABD) binds cooperatively to individual actin filaments, and that binding induces a conformational change in the actin protomer that has a long-range influence on filament structure. α E-catenin ABD limits barbed end growth, but not formin-driven polymerization of unbranched filaments. Conversely, α E-catenin ABD inhibits actin filament branching by the Arp2/3 complex and severing by cofilin, activities critical for actin dynamics and turnover. These results provide a mechanistic framework for how α E-catenin may regulate changes in actin organization during cell-cell adhesion.

Introduction

The regulation of actin cytoskeleton dynamics and organization is essential for cell migration and cell-cell adhesion during embryonic development (Halbleib and Nelson, 2006), and is often altered in diseases such as metastatic cancer (Condeelis et al., 2005). The spatial organization of filamentous actin (F-actin) is different in single migrating cells and cells that form strong cell-cell adhesions; the former generally comprised a highly-branched dynamic actin network controlled by the Arp2/3 complex for lamellipodia formation and integrin mechano-transduction and dynamics (Svitkina and Borisy, 1999), while in the latter comprises bundles of unbranched filaments parallel to cell-cell adhesions (Hirokawa et al., 1983). Proteins that coordinate transitions between these distinct actin organizations, and hence cell behaviors, are unknown.

A candidate regulator of actin organization is α E-catenin, an actin-binding component of the cadherin cell-cell adhesion complex (Aberle et al., 1994; Rimm et al., 1995). In mammals, α E-catenin is allosterically regulated: the monomer binds β -catenin/cadherin, whereas the homodimer does not bind β -catenin but binds strongly to, and bundles F-actin. Significantly, depletion of the cytoplasmic pool of α E-catenin does not affect cell-cell adhesion but results in increased membrane activity and 3-5x faster cell migration (Benjamin et al., 2010), indicating that the homodimer functions separately from the cadherin-bound α E-catenin in the cytoplasm of mammalian cells as a negative regulator of membrane dynamics and cell migration. Furthermore, deletion of α E-catenin in mice causes defects in cell-cell adhesion, cell migration and proliferation

(Vasioukhin et al., 2000), and in humans coincides with metastatic cancers with a worse prognosis than deletion of E-cadherin alone (Benjamin and Nelson, 2008). Together, these results indicate that α E-catenin plays broad roles in cell-cell adhesion and cell migration. However, there is little mechanistic understanding of how α E-catenin regulates different aspects of actin polymerization and organization necessary to affect changes in cell behavior during transitions between migratory cells and more stationary cell aggregates.

Vinculin is structurally related to α E-catenin and contains a similar domain structure and is also conformationally regulated: the monomer does not bind F-actin until it is activated by talin, for example, and then undergoes a conformational change that relieves inhibition of the C-terminal actin binding domain (ABD). In comparison to the molecular understanding of how vinculin interacts with, and regulates actin organization, much less is known about α E-catenin. Previous studies showed that α E-catenin homodimers bind and bundle actin filaments, but it is not known how α E-catenin binds to actin protomers in the filament or whether this interaction affects the conformation of protomers in the actin filament, or the assembly and disassembly dynamics of F-actin. Bulk assays also showed that α E-catenin inhibits polymerization of F-actin by the Arp2/3 complex, but it is not known whether this is due to a direct effect on barbed-end polymerization and/or branching activity, or a steric effect of α E-catenin on Arp2/3 binding to F-actin. Similarly, α E-catenin binds to formins, but it is unknown whether this affects barbed end nucleation by formins. In addition to these actin nucleating activities, actin dynamics is regulated by severing proteins

such as cofilin, and it is unknown whether α E-catenin affects these activities as well.

Understanding these molecular details of how α E-catenin regulates actin dynamics may provide a mechanistic framework for how α E-catenin controls changes in cell behavior in cell-cell adhesion and cell migration. Here, we use Total Internal Reflection Fluorescence (TIRF) microscopy to examine the assembly and disassembly dynamics of individual actin filaments in the presence of actin nucleating (Arp2/3, formin, profilin) and severing proteins (cofilin) and purified α E-catenin homodimers and α E-catenin ABD. Our results show that α E-catenin binding to F-actin affects barbed-end polymerization and inhibits binding, and hence activities of the Arp2/3 complex and cofilin, but not formins. 3-dimensional reconstruction of images from cryo-electron microscope tomography shows that binding of α E-catenin ABD induces a conformational change in the actin protomer that has a long-range influence on filament structure that may structurally affect Arp2/3 complex and cofilin binding.

Results and Discussion

Mammalian α E-catenin exists as a monomer and homodimer in solution, and the oligomeric state affects F-actin binding (Drees et al., 2005). The primary F-actin binding region in α E-catenin is located in the C-terminal actin binding domain (ABD, aa 671-906), a five-helix bundle with significant homology to the corresponding domain in vinculin (Fig. 1 A). In addition to full-length α E-catenin, we used the α E-catenin ABD to eliminate complications from oligomerization (Fig. 1 A, Fig. S1).

Total Internal Reflection Fluorescence-Microscopy (TIRF-M) was used to visualize GFP-tagged α E-catenin ABD bound to actin filaments polymerized *in vitro*. GFP- α E-catenin ABD bound cooperatively to actin filaments with a Hill coefficient of 3.3 and a K_d of $\sim 0.5 \mu\text{M}$ (Fig. 1, B and C), similar to "dark" (unlabeled) α E-catenin ABD (Hill coefficient 3.6; $K_d \sim 1.0 \mu\text{M}$) measured in a bulk actin filament co-sedimentation assay (Fig. S1 D). "Dark" full-length α E-catenin dimer bound actin with a similar affinity, though the binding was less cooperative (Fig. S1 E). Consistent with cooperative binding, we observed a concentration-dependent change in the dwell time of GFP α E-catenin ABD on individual actin filaments (Fig. 1D-F; Fig. S1B and C; movie S1 and S2). When GFP α E-catenin ABD was diluted to 2 nM, the average dwell time for single molecules interacting with F-actin was $70 \pm 2 \text{ ms}$ (Fig. 1, D and E). Conversely, when 2 nM GFP α E-catenin ABD was mixed with $0.5 \mu\text{M}$ dark α E-catenin ABD, we observed two populations GFP-labeled ABD: (1) fast dissociating, $88 \pm 3 \text{ ms}$ (58%), and (2)

slow dissociating, 659 ± 15 ms (42%) (Fig. 1, D and F). The nearly 10-fold increase in the dwell time for GFP α E-catenin ABD in the presence of dark protein is consistent with a model for cooperative binding.

To understand the α E-catenin-actin filament interaction at high resolution, we obtained 3-dimensional (3D) reconstructions of cryo-electron micrographs of actin filaments decorated with α E-catenin ABD. The micrographs showed either bare actin filaments (Fig. 2 A, red filaments) or filaments completely decorated with α E-catenin ABD (Fig. 2 A, blue filaments), consistent with cooperative binding of α E-catenin ABD observed in our *in vitro* binding assay (Fig. 1). Using electron cryo-microscopy and image reconstruction techniques, we obtained reconstructions at ~ 1.8 -nm resolution for both bare actin filaments (Fig. 2 B) and actin filaments with bound α E-catenin ABD (Fig. 2 C). Both the shape and attachment angle of the extra α E-catenin ABD density on actin filaments (Fig. 2 C) were similar to that of the vinculin and metavinculin ABDs (Janssen et al., 2006; Janssen et al., 2012); note that The E-catenin ABD is structurally similar to the vinculin ABD (Bakolitsa et al., 1999; Pokutta et al., 2002), which also binds cooperatively to actin filaments (Janssen et al., 2006; Menkel et al., 1994). Furthermore, the potential binding interface of the α E-catenin ABD (green “footprint” in Fig. 2 E) matched closely to that of vinculin, and, similar to vinculin, α E-catenin ABD binding did not alter actin filament symmetry. Interestingly, we detected displacement of actin subdomain 2 away from the center of the filament when α E-catenin ABD was bound (Fig. 2 D). Since the resolution of the vinculin and metavinculin reconstructions on actin filaments are too low, we do not know

if vinculin ABD binding induces a similar displacement.

Since binding of α E-catenin to actin filaments is cooperative and affects actin protomer conformation, we examined whether binding affected actin polymerization kinetics. In the presence of 2 μ M monomeric actin, filaments nucleated spontaneously and elongated at an average rate of 16 ± 1.4 subunits/sec (Fig. 3 A; Fig. S2 A). However, in the presence of increasing concentrations of GFP α E-catenin ABD, barbed end elongation slowed significantly (11 subunits/sec; Fig. 3 A; Fig. S2). A similar, though less dramatic decrease in barbed end filament elongation was observed with untagged (dark) α E-catenin ABD (Fig. 3 A), suggesting that the GFP tag may partially interfere with barbed end elongation. Within the optical limits of our observations, barbed end elongation was continuous, suggesting that slower growth was not solely caused by intermittent pauses in growth (Fig. 3, B and C; Fig. S2 B). α E-Catenin induces actin filament bundling, and we found that the filament elongation rate in bundles generated by GFP α E-catenin ABD was even slower and largely insensitive to higher ionic strength buffers (Fig. S2 A-B; Fig. S3 A-D). Together, these results reveal that α E-catenin binding to filamentous actin reduces the rate of actin polymerization, especially during filament bundling.

The effects of α E-catenin binding on filament barbed end growth might be expected to affect the interaction of formins, which bind barbed ends and nucleate unbranched actin filaments (Kovar et al., 2006; Pruyne et al., 2002). Constitutively active formin mDia2 and 2 μ M profilin-actin produced two populations of elongating actin filaments: 1) dim, fast-growing filaments with

barbed end associated mDia2 (~25 sub/sec; Fig. 3 D; Fig. S2, C-E); and 2) bright, slow-growing filaments that lacked mDia2 (~4 sub/sec; Fig. S2 D). Importantly, growth of both populations of actin filaments was independent of α E-catenin ABD binding, except when actin filament bundling was induced by α E-catenin (Fig. 3 D; Fig. S2 E). Formins remained attached to actin filaments in bundles formed in the presence of α E-catenin ABD; however, barbed end elongation was markedly slower (Fig. S2 E; Fig. S3 B). Thus, α E-catenin does not affect formin binding to barbed ends, or formin-dependent elongation of single actin filaments. However, α E-catenin ABD binding and bundling of actin filaments does attenuate barbed end elongation, even in the presence of formins.

α E-Catenin may regulate actin polymerization and cell dynamics by the Arp2/3 complex (Benjamin et al., 2010; Drees et al., 2005; Sarpal et al., 2012). 3D reconstructions of cryo-electron micrographs showed that α E-catenin ABD binding to actin filaments induced a shift in subdomain 2 of the actin protomer (Fig. 2D), which forms part of the binding interface with the Arp2/3 complex. Therefore, we used TIRF-M to examine how α E-catenin binding to actin filaments may regulate Arp2/3 complex activity. In the presence of 1 μ M Mg-ATP-actin and the Arp2/3-activating VCA domain from SCAR, the Arp2/3 complex generated new (daughter) filaments from the sides of pre-existing (mother) filaments with a frequency of 0.13 branches/ μ m of mother filament (Fig. 4, A and C). In the presence of \geq 500 nM GFP α E-catenin ABD (Fig. 4 A) or \geq 2 μ M full-length GFP α E-catenin (Fig. 4 B; Movie S3 and S4), branching frequency induced by the Arp2.3 complex decreased 14-fold (Fig. 4 C). Thus, α E-catenin binding to

filaments inhibits the polymerization of branched actin filaments by the Arp2/3 complex.

Assembly of functional actin networks also requires proteins that catalyze filament disassembly such as the severing protein cofilin (Oser and Condeelis, 2009). Subdomain 2 of actin is actively involved in cofilin binding, and we asked if α E-catenin binding to actin filaments affected cofilin-mediated severing.

Significantly, the presence of either α E-catenin ABD or α E-catenin full-length protein reduced cofilin binding and concomitant actin filament severing in a concentration-dependent manner (Fig. 5, A and B; Movie S5). Thus, α E-catenin binding to actin filaments inhibits Arp2/3 complex-mediated branching and cofilin-mediated severing, but leaves the barbed end free for nucleation by formins. α E-catenin may affect binding of these proteins to actin filaments by local steric interference at the binding site. In addition, the observations that the ABD binds with strong cooperativity and that binding is associated with a change in subunit structure (Fig. 2) suggest that there could be changes in the filament away from the actual site of ABD binding, thereby interfering with Arp2/3 and cofilin by a long-range allosteric mechanism.

Our results provide a significant advance on understanding the interaction of α E-catenin with F-actin and, thereby, a mechanistic and structural framework for how α E-catenin binding to actin filaments may remodel the actin cytoskeleton during transitions between cell migration and cell-cell adhesion. α E-Catenin binding to actin filaments induces a conformational change in the actin protomer that effects filament structure. This may explain how α E-catenin binding inhibits

the filament branching and severing activities of the Arp2/3 complex and cofilin, respectively, but does not affect barbed end association and filament elongation by formins. Mechanistically, this effect is similar to how cofilin promotes dissociation of the Arp2/3 complex from actin filaments by changing filament conformation (Chan et al., 2009). α E-catenin binding to and bundling of actin filaments directly reduced barbed end polymerization; these properties could control the amount of actin polymerization at cell-cell adhesions, especially during α E-catenin-induced filament bundling. Thus, an increased local concentration of α E-catenin associated with cadherin complexes clustered at cell-cell adhesions could change actin filament dynamics and organization by suppressing the branched actin organization in lamellipodia of migrating cells (Drees et al., 2005; Benjamin et al., 2010) and inducing the bundled organization of long, parallel actin filaments at cell-cell contacts (Hirokawa et al., 1983). These multiple biochemical activities may explain why loss of α E-catenin has such broad effects on cell behavior in development and disease.

Materials and Methods

Protein purification and labeling

Full-length murine α E-catenin (aa 1-906) and ABD (aa 671-906) were expressed as either N-terminal GST-fusion proteins in pGEX-TEV or N-terminal His-tagged EGFP fusion proteins in pPROEX-HTa. All recombinant α E-catenin proteins were expressed in BL21 (DE3) Codon Plus *E. coli* cells (Pokutta and Weis, 2000). GST-tagged constructs bound to glutathione-agarose were equilibrated in cleavage buffer (20 mM Tris pH 8.0, 150 mM NaCl, 2 mM EDTA, 1 mM DTT and 10% glycerol) and then incubated with TEV protease overnight at 4° C to cleave the GST tag. His-tagged proteins were purified on Ni-NTA agarose beads, and eluted with imidazole. Full-length α E-catenin proteins ("dark" and EGFP-tagged) were first loaded onto a MonoQ anion exchange column and eluted with ~200 mM NaCl. Eluted monomer protein was then further purified on a Superdex200 gel filtration column in 20 mM Tris pH 8.0, 150 mM NaCl, 10% glycerol and 1 mM DTT. ABD proteins were purified using a cation exchange (MonoS column) and then by Superdex200 gel filtration in 20 mM Tris pH 8.0, 150 mM NaCl, 10% glycerol and 1 mM DTT. Eluted protein was concentrated to 30-100 μ M using a Millipore column concentrator, flash frozen and stored at 80°C.

Cytoplasmic actin was purified from *Acanthamoeba castellanii* (Gordon et al., 1976; Zuchero, 2007). Actin was stored at 4⁰C in 2 mM Tris [pH 8.0], 0.5 mM TCEP, 0.1 mM CaCl₂, 0.2 mM ATP, 0.01% azide, and used within 6 months.

Monomeric actin was labeled on Cys-374 with Cy3-maleimide (GE Healthcare) on ice in the absence of reducing agent for 15 minutes. The reaction was quenched with 10 mM DTT and then centrifuged at 100000 x g (TLA 100.4 rotor, Beckman Coulter) to remove insoluble material. Labeled actin was then polymerized at room temperature by the addition of KMEI buffer (50 mM KCl, 1 mM MgCl₂, 1 mM EGTA, 10 mM imidazole [pH 7.0]). Polymerized actin was pelleted, washed with G-buffer, and resuspended in G-buffer (2 mM Tris [pH 8.0], 0.5 mM TCEP, 0.1 mM CaCl₂, 0.2 mM ATP, 0.01% azide) to depolymerize filaments. Following depolymerization in G-buffer for 5 days, actin was hard spun, and gel filtered (Superdex 75). We typically achieved a 40-60% labeling efficiency in the recovered material. The quality of labeled actin was determined by visualization of single actin filament elongation *in vitro* using TIRF-M.

Arp2/3 was purified as described (Dayel et al., 2001). In brief, *Acanthamoeba castellanii* high speed lysate was applied to a diethylaminoethane (DEAE) column. The DEAE flow through was then applied to an NWASP^{VCA} column (NWASP covalently linked to a HiTrap NHS-activated HP column, GE Healthcare 17-0717-01). Following elution from the NWASP^{VCA} column, Arp2/3 was further purified by cation exchange (MonoS) chromatography and gel filtration (Superdex 200).

Human cofilin I was cloned into a modified pETM-Z2 vector containing a N-terminal ybbR fusion (Z-Tag-his₁₀-TEV-ybbR-hCof1) and expressed in BL21 (DE3) Rosetta cells. We used a ybbR tag with the following peptide sequence: GDSLSWLLRLLN (Zhou et al., 2007). Following microfluidization of cells and

ultracentrifugation, Z-Tag-his₁₀-TEV-ybbR-hCof1 containing bacterial lysate was batch bound to a 5mL Hi-Trap Cobalt charged column. The eluate was cleaved with TEV protease to remove Z-Tag-his₁₀. Purification of ybbR-hCof1 was achieved by cation exchange (monoS) and size exclusion (Superdex 200) chromatography. Pure ybbR-hCof1 was subsequently labeled *in vitro* using purified Sfp phosphopantetheinyl transferase and Atto488-CoA (NEB S9348S) as described (Yin et al., 2005). Atto488-ybbR-hCof1 was functionally indistinguishable from human cofilin in our single actin filament TIRF assay as well as solution based actin filament severing assays (SH, unpublished results).

Constitutively active his₁₀-TEV-mDia2^(519-1171aa) was expressed in BL21 (pRARE) bacteria overnight at 16^oC in the presence of 50μM IPTG. Cells were lysed into buffer containing 20mM Tris pH 8, 400mM NaCl, 0.5mM BME, and 1mM PMSF. High speed supernatant was then pumped over a 5mL HiTrap Cobalt Chelating column, washed, and then eluted with buffer containing 20mM Tris pH 8, 250mM imidazole, 400mM NaCl, 0.5mM BME. TEV protease was added to cleave the his₁₀ tag and the eluate was dialyzed into 10mM Hepes pH 7.5, 200mM NaCl, 1mM EDTA and 5mM BME overnight. Dialysate was flowed over NiNTA resin to remove uncleaved protein and his₁₀-TEV. Cleaved mDia2 was then loaded onto a Superdex 200 gel filtration column (323mL), equilibrated with 10mM Hepes pH 7.5, 200mM NaCl, 1mM EDTA, and 5mM BME. The dimer peak was pooled and immediately diluted into buffer such that the [NaCl]_{final} = 50-75mM. mDia2 was then loaded onto a MonoS column and eluted over 35CV with 7.5-40% of 1M NaCl gradient. Two peaks eluted from the column, each

having different nucleation activities in a pyrene assay. The high salt peak had more activity and was therefore used for experiments. Pure mDia2^(519-1171aa)^{M1041A} off the MonoS column (high salt peak) was dialyzed into 10mM HEPES pH 7.5, 100mM NaCl, 1mM TCEP, 20% glycerol overnight and then frozen with liquid nitrogen. The activity of mDia2, frozen and unfrozen, were indistinguishable.

Glass silanization and pegylation

Glass was functionalized as described (Bieling et al.) with modifications. In brief, coverglass (Corning No. 1.5, 18x18 mm sq.) was cleaned by sonication in 3M NaOH, followed by Piranha etching (40% hydrogen peroxide, 60% sulfuric acid). After washing glass with MilliQ water, coverslip sandwich were incubated with 100% GOPTS for 30 minutes at 75⁰C. Glass was then washed with anhydrous acetone (Electron Microscopy Sciences; RT 10016) to remove excess silane. Next, dry hydroxyl-PEG_{3000 Da}-NH₂ (95%) and CH₃O-Biotin-PEG_{3000 Da}-NH₂ (5%) were combined using a mortar and pestle (Cat # 10-3000-20 and 10-3000-25-20 respectively; Rapp Polymere). The dry 95/5 amino-PEG mixture was then melted onto clean silanized coverslips (~ 8mg total per coverslip sandwich) and baked for ≥ 8 hours at 75⁰C in glass weigh jars (Fisher, Cat# 03-420-5C). The glass was then washed with copious amounts of MilliQ water before spin drying and storage in a dust free container at room temperature.

Single actin filament TIRF assay

Counter glass slides (24 x 75 x 1 mm, Fisher 12-544-7) were sonicated in 3M NaOH, followed by washes with water and sonication in 100% ethanol. To minimize protein depletion effects, counter glass slides were coated with poly-L-lysine-PEG as described (Huang et al., 2000). PLL-PEG was allowed to dry on the glass before rinsing off excess reagent with MilliQ water. PEG functionalized coverslips (18x18 mm) were then attached to the PLL-PEG coated counter glass slides with double stick tape. To reduce nonspecific binding to the PEG functionalized imaging chamber was washed with a 1x phosphate buffer saline (PBS) [pH 7.2] containing 1% Pluronic F-127 (Sigma P2443) and 100 µg/mL kappa casein (Sigma C0406). Glass was then washed with buffer containing 10mM HEPES [pH 7.0], 2 mM TCEP, 200 mM KCl, and 1 mg/mL BSA. Next, 50 nM streptavidin (Rockland Immunochemicals S00-01) was flowed into the imaging chamber and incubated for 30 seconds. Finally, the flow chamber was incubated with 50 nM biotin-PEG₁₁ heavy meromyosin (EZ-Link Maleimide-PEG11-Biotin, Fisher Thermo Scientific/Pierce, #21911) for 30 seconds before washing out excess biotin-HMM.

The single actin filament TIRF assay was performed as described (Hansen and Mullins). In brief, actin polymerization reactions were initiated by combining 1µL of 10x ME (2 mM EGTA, 0.5 mM MgCl₂) with 9µL of 4.44µM monomeric actin (10-20% Cy3 labeled) for 2 minutes at room temperature. The Mg-ATP-Actin was then combined with TIRF buffer to reach a final buffer

composition of 1 μ M actin (5-10% Cy3 labeled), 10 mM imidazole [pH 7.0]. 1 mM EGTA, 1 mM $MgCl_2$, 50-100 mM KCl, 0.2% methylcellulose (cP400, Sigma M0262), 1 mg/mL BSA (Sigma A0281), 20 mM beta-mercaptoethanol (Sigma M6250), 20 mM glucose, 0.2 mM ATP (Sigma 26209), 125 μ g/mL glucose oxidase (Biophoretics/Serva Electrophoresis #22778.01), and 20 μ g/mL catalase (Sigma, C40-100MG from Bovine liver). The glucose oxidase and catalase solutions were made fresh from dry reagents, ultracentrifuged to remove debris (TLA120.1, 278,587 x g, 20 minutes), and used within 3 days.

Actin cosedimentation assay

Chicken G-actin was incubated in polymerization buffer (20 mM HEPES 7.5 or 20 mM Tris pH 8.0, 100 mM KCl, 2 mM $MgCl_2$, 0.5 mM ATP, 1 mM EGTA) for 1 hour at room temperature to polymerize filaments. α E-catenin was diluted to various concentrations in reaction buffer (20 mM HEPES 7.5 or 20 mM Tris pH 8.0, 150 mM NaCl, 2 mM $MgCl_2$, 0.5 mM ATP, 1 mM EGTA, 1 mM DTT) with and without 2 μ M F-actin and incubated for 30 minutes at RT. Samples were centrifuged at 100,000 rpm for 20 minutes in a TLA 120.1 rotor. Supernatant and pellet samples were diluted in Laemmli sample buffer, separated by SDS-PAGE and stained with either Coomassie blue or SYRPO Ruby gel stain. Gels were imaged on a LI-COR (Coomassie stain) or Typhoon (SYPRO stain) scanners, and measured and quantified in ImageJ. Binding data was processed with Prism software.

Fluorescence Microscopy, Software, and Data Analysis

All TIRF microscopy data was collected on a Nikon Eclipse TE2000-E using Nikon Perfect focus at 25⁰C. All images were acquired with a cooled Andor iXon EMC CD camera using Micromanager 3.0 software (Stuurman et al., 2007). Fluorescent dyes were excited through a 100x Apo Nikon TIRF objective (NA 1.49) using either a 491 nm (50 mW) or 561 nm (50 mW) laser.

Curve fitting for determination of the K_d of filamentous actin binding of GFP aE-catenin was solved using Prism software using a one-site specific binding model with Hill coefficient. Single molecule lifetime data for GFP aE-catenin were fit to either a single exponential of $\log_{10}(1-CF) [1*\exp(-M0/m1)]$ or a double exponential of $\log_{10}(1-CF) [m2*\exp(-M0/m1)+(1-m2)*\exp(-M0/m3)]$ using KaleidaGraph software. Error bars for dwell times are the standard error of measure (SEM) from curve fitting. The statistical significance of the aE-catenin dependent changes in single actin filament barbed end polymerization rates was evaluated using an unpaired two tail student t-test in Microsoft Excel. Final figures were generated using ImageJ, Photoshop CS3, and Illustrator CS3.

Electron microscopy and Image Analysis

Rabbit skeletal muscle actin was prepared and stored as described (Volkman et al., 2000). F-actin was used within 1-2 weeks of preparation. Flashed-frozen aE-catenin ABD was used within the week of thawing. Both F-actin and ABD α E-catenin were diluted to 5 mM NaPO₄ (7.0), 60 mM NaCl, 1 mM MgCl₂, 0.1 mM EGTA, 2mM NaN₃. Actin filaments were diluted to 0.02 mg/ml

and α E-catenin ABD samples were diluted to 0.05 mg/ml. After 10 min incubation, 4 μ l from the final 1:2 w/w mixture was applied to UV glow discharged 400-mesh copper grids coated with Holey Triafol carbon film made in house. After 1 min of incubation in a humidified chamber, the excess of liquid was blotted and the samples were plunge-frozen in liquid-nitrogen-cooled liquefied ethane. Low-dose images were recorded with a Tecnai F20 (FEG) electron microscope (FEI, Company, Hillsboro, OR) at a nominal magnification of 50,000 at 200 keV and 2.5 μ m defocus (electron dose 20 $e^-/\text{\AA}^2$). The micrographs (Kodak Electron Image Film SO-163) were digitized with a SCAI scanner (Hexagon Geosystems, Madison, AL) with a pixel size of 0.3 nm on the sample. Two independent biochemical preparations of ABD α E-catenin were used.

Iterative reconstruction and sorting procedure

For this study, we employed an iterative reconstruction/sorting protocol. For the reconstruction component, we use a modified protocol of the iterative helical real space reconstruction method (Egelman, 2000). The modification uses components from EMAN (Ludtke et al., 1999), SPARX (Hohn et al., 2007) and CoAn (Volkman and Hanein, 1999) and was shown to give higher fidelity in the angle assignment step and allows back-mapping of the segments included in the final reconstruction (Volkman et al., 2005). The selected segments were 40x40 nm (about 15 actin subunits) and spaced \sim 5.5 nm apart along the axis of filaments in the micrographs (Fig. 2A). A total of 34,390 segments were selected from 33 micrographs after correction for the contrast transfer of the microscope

(Mallick et al., 2005). For the initial sorting step, we aligned all selected segments along their helical axis; then, we projected the intensities down the helical axis for each segment, resulting a one-dimensional intensity profile for each selected segment. Since a complete crossover of the filament is contained in each segment, the profiles are invariant of location along the filament. Furthermore, the averaging along the axis improves the signal-to-noise dramatically. As a consequence, the profiles are highly sensitive to changes in filament width, i.e. the presence or absence of bound material.

Once we generated the intensity profiles as described, we used reference-free K-means clustering to classify the segments. The data segregated readily into two main groups with a significant difference in width. These two groups were then separately reconstructed using a cylindrical density as reference and the standard actin-filament symmetry parameters (rise 2.75 nm, twist -166.66°) as a starting point. To ensure absence of bias, we also used perturbed symmetry values (rise ± 1 , rise ± 3) as starting points, which converged to the same reconstructions/symmetry as those started with actual actin symmetry. The resulting reconstructions were already very similar to those shown in Fig. 2 with one resembling bare actin, the other showing clear extra density. To improve resolution and correct for possible misclassifications from the intensity profiles, we used these initial reconstructions for reference-based sorting of the segments, iterating the process until convergence, i.e. until no segments swapped classes (3 rounds). Only 5% of the segments were reclassified from the original assignment, attesting the robustness and efficiency of the profile-based

sorting procedure. The final classes contained 22,740 and 11,650 segments for the bare and decorated filaments, respectively. The resolution of the reconstructions (~1.8 nm) was determined with the 0.5 cutoff criterion of the Fourier shell correlation. Optimal alignment of the maps was achieved using CoAn (Volkman and Hanein, 1999). The “footprint” of the extra density was determined by calculating a difference map of decorated minus bare filaments from the aligned maps and then mapping the close contacts between the difference map and the bare filament reconstruction onto the bare filament reconstruction.

Abbreviations List

ABD, actin binding domain; GFP, green fluorescent protein; SAXS, small-angle X-ray scattering.

Acknowledgements: We thank Jim Bear for helpful comments. This work was supported by GM035527 (WJN), GM56169 (WIW), 1U01GM094663 (WJN, WIW, NV, DH), GM61010 (RDM) and a National Science Foundation Predoctoral Fellowship (SDH). We would like to thank Peter Bieling (Mullins lab, UCSF) for purified and labeled ybbr-Atto488-cofilin.

References

- Aberle, H., S. Butz, J. Stappert, H. Weissig, R. Kemler, and H. Hoschuetzky. 1994. Assembly of the cadherin-catenin complex in vitro with recombinant proteins. *J Cell Sci.* 107 (Pt 12):3655-3663.
- Bakolitsa, C., J.M. de Pereda, C.R. Bagshaw, D.R. Critchley, and R.C. Liddington. 1999. Crystal structure of the vinculin tail suggests a pathway for activation. *Cell.* 99:603-613.
- Benjamin, J.M., A.V. Kwiatkowski, C. Yang, F. Korobova, S. Pokutta, T. Svitkina, W.I. Weis, and W.J. Nelson. 2010. AlphaE-catenin regulates actin dynamics independently of cadherin-mediated cell-cell adhesion. *J Cell Biol.* 189:339-352.
- Benjamin, J.M., and W.J. Nelson. 2008. Bench to bedside and back again: molecular mechanisms of alpha-catenin function and roles in tumorigenesis. *Semin Cancer Biol.* 18:53-64.
- Bieling, P., I.A. Telley, C. Hentrich, J. Piehler, and T. Surrey. Fluorescence microscopy assays on chemically functionalized surfaces for quantitative imaging of microtubule, motor, and +TIP dynamics. *Methods Cell Biol.* 95:555-580.
- Chan, C., C.C. Beltzner, and T.D. Pollard. 2009. Cofilin dissociates Arp2/3 complex and branches from actin filaments. *Curr Biol.* 19:537-545.
- Condeelis, J., R.H. Singer, and J.E. Segall. 2005. The great escape: when cancer cells hijack the genes for chemotaxis and motility. *Annu Rev Cell Dev Biol.* 21:695-718.
- Dayel, M.J., E.A. Holleran, and R.D. Mullins. 2001. Arp2/3 complex requires hydrolyzable ATP for nucleation of new actin filaments. *Proc Natl Acad Sci U S A.* 98:14871-14876.
- Drees, F., S. Pokutta, S. Yamada, W.J. Nelson, and W.I. Weis. 2005. Alpha-catenin is a molecular switch that binds E-cadherin-beta-catenin and regulates actin-filament assembly. *Cell.* 123:903-915.
- Egelman, E.H. 2000. A robust algorithm for the reconstruction of helical filaments using single-particle methods. *Ultramicroscopy.* 85:225-234.
- Gordon, D.J., E. Eisenberg, and E.D. Korn. 1976. Characterization of cytoplasmic actin isolated from *Acanthamoeba castellanii* by a new method. *J Biol Chem.* 251:4778-4786.

- Halbleib, J.M., and W.J. Nelson. 2006. Cadherins in development: cell adhesion, sorting, and tissue morphogenesis. *Genes & development*. 20:3199-3214.
- Hansen, S.D., and R.D. Mullins. VASP is a processive actin polymerase that requires monomeric actin for barbed end association. *J Cell Biol*. 191:571-584.
- Hirokawa, N., T.C. Keller, 3rd, R. Chasan, and M.S. Mooseker. 1983. Mechanism of brush border contractility studied by the quick-freeze, deep-etch method. *J Cell Biol*. 96:1325-1336.
- Hohn, M., G. Tang, G. Goodyear, P.R. Baldwin, Z. Huang, P.A. Penczek, C. Yang, R.M. Glaeser, P.D. Adams, and S.J. Ludtke. 2007. SPARX, a new environment for Cryo-EM image processing. *J Struct Biol*. 157:47-55.
- Huang, N.-P., R. Michel, J. Voros, M. Textor, R. Hofer, A. Rossi, D.L. Elbert, J.A. Hubbell, and N.D. Spencer. 2000. Poly(l-lysine)-g-poly(ethylene glycol) Layers on Metal Oxide Surfaces: Surface-Analytical Characterization and Resistance to Serum and Fibrinogen Adsorption. *Langmuir*. 17:489-498.
- Janssen, M.E., E. Kim, H. Liu, L.M. Fujimoto, A. Bobkov, N. Volkmann, and D. Hanein. 2006. Three-dimensional structure of vinculin bound to actin filaments. *Mol Cell*. 21:271-281.
- Janssen, M.E., H. Liu, N. Volkmann, and D. Hanein. 2012. The C-terminal tail domain of metavinculin, vinculin's splice variant, severs actin filaments. *J Cell Biol*. 197:585-593.
- Kovar, D.R., E.S. Harris, R. Mahaffy, H.N. Higgs, and T.D. Pollard. 2006. Control of the assembly of ATP- and ADP-actin by formins and profilin. *Cell*. 124:423-435.
- Ludtke, S.J., P.R. Baldwin, and W. Chiu. 1999. EMAN: semiautomated software for high-resolution single-particle reconstructions. *J Struct Biol*. 128:82-97.
- Mallick, S.P., B. Carragher, C.S. Potter, and D.J. Kriegman. 2005. ACE: automated CTF estimation. *Ultramicroscopy*. 104:8-29.
- Menkel, A.R., M. Kroemker, P. Bubeck, M. Ronsiek, G. Nikolai, and B.M. Jockusch. 1994. Characterization of an F-actin-binding domain in the cytoskeletal protein vinculin. *J Cell Biol*. 126:1231-1240.
- Oser, M., and J. Condeelis. 2009. The cofilin activity cycle in lamellipodia and invadopodia. *J Cell Biochem*. 108:1252-1262.

- Pokutta, S., F. Drees, Y. Takai, W.J. Nelson, and W.I. Weis. 2002. Biochemical and structural definition of the I-afadin- and actin-binding sites of alpha-catenin. *J Biol Chem.* 277:18868-18874.
- Pokutta, S., and W.I. Weis. 2000. Structure of the dimerization and beta-catenin-binding region of alpha-catenin. *Mol Cell.* 5:533-543.
- Pruyne, D., M. Evangelista, C. Yang, E. Bi, S. Zigmond, A. Bretscher, and C. Boone. 2002. Role of formins in actin assembly: nucleation and barbed-end association. *Science.* 297:612-615.
- Rimm, D.L., E.R. Koslov, P. Kebriaei, C.D. Cianci, and J.S. Morrow. 1995. Alpha 1(E)-catenin is an actin-binding and -bundling protein mediating the attachment of F-actin to the membrane adhesion complex. *Proc Natl Acad Sci U S A.* 92:8813-8817.
- Sarpal, R., M. Pellikka, R.R. Patel, F.Y.W. Hui, D. Godt, and U. Tepass. 2012. Mutational analysis supports a core role for Drosophila α -Catenin in adherens junction function. *Journal of Cell Science.* 125:233-245.
- Stuurman, N., N. Amoday, and R.D. Vale. 2007. μ Manager: Open Source software for light microscopy imaging. *Microscopy Today.* 15:42-43.
- Svitkina, T.M., and G.G. Borisy. 1999. Arp2/3 complex and actin depolymerizing factor/cofilin in dendritic organization and treadmilling of actin filament array in lamellipodia. *J Cell Biol.* 145:1009-1026.
- Vasioukhin, V., C. Bauer, M. Yin, and E. Fuchs. 2000. Directed actin polymerization is the driving force for epithelial cell-cell adhesion. *Cell.* 100:209-219.
- Volkman, N., and D. Hanein. 1999. Quantitative fitting of atomic models into observed densities derived by electron microscopy. *J Struct Biol.* 125:176-184.
- Volkman, N., D. Hanein, G. Ouyang, K.M. Trybus, D.J. DeRosier, and S. Lowey. 2000. Evidence for cleft closure in actomyosin upon ADP release. *Nat Struct Biol.* 7:1147-1155.
- Volkman, N., H. Liu, L. Hazelwood, E.B. Kremmentsova, S. Lowey, K.M. Trybus, and D. Hanein. 2005. The structural basis of myosin V processive movement as revealed by electron cryomicroscopy. *Mol Cell.* 19:595-605.
- Yin, J., P.D. Straight, S.M. McLoughlin, Z. Zhou, A.J. Lin, D.E. Golan, N.L. Kelleher, R. Kolter, and C.T. Walsh. 2005. Genetically encoded short

peptide tag for versatile protein labeling by Sfp phosphopantetheinyl transferase. *Proc Natl Acad Sci U S A*. 102:15815-15820.

Zhou, Z., P. Cironi, A.J. Lin, Y. Xu, S. Hrvatin, D.E. Golan, P.A. Silver, C.T. Walsh, and J. Yin. 2007. Genetically encoded short peptide tags for orthogonal protein labeling by Sfp and AcpS phosphopantetheinyl transferases. *ACS Chem Biol*. 2:337-346.

Zuchero, J.B. 2007. In vitro actin assembly assays and purification from *Acanthamoeba*. *Methods Mol Biol*. 370:213-226.

Figure Legends

Figure 1

α E-catenin ABD binds cooperatively to F-actin

(A) Localization of 1 μ M GFP α E-catenin ABD bound to phalloidin-stabilized Cy3-labeled F-actin. Scale bar 5 μ m.

(B) Average fluorescent signal of GFP α E-catenin ABD bound to single actin filaments plotted against total concentration of GFP α E-catenin. Each data point represents average GFP fluorescence per pixel measured over ≥ 100 μ m of single actin filaments (≥ 2 samples). Data were fit to either a Hill equation (black, straight line) or a hyperbolic function (red, dashed line).

(C) Kymographs showing 2 nM GFP α E-catenin ABD bound to single actin filaments in the absence or presence of 0.5 μ M dark α E-catenin ABD.

(D-E) Histograms of 2 nM GFP α E-catenin ABD dwell time on F-actin in the absence (D) or presence (E) of 0.5 μ M dark α E-catenin ABD. Inset shows curve fit of the 1-cumulative frequency **(D)**. Single exponential fit ($t_1=70 \pm 2$ ms, $n=1244$ molecules). **(E)** Double exponential fit ($t_1=88 \pm 3$ ms (58%), $t_2=659 \pm 15$ ms (42%), $n=1289$ molecules).

(F) Electron micrographs of actin filaments in the presence of α E-catenin ABD. ABD-bound filaments psuedo-colored red; naked filaments colored yellow. Scale bar 50 nm.

Figure 2

Electron cryo-microscopy and 3D reconstructions of actin filaments in the presence of α -E-catenin actin-binding domain (ABD)

- (A)** Typical field of view. The centers of segments used for the reconstructions are marked in red (bare actin) and cyan (decorated actin). The assignment was done using a bias-free iterative sorting procedure. The distance between segments is ~ 5.5 nm, the distance between two neighboring actin subunits along the long-pitch helix (see B). The bar represents 120 nm. **(B)** Reconstruction of bare actin filaments. The actin subdomains 1-4 are marked for one subunit. The distance between actin subunits along the long-pitch helix is indicated on the left.
- (C)** Reconstruction of actin filaments decorated with α -E-catenin ABD. The bar represents 4 nm.
- (D)** Overlay of reconstruction of decorated (yellow) and bare (red) actin filaments reveals a shift of actin subdomain 2 away from the filament center upon binding of α -catenin ABD.
- (E)** The “footprint” (green) of the extra density in the decorated filaments on the bare actin filament. This indicates the potential binding surfaces of the α -catenin ABD, which matches closely those observed for vinculin and metavinculin ABDs (Janssen et al., 2006; Janssen et al., 2012). Bar represents 2 nm.

Figure 3

aE-catenin ABD reduces barbed end polymerization

(A) Average barbed end polymerization rates measured in the presence of 4 μM Mg-ATP-actin (5% Cy3 labeled) plus 4 μM profilin, in the presence of either 2 μM GFP aE-catenin ABD or 2 μM aE-catenin ABD. Error bars indicate SD ($n \geq 30$ actin filaments from ≥ 2 experiments).

(B) Kymograph of actin filament bundling in the presence of 4 μM Mg-ATP-Actin (5% Cy3 labeled), 4 μM human profilin I, and 2 μM GFP $\alpha\text{E-catenin ABD}$. White dashed line indicates barbed end elongation of single actin filament; black dashed lines indicate bundled actin filaments. Arrowheads point to pauses in barbed end elongation.

(E) Quantification of single actin filament barbed end polymerization rates in the presence of 2 μM Mg-ATP-Actin (10% Cy3-labeled), 2 μM profilin I, 0.25 nM mDia2, and 2 μM GFP $\alpha\text{E-catenin ABD}$. Error bars indicate SD ($n \geq 30$ actin filaments from ≥ 2 experiments).

Figure 4

aE-catenin inhibits Arp2/3 complex branching

(A) Images of 1 μM Cy3-labeled Mg-ATP-actin polymerized with 50 nM Arp2/3 complex and 100 nM SCAR^{VCA} only or with increasing concentrations of either GFP aE-catenin ABD or full-length GFP aE-catenin.

(B) Quantification of filament branching frequency. Error bars indicate SD (≥ 200 μm of F-actin from ≥ 2 samples).

Figure 5

aE-catenin inhibits cofilin severing

(A) Montage of Cy3-labeled ADP actin filaments with 75 nM Atto488-ybbr-hCofilin alone or with aE-catenin ABD or full-length aE-catenin.

(B) Quantification of cofilin severing of actin filaments. Error bars indicate SD ($\geq 200 \mu\text{m}$ of filamentous actin from ≥ 2 experiments).

Supplemental Figure 1

α E-catenin binds cooperatively to filamentous actin

(A) Representative images of GFP α E-catenin ABD binding to F-actin *in vitro*. Localization of 25 nM to 4 μM GFP α E-catenin ABD bound to phalloidin-stabilized F-actin (20% Cy3 labeled).

(B) Kymograph of 2nM GFP α E-catenin ABD binding to filamentous actin (20% Cy3 labeled, phalloidin stabilized) in the presence of 1 μM dark α E-catenin ABD.

(C) Histogram of lifetimes for 2 nM GFP α E-catenin ABD binding to filamentous actin in the presence of 1 μM dark α E-catenin ABD. Dwell times greater than 2 seconds were omitted from the histogram for display purposes only. Inset graph shows double exponential fit of the $\log_{10}(1-CF)$ for 2nM GFP α E-catenin ABD binding in the presence of 1 μM dark α E-catenin ABD ($\tau_1=144 \pm 4 \text{ ms}$ (64%), $\tau_2=986 \pm 26 \text{ ms}$ (36%), $n=1210$ molecules).

(D-E) Bulk actin filament pelleting assays with α E-catenin ABD **(D)** and full-length α E-catenin dimer **(E)**. Bound α E-catenin (μM) was plotted against free α E-

catenin (μM), and data were fit to a Hill equation (red line; K_d and Hill coefficient listed in red) or hyperbolic function (green line; K_d listed in green). Data shown are representative of ≥ 3 experiments for αE -catenin ABD and dimer.

Supplemental Figure 2

αE -catenin ABD reduces barbed end polymerization

(A) Average barbed end polymerization rate in $2 \mu\text{M}$ Mg-ATP-actin (10% Cy3 labeled) was measured with increasing concentrations of GFP αE -catenin ABD. Error bars indicate SD ($n \geq 30$ actin filaments from ≥ 2 experiments).

(B) Kymographs of Cy3-labeled actin filaments growing with or without $2 \mu\text{M}$ GFP αE -catenin ABD. Arrowheads mark pauses in barbed end elongation (frequency was 0.087 min^{-1} , average lifetime was 62 ± 36 seconds, $n=32$ pauses).

(C) Barbed end growth rates $4 \mu\text{M}$ Mg-ATP-actin (5% Cy3 labeled) and $4 \mu\text{M}$ profilin, in the presence of either $2 \mu\text{M}$ GFP αE -catenin ABD or $2 \mu\text{M}$ αE -catenin ABD.

(D) Kymograph of actin filament bundling in the presence of $4 \mu\text{M}$ Mg-ATP-Actin (5% Cy3 labeled), $4 \mu\text{M}$ human profilin I, and $2 \mu\text{M}$ GFP αE -catenin ABD. White dashed line indicates barbed end elongation of single actin filament; black dashed lines indicate bundled actin filaments. Arrowheads point to pauses in barbed end elongation.

(E) Quantification of single actin filament barbed end polymerization rates in the presence of $2 \mu\text{M}$ Mg-ATP-Actin (10% Cy3-labeled), $2 \mu\text{M}$ profilin I, 0.25 nM

mDia2, and 2 μ M GFP α E-catenin ABD. Error bars indicate SD ($n \geq 30$ actin filaments from ≥ 2 experiments).

(F-H) Kymograph showing formin-dependent barbed end elongation of a single actin filament (**F**), change in barbed end elongation rate after mDia2 dissociation (**G**, arrowhead marks release), and barbed end elongation in the presence of mDia2 and 2 μ M GFP α E-catenin ABD (**H**). mDia2-mediated barbed end elongation of a single actin filament (white, dashed lines) and GFP α E-catenin ABD-dependent actin bundles (black, dashed lines). Arrowheads indicate pauses in mDia2 barbed end elongation (numbers are subunits/sec).

Supplemental Figure 3

Localization GFP α E-catenin ABD during actin filament bundling

(A) Montage of 2 μ M Mg-ATP-Actin (10% Cy3 labeled) polymerizing and bundling in the presence of 0.25 μ M GFP α E-catenin ABD. We observed a 2.9-fold increase in GFP α E-catenin ABD fluorescence per actin filament at sites of bundling. Scale bar is 10 μ m.

(B) Kymograph of actin filaments bundling in the presence of 2 μ M Mg-ATP-Actin (10% Cy3 labeled) and 0.25 μ M GFP α E-catenin ABD. Note the change BE growth during filament bundling. Vertical scale is 1 minute. Horizontal scale bar 5 μ m.

(C) Barbed end growth rates with 2 μ M GFP α E-catenin ABD and increasing concentrations of KCl. Note barbed end elongation in actin filament bundles was still delayed in high salt.

(D) Kymograph showing bundling dependent delay in barbed end filament elongation in the presence of 2 μM Mg-ATP-actin, 2 μM GFP αE -catenin ABD and 150 mM KCl.

Figure 1

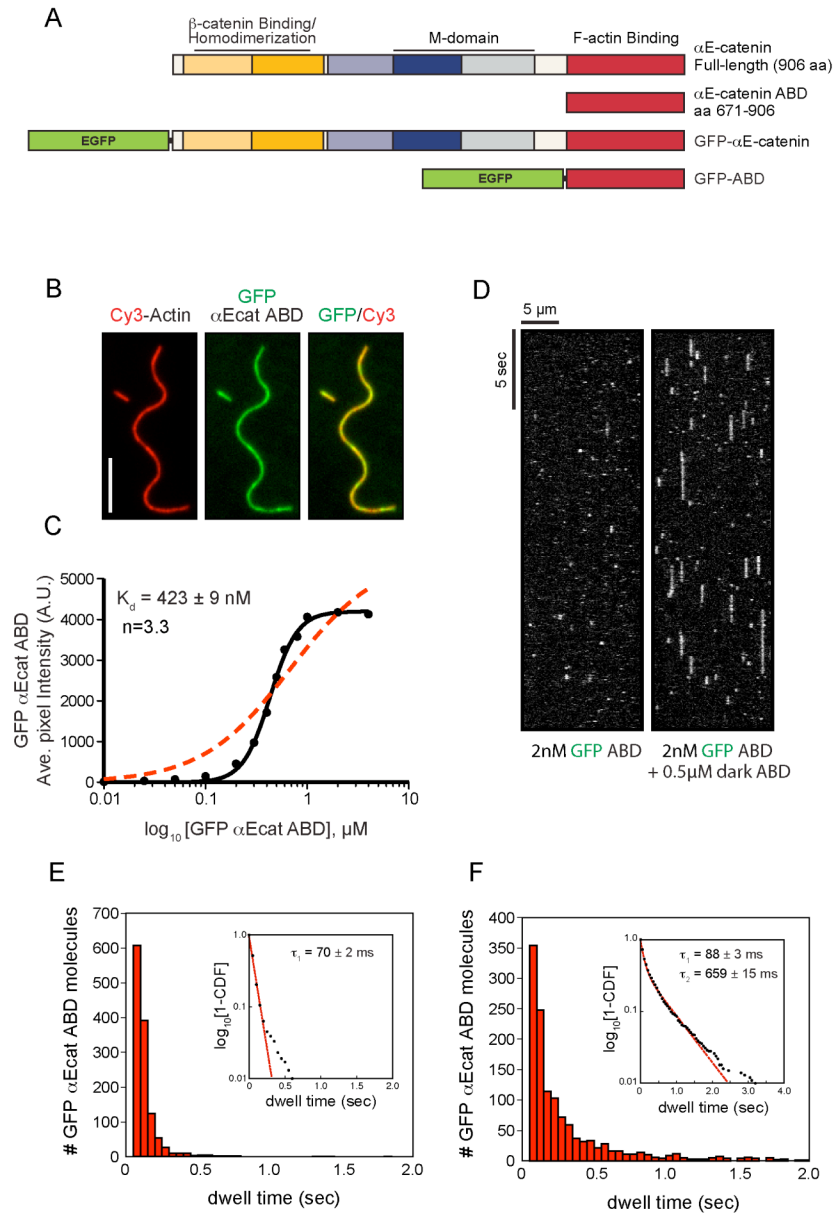


Figure 2

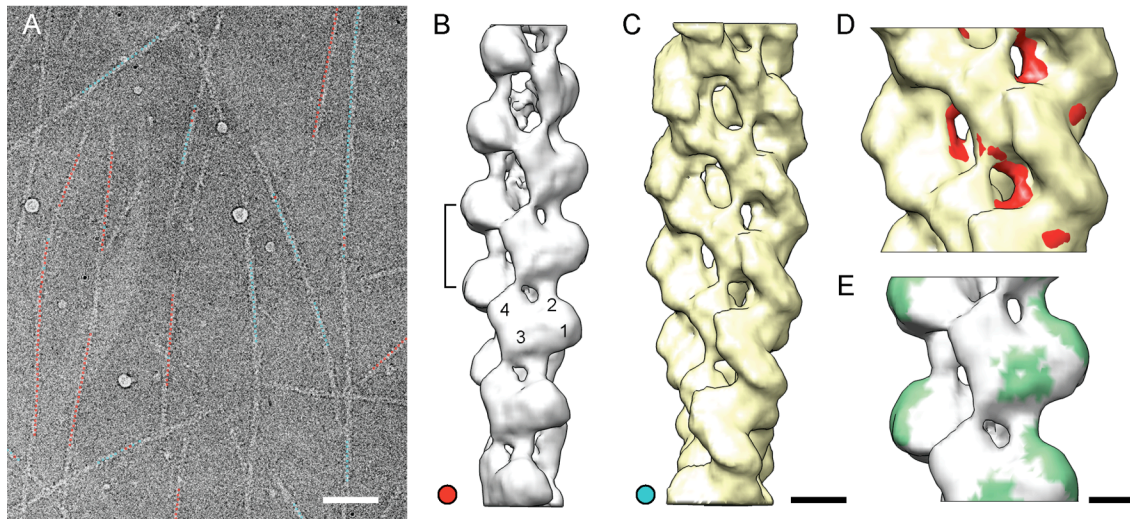


Figure 3

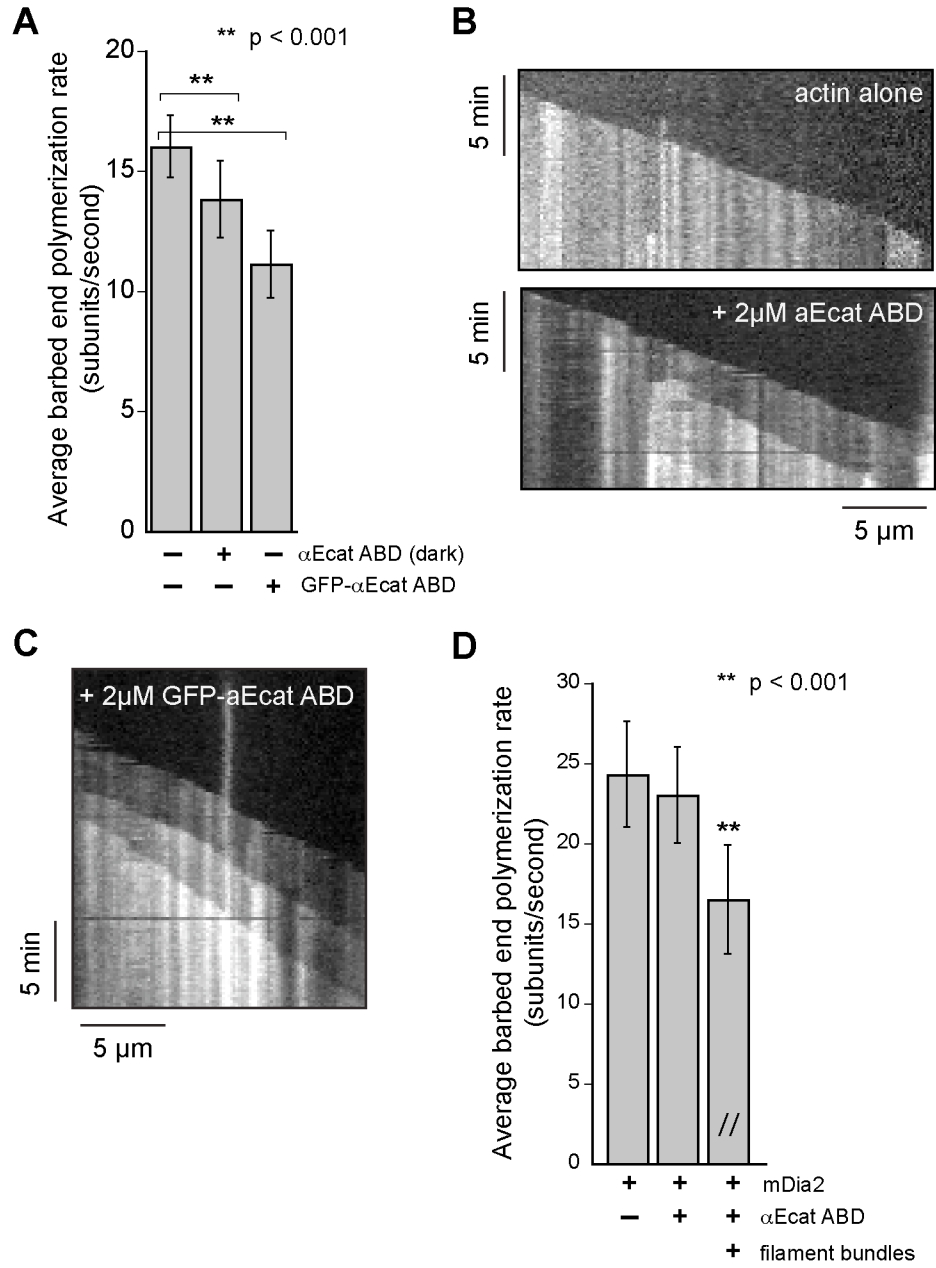


Figure 4

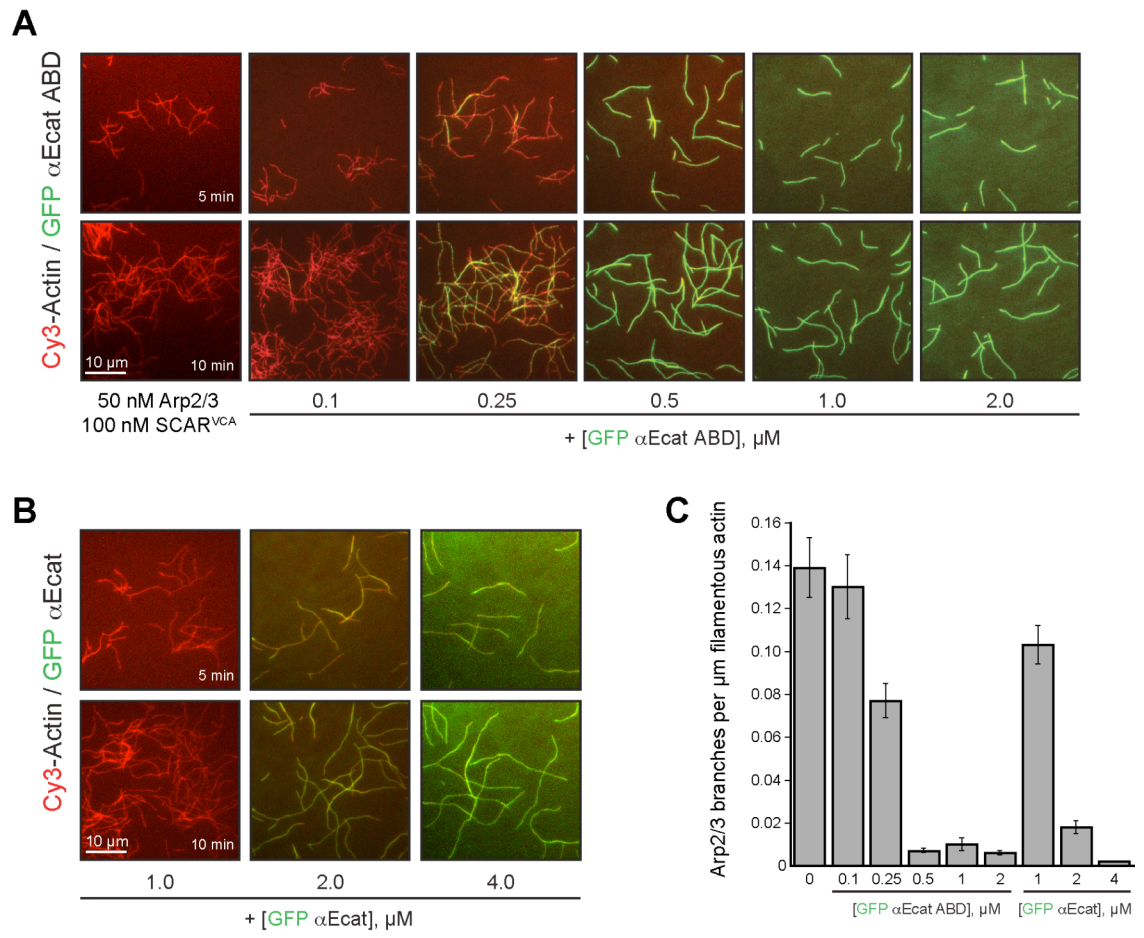
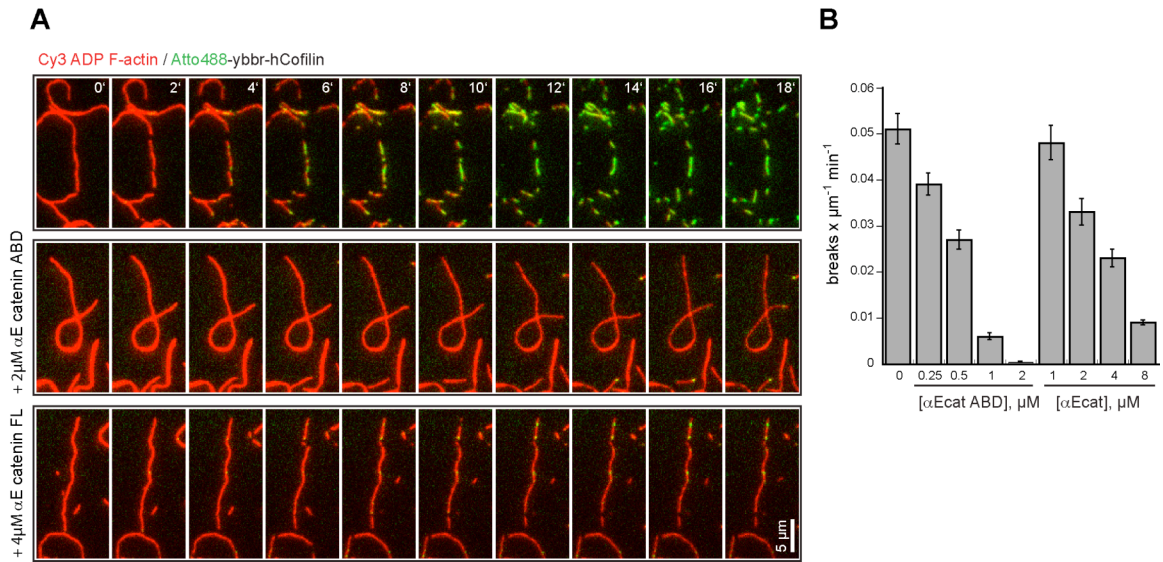
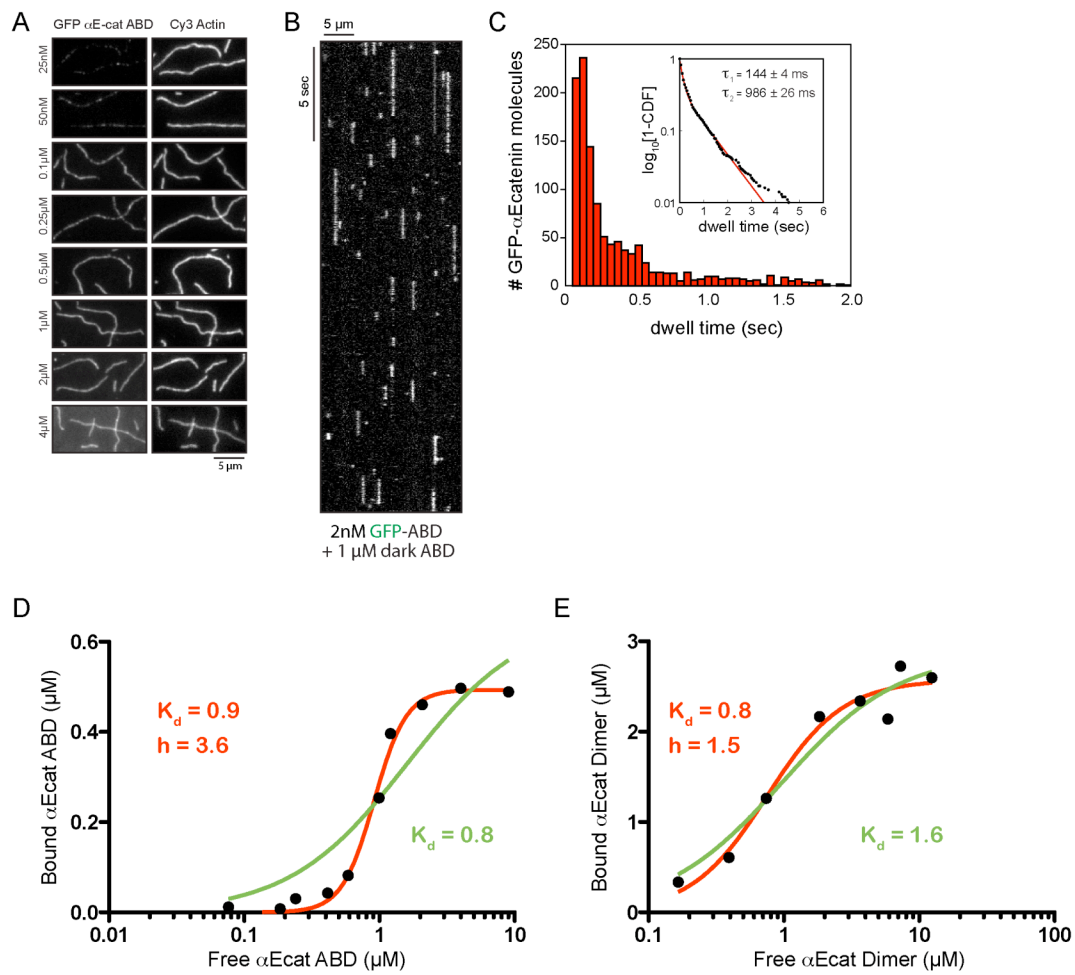


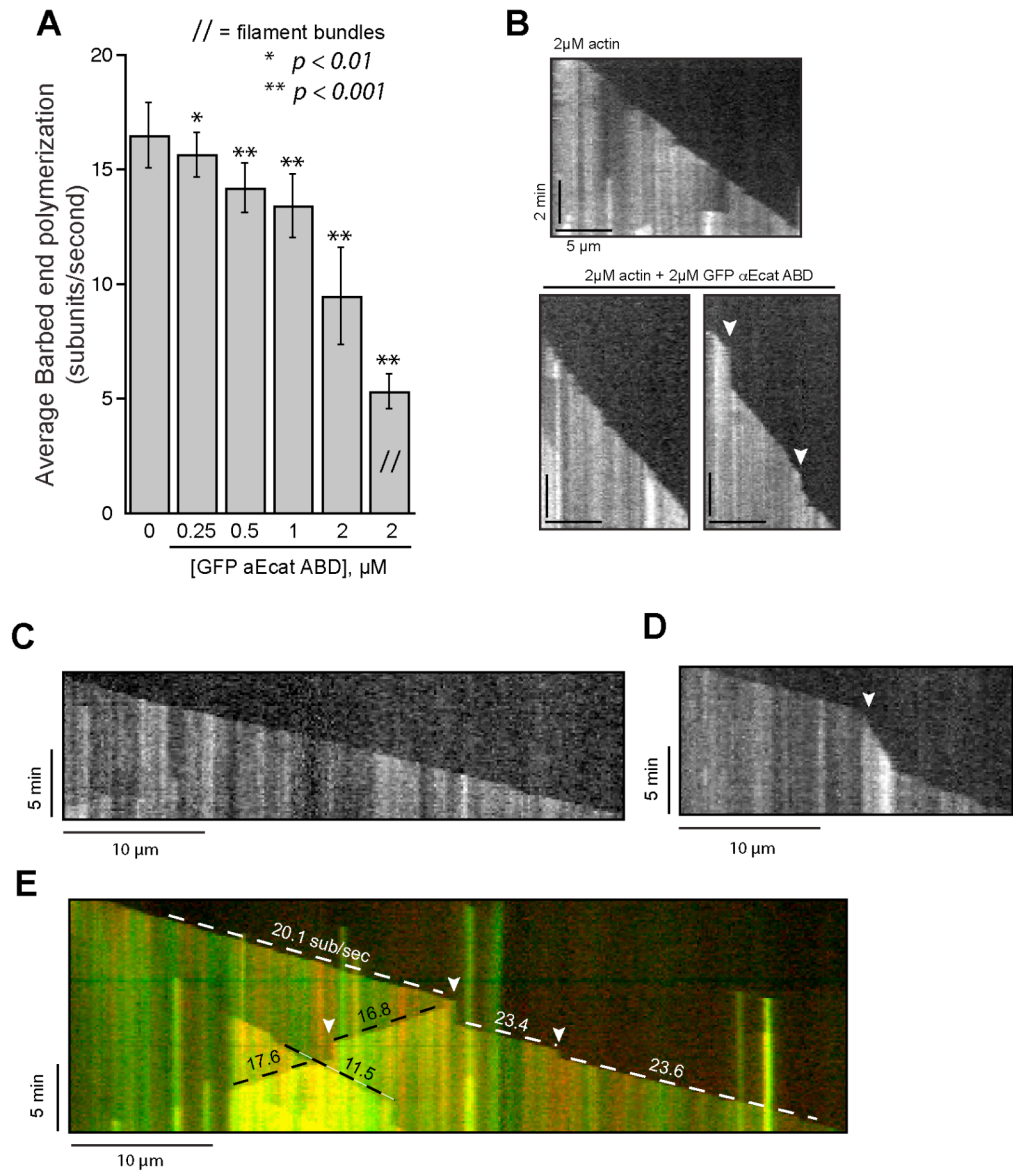
Figure 5



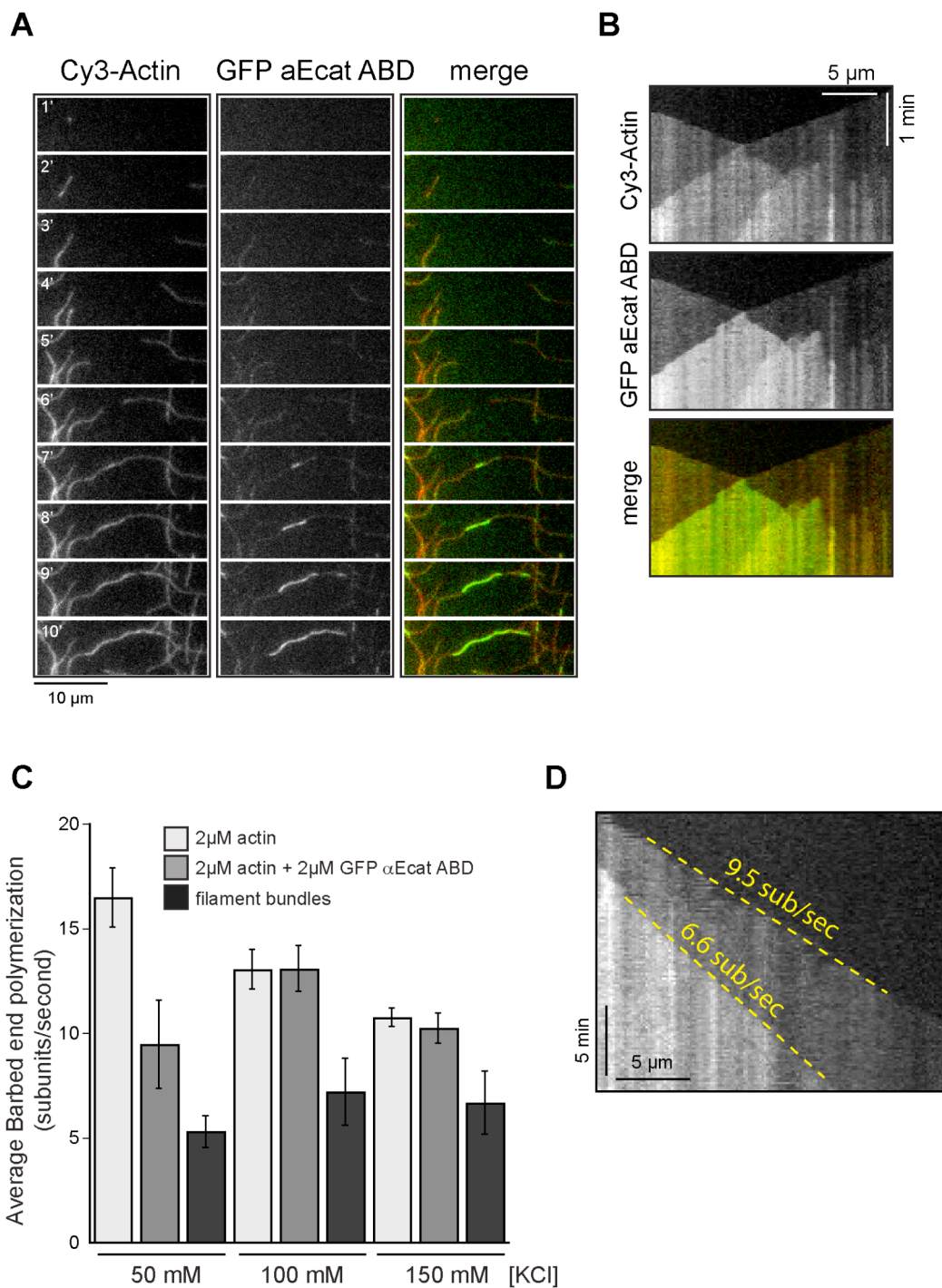
Supplemental Figure 1



Supplemental Figure 2



Supplemental Figure 3



Chapter 5

Single actin filament TIRF assay

Scott D. Hansen and J. Bradley Zuchero

In preparation for Adhesion Protein Protocols, 3rd edition
Edited by Amanda Coutts

1. Introduction

This protocol describes a method for passivating glass surfaces with PEG and Biotin-PEG polymers to be used for imaging static or dynamically growing actin filaments by TIRF microscopy. Since pegylation reduces nonspecific protein binding to glass, these glass surface can also be used for single molecule imaging of fluorescently labeled actin binding proteins (i.e. Cy3-VASP).

2. Materials

2.1 Silanization and pegylation of glass coverslips

1. Diamond pen (J&M Diamond Tool Inc, HS-110)
2. Glass weigh jars (Fisher, 03-420-5C)
3. Ceramic coverslip racks
4. 18 x 18 coverslips, 1.5 mm thickness
5. Bath sonicator
6. Sodium hydroxide (Fisher, S318-1)
7. Sulfuric Acid (Fisher, A300-500)
8. Hydrogen peroxide (30% solution, Fisher H325-500)
9. APTES (3-Aminopropyl)triethoxysilane (Sigma, A3648)
10. mPEG-5000-NHS (JenKem Technology USA) M-SCM-5000
11. Biotin-PEG5000-NHS (JenKem Technology USA, Biotin-PEG-5000-NHS)
12. Dimethylformamide (anhydrous, Sigma 227056)
13. Isopropanol (Fisher, A451-4)
14. Ethanol (Fisher, A995-4)

15. Acetone (Fluka, 00561)

16. MilliQ water

2.2 Labeling *A. castellani* actin with maleimide derivatives

1. Actin storage buffer (1X Buffer-A): 2 mM Tris [pH 8], 200 μ M ATP, 100 μ M CaCl_2 , 0.5 mM TCEP, 0.04% NaN_3 .
2. Actin labeling buffer: 5 mM Tris [pH 8], 200 μ M ATP, 100 μ M CaCl_2 .
3. Actin polymerization buffer (10X KMEI): 500 mM KCl, 10 mM MgCl_2 , 10 mM EGTA, 100 mM imidazole [pH 7.0].
4. Fluorescent dyes: Alexa488 maleimide (Invitrogen, A-10254), Cy3 maleimide (GE Healthcare, PA13131), and Cy5 maleimide (GE Healthcare, PA15131).
5. Biotin-PEG2-Maleimide (Fisher Thermo Scientific/Pierce, #21901).
6. PD10 salt exchange column (aka G25 Sephadex resin, GE Healthcare 17-0851-01)
7. 500 mM TCEP-HCl [pH 7.0 with KOH] (Pierce, 20491).
8. 1 M DTT dissolved in water (Roche, 100034).

2.3 Assembly of TIRF-M flow cells for attachment of filamentous actin

1. 15 mm wide Double sided tape (Tesa $\text{\textcircled{R}}$, Cat# 05338)
2. 25 x 75 x 1 mm Fisher Premium Microscope slides (Fisher, 12-544-7).
3. 3 mg/mL Poly-L-lysine PEG (Huang et al., 2001; Bieling et al., 2010 for grafting protocol).
4. 500 mM TCEP-HCl [pH 7.0 with KOH] (Pierce, 20491).

5. Streptavidin (Rockland immunochemicals S00-01). Resuspend lyophilized protein in 10 mM Tris [pH 8] to final concentration of 20-40 μ M. Ultracentrifuge at 350,000 x g (80,000 rpm with a TLA100.4) for 20 min to remove aggregates. Freeze with liquid nitrogen. Store at -80°C .
6. Heavy meromyosin (chymotrypsin cleaved rabbit skeletal muscle myosin, see X for protocol).
7. Biotin-phalloidin (Alexis Biochemicals; ALX-350-267-MC01).
8. Biotin-PEG11-Maleimide (Fisher Thermo Scientific/Pierce, #21911).
9. 10 mg/mL kappa casein dissolved in 1x PBS [pH 7.2] (Sigma C0406; bovine milk). Ultracentrifuge at 350,000 x g (80,000 rpm with a TLA100.4) for 20 min to remove aggregates. Use within 3 days.
10. Pluronic F-127 (Sigma, P2443): prepare 10% (vol./vol.) in water.
11. Actin polymerization buffer (10X KMEI): 500 mM KCl, 10 mM MgCl_2 , 10 mM EGTA, 100 mM imidazole [pH 7.0].
12. 1X PBS buffer: 2.9 mM NaH_2PO_4 , 7.1 mM Na_2HPO_4 , 137 mM NaCl, 2.7 mM KCl [pH 7.2 with NaOH].
13. Blocking buffer: 1% Pluronic F127, 50 μ g/mL kappa casein, 1x PBS [pH 7.2].
14. Wash buffer: 20 mM HEPES [pH 7], 200 mM KCl, 1 mM TCEP, 1 mg/mL BSA.

2.4 Visualization of dynamic actin filament assembly

1. Unlabeled G-actin stored in buffer A.
2. Alexa488, Cy3, or Cy5 labeled G-actin stored in buffer A.

3. 100 mM ATP dissolved in water [pH 7.0 with KOH] (Sigma, A26209-10G).
Store aliquots at -20°C.
4. 50 mg/mL BSA dissolved in water (Sigma, A0281-1G).
5. 1 M D-(+)-Glucose in water (Sigma, G5767).
6. 14.3 M β -mercaptoethanol (Sigma, M6250).
7. 2% methylcellulose (wt./vol.) (cP400, Sigma M0262). Suspend methylcellulose in 90-100°C water by vortexing in an ependorf. Invert tube and chill on ice to solubilize. Microcentrifuge and resuspend methylcellulose to homogeneity.
8. 10 mg/mL glucose oxidase dissolved in OSS buffer (Biophoretics/Serva Electrophoresis CAT# 22778.01). Ultracentrifuge at 350,000 x g (80,000 rpm with a TLA100.4) for 20 min to remove aggregates. Use within 3 days.
9. 10 mg/mL catalase dissolved in OSS buffer (Sigma C40-100MG; bovine liver). Ultracentrifuge at 350,000 x g (80,000 rpm with a TLA100.4) for 20 min to remove aggregates. Use within 3 days.
10. Actin storage buffer (1X Buffer A): 2 mM Tris [pH 8], 200 μ M ATP, 100 μ M CaCl_2 , 0.5 mM TCEP, 0.04% NaN_3 .
11. ME Buffer (10X) : 0.5 mM MgCl_2 , 2 mM EGTA.
12. OSS buffer: 20 mM HEPES [pH 7], 150 mM NaCl.
13. 2X TIRF Buffer: 40 mM HEPES [pH 7], 50 mM KCl, 2 mM MgCl_2 , 2 mM EGTA, 0.4% methylcellulose (cP400), 40 mM glucose, 40 mM beta-mercaptoethanol, 2 mg/mL BSA, 2 mM ATP, 250 μ g/mL glucose oxidase,

- 20 µg/mL catalase. Add oxygen scavenger enzymes (i.e. glucose oxidase and catalase) 5-10 minutes before combining with actin and imaging.
14. Protein dilution buffer: 20 mM HEPES [pH 7], 100 mM KCl, 1 mM TCEP, 1 mg/mL BSA.
 15. VALAP (1:1:1; vasoline:lanoline:paraffin).
 16. NIKON Eclipse TE2000-E microscope with Nikon Perfect Focus.
 17. ANDOR iXon cooled EM CCD camera.
 18. 100x Nikon Apo TIRF objective (NA 1.49)
 19. 40mW 488/514 Argon Ion laser or 40mW 542 crystal laser.
 20. Chroma/Shemrock multibandpass filter.
 21. Micromanager 4.0 software (Stuurman et al., 2007).

3. Methods

3.1 *Silanization and pegylation of glass coverslips*

1. Use a diamond pen to unambiguously mark 18x18 coverslips (e.g. mark the bottom right-hand corner of coverslip with a “C” or “R”). The scored side of the coverslips will be silanized and pegylated.
2. Place mark coverslips in a 1 liter glass beaker containing 200 mL of 3M NaOH (see **Note 1** for alternative cleaning strategies).
3. Sonicate in NaOH for 30-40 minutes. Swirl every 10 minutes. Save this base solution for washing glassware in later steps.
4. Decant NaOH and rinse coverslips with copious amounts of MilliQ water.
5. Add 200 mL of 100% isopropanol and sonicate for 15 minutes.

6. Meanwhile, make 200mL of 5% APTES in isopropanol (containing 1% water; see **Note 2-4**). APTES is very toxic and corrosive. Use glass pipets when aliquoting APTES.
7. Remove coverslips individually from isopropanol and transfer them to a new beaker containing the 5% APTES solution. Swirl each coverslip in the solution before dropping into the beaker. Bath sonicate the coverslips for 20-30 minutes.
8. Pour silane solution into waste container. Dispose of waste for EH&S collection. Do not pour APTES and isopropanol down the drain.
9. Rinse coverslips 3x with 100% isopropanol to remove excess silane.
10. Remove coverslips one-by-one. Dip into a series of 3 beakers containing isopropanol to wash off excess APTES. Wave forceps back and forth in isopropanol to clean coverslips. Rack coverslips in ceramic holders. Make sure you thoroughly clean off excess APTES with the isopropanol washes. Otherwise, an insoluble white precipitate will form during the baking step.
11. Bake for ≥ 2 hours at 90°C . The purpose of this step is to drive moisture off the glass surface which coordinates interactions between silane and water molecules. Dehydration of the coverslip surface caused the silane to form a covalently attached monolayer on the glass surface. Excess APTES on the glass surface will form an insoluble white precipitate when the glass is heated above 70°C . If this occurs, discard the coverslips and wash more thoroughly with isopropanol in the future.

12. After baking the APTES coated glass, bath sonicate the coverslips in 100% EtOH for 15-30 minutes.
13. Using forceps, remove individual coverslips from the ethanol. Dip and waft coverslips in a beaker of MilliQ water. Slowly pull the coverslip out of the water. If the glass is properly silanized, water will bead-up and pull away from the coverslip. Oven dry to remove residue water.
14. Weigh 45 mg of CH₃O-PEG-NHS and 5 mg Biotin-PEG-NHS (see **Note 5**). The ratio can be varied depending on the desired % of biotin-PEG. Add anhydrous dimethylformamide (DMF) to make a 50 mg/mL final concentration. If necessary, gently warm the solution to completely solubilize the PEG reagents. Be sure to use high quality/new DMF. Some solvents contain a large amount of fluorescent contamination which will bind to the glass.
15. Place 6 coverslip in each glass weigh jar with the diamond etched side up.
16. Spot 75µL of solution onto each coverslip.
17. Place second coverslip on top of first to make sandwich. Repeat. 6 sandwiches/12 coverslips per weigh jar.
18. Incubate at 75C for 2 hours.
19. Transfer weighing jars to a fume hood. Cool slightly before opening.
20. Separate coverslip sandwiches with forceps and place them in a large beaker of MilliQ water. Avoid touching the coverslips with your hands/gloves. Wash coverslips with copious amounts MilliQ water.

21. Remove coverslips one-by-one with forceps and swirl in a large beaker of water. Dry and store coverslips in a covered container at 4-25⁰ C.

Pegylated glass will last \geq 1 months.

3.2 Labeling *A. castellani* actin with maleimide derivatives

1. Make actin labeling buffer: 5 mM Tris [pH 8], 0.2 mM ATP, 0.1 mM CaCl₂.
2. Equilibrate PD10 column with 3 column volumes of actin labeling buffer.
3. Buffer exchange 2.5 mL of G-actin, 25-50 μ M, using a PD10 column to remove the reducing agent (i.e. TCEP).
4. Determine the new actin concentration by measuring the absorbance at 290 nm. $A_{290}=1=38.5 \mu\text{M}$ amoeba actin.
5. Add 3-5 molar excess Alexa488-maleimide (or Cy3/Cy5-maleimide).
Maleimide dyes are typically solubilized with DMSO to a working concentration of 10-20 mM. These reagents should be store in the -20⁰C freezer and used within a year.
6. Incubate on ice for 5-10 minutes on ice in a 15 mL conical, epi, or centrifuge tube.
7. Quench the labeling reaction by adding 10 mM DTT. Incubate for 5 minutes on ice.
8. Ultracentrifuge the labeled monomeric actin at 350,000 x g (80,000 rpm with a TLA100.4) for 20 min. This will help remove aggregated proteins and insoluble fluorescent dye.

9. Transfer supernatant to a new tube. Add 10x KMEI to polymerize actin for 2-3 hours at 20-25⁰C. Final KMEI buffer concentrations should be 50 mM KCl, 1 mM MgCl₂, 1 mM EGTA, and 10 mM Imidazole [pH 7.0].
10. Pellet labeled filamentous actin by ultracentrifugation at 195,000 x g (60,000 rpm with a TLA100.4) for 30 minutes.
11. Remove supernatant and gently wash the labeled actin pellet with 0.5 mL of buffer A to remove free dye. Note: when labeling actin with tetramethylrhodamine, labeled actin will not polymerize. Monomeric TMR-labeled actin must be separated from free dye with a desalting or gel filtration column.
12. Gently resuspend the actin pellet in 250-500 μL of buffer A. Pipet up and down to shear actin filaments. Transfer labeled actin in an ependorf. Allow actin filaments to depolymerize for 3-5 days at 4⁰C.
13. After depolymerization, ultracentrifuge the labeled actin at 350,000 x g (80,000 rpm with a TLA100.4) for 20 min to remove aggregates and small actin filament seeds (see **Note 6**).
14. To remove the last trace of unconjugated fluorescent dye, buffer exchange the depolymerized actin into buffer A using a NAP-5 (or PD-10) desalting column. Determine the new actin concentration and labeling efficiency using a spectrophotometer.
15. Measure the A₂₉₀ of your labeled actin and absorbance at the dye excitation peak. Since fluorescent dyes contribute to the A₂₉₀ signal, you'll

- need to subtract this contribution from the A_{290} of the labeled actin to accurately calculate the concentration and labeling efficiency (see **Fig. 1**).
16. To determine how much your dye contributes to the A_{280} , make a 1/1000 dilution of the dye in protein happiness buffer and perform a wavescan. Divide the A_{290} by the $A_{\text{ex peak}}$ or whatever other wavelength you desire.
 17. For actin labeled with Alexa488, $A_{290} (\text{actual}) = A_{290} (\text{labeled protein}) - (A_{290} (\text{labeled protein}) \times 0.132)$.
 18. Labeling efficiency = $[\text{protein}]_{290} / [\text{protein label}]_{\text{ex peak}}$
 19. This protocol can also be used to biotinylated actin with maleimide-PEG2-Biotin.

3.3 Assembly of TIRF-M flow cells for attachment of filamentous actin

1. Clean 25 x 75 x 1 mm glass slides with 3M NaOH, 100% ethanol, or oxygen plasma.
2. Cut double sided tape and attach to glass slides (see Figure 1). Firmly rub across the tape with a capped Sharpie pen to form a tight seal with the counter-glass. Although not essential for visualizing dynamic actin filaments, its worth passivating the counter-glass with poly-L-lysine PEG to minimize protein depletion effects (see **Fig. 2**).
3. To passivate the counter-glass, apply 5-10 μL of 3 mg/mL PLL-PEG to the space between the double sided tape. Allow PLL-PEG to dry on the surface and then wash the glass under a stream of MilliQ water. Allow the counter-glass and tape to dry before attaching the functionalized coverslip. After attaching a functionalized coverslip to the double sided tape, gently

press on the surface using capped Sharpie pen to create a tight seal between the glass and tape.

4. Flow 40 μ L blocking buffer (1% Pluronic F127, 50 μ g/mL kappa casein, 1x PBS [pH 7.2]) (see **Note 7**). Incubate for 2 minutes. If you make the working stock of block solution in water, the pluronic and kappa casein will bind to the PEG surface in a manner that causes Alexa488-actin to non-specifically bind to the surface. This will reduce your signal to noise the yield low quality data. Dilute in PBS or equivalent buffer. Kappa casein binds to positive charges.
5. Incubate blocking solution for 1 minute.
6. Wash with 40 μ L wash buffer (20 mM HEPES [pH 7], 200 mM KCl, 1 mM TCEP, 1 mg/mL BSA)
7. Flow 40 μ L of 50 nM streptavidin in wash buffer. Incubate for 30 seconds. Flush with 40 μ L wash buffer.
8. Flow 40 μ L of 50 nM biotin-PEG2-HMM in wash buffer. Incubate for 30 seconds. Flush with 40 μ L wash buffer. Alternatively, low concentration of biotin-PEG2-actin (0.1-0.5% labeling) or biotin-phalloidin can be used to attach static or dynamic actin filaments. These methods of attachment may not be compatible with every actin binding protein.
9. With myosin attached to the coverslip surface, phalloidin stabilized or dynamically elongating actin filaments can be attached to the functionalized glass surface (see **Fig. 3** and **Note 8**).

3.4 Visualization of dynamic actin filament assembly

1. *In vitro*, G-actin can spontaneously nucleates in the absence of other regulatory proteins (i.e. Arp2/3 complex, profilin, etc.). However, this process must initiated by the addition of MgCl_2 (cofactor), EGTA (Ca^{2+} chelator), and KCl.
2. In G-buffer, combine the appropriate volumes of dark actin and fluorescently labeled actin to make a working stock of 4.44 μM (10-30% Alexa488, see **Note 9**).
3. To exchange the Ca^{2+} for Mg^{2+} , combine 1 μL 10X ME and 9 μL of 4.44x Actin. Incubate for 2 min.
4. Meanwhile combine 18 μL 2.22X TIRF buffer (lacking OSS) with 1 μL glucose oxidase (40X) and 1 μL catalase (40X) (see **Note 10**). Be sure to calculate your buffer concentrations so that the addition of the OSS brings all of the TIRF buffer reagents/enzymes to 2X the desired final concentration.
5. Add 10 μL of protein dilution buffer to the 2X TIRF buffer ($V_f = 30 \mu\text{L}$). Typically this portion of the reaction mixture contains additional actin binding proteins (i.e. profilin, VASP, etc.).
6. To initiated the actin polymerization reaction, transfer the 30 μL TIRF buffer mix into the tube containing 10 μL of ME exchange G-actin. Pipet up and down twice. Flow all 40 μL into chamber using Whatman paper to wick the solution through the channel. Although it only requires 10-15 μL to flush the chamber, the 40 μL flush will ensure that the final concentrations in the TIRF chamber are identical to those aliquoted in the ependorf.

7. Seal the edges of the flow cells with VALAP, apply immersion oil, and mount on the TIRF microscope. In the presence of 1 μM actin, filaments will spontaneously nucleate and start elongating immediately. By time you have mounted your slide on the microscope and focused on the imaging surface (30-60 seconds), small actin filament seeds should be visible (see **Fig. 4A**). Imaging with a 5-10 second frame rate is sufficiently fast to capture the dynamic of actin filament assembly (see **Fig. 4B**). Under these conditions, actin filament barbed ends should elongate at a rate of ~ 10 subunits/seconds (see **Fig. 4C**).
8. For image analysis of microscopy data, we use ImageJ. An ImageJ Kymograph plugin, designed by J. Rietdorf (FMI Basel) and A. Seitz (EMBL Heidelberg) can be used to determine the single filament elongation rates. 1 μm of filamentous actin, contains 370 subunits.

Notes

Silanization and pegylation of glass coverslips

1. If you find that the functionalized glass contains a high fluorescent background, you can Pirahna etch the glass before silanizing. Pirahna is a 3:1 mixture of Sulfuric acid and hydrogen peroxide. Be sure to wear the proper protective. Alternative to 3M NaOH or Pirahna etching, warm 2% Hellmanex (Fisher, 14-385-944) can be used to efficiently strip glass of fluorescence and organic matter.
2. The addition of a small amount water is required for the amino-silane molecules to polymerize and form weak electrostatic interaction with each

other. Most reagent grade alcohol will contain enough trace water for this to be accomplished.

3. Isopropanol is not the only solvent that can be used to dilute silanes. Although more expensive, ethanol and acetone are good alternatives. Depending on your source of solvents, you may find that this is the source of most fluorescent contaminations on the final functionalized glass surface. If you plan to image single fluorescently labeled proteins, we might need to test multiple types of solvents to find the with the least amount of fluorescent contamination.
4. If you'd like to generate a more dense PEG functionalized glass surface, try silanizing the glass with (3-Glycidyloxypropyl)-trimetoxysilane (GOPTS) (Sigma 440167). GOPTS is destroyed by aqueous solvents. Therefore, it is necessary to wash the glass with anhydrous acetone after silanizing. After silanizing glass to GOPTS, you can use Hydroxy-PEG-NH₂ 3000Da (Rapp Polymere, 10-3000-20) and Biotin-CONH-PEG-NH₂ 3000Da (Rapp Polymere, 13-5000-25-20) to functionalize the surface. For more detail, refer to Bieling et al. (2010).
5. PEG-NHS and biotin-PEG-NHS reagents are quickly destroyed by moisture. In aqueous buffer, water acts as a nucleophile and reacts irreversibly with the NHS (half-life ~ 15 minutes). NHS reagents should be store at -20⁰C in a sealed desiccator. When using these reagent, allow the reagents storage bottle to warm to room temperature before open the bottle. If the bottle is cold, water will condense on the lyophilized

chemical and will gradually reduce the activity. We recommend storing pre-weighed quantities of each NHS reagent in ependorfs that are then sealed with parafilm and stored in a desiccator in the -20°C freezer. This will minimize the number of times any particular chemical container is opened and exposed to moisture.

Labeling actin

6. Without gel filtration, some actin dimers and trimers will be present. This is really only a problem if you want to measure nucleation rates. If you find that spontaneous nucleation is too rapid in an actin polymerization assay, hard spin or gel filter actin with a Superdex 75 column.

Single actin filament TIRF assay

7. Passivating the counter-glass surface with PLL-PEG will minimize protein depletion effects. Protein depletion can lead to inconsistent results if you choose to characterize an actin binding protein that is present at a nanomolar concentration in the assay.
8. It's important to optimize conditions such that filaments are not tacked down to the glass too much as to prevent them from polymerizing. Pauses should be infrequent by kymograph analysis. If the filaments are pausing too much or growing slowly, use less streptavidin and Biotin-HMM. Alternatively, reduce the percentage of conjugated biotin-PEG.
9. For polymerization assays, it's best to use 10% labeled actin. The higher the percentage labeled actin, the slower filaments will elongate. If you find that you have to use more than 10% labeled actin, something could be

wrong with your reagents. Alternatively, you might need to optimize your microscope configuration. Is your camera sensitive enough? How much laser power is coming through the objective? Your glass might not be properly functionalized, your actin is partially proteolyzed/denatured, or you're using too much excitation light. Also check the quality of your actin by SDS-PAGE if you're having problems.

10. Make glucose oxidase and catalase stocks fresh and ultracentrifuge at $350,000 \times g$ (80,000 rpm with a TLA100.4) for 20 min to remove aggregates. There is typically a large dark brown pellet after centrifuging catalase. Keep the supernatant and do not resuspend this pellet. Use within 3 days.
11. If you find that spontaneous nucleation is too rapid in an actin polymerization assay, hard spin or gel filter the actin to remove seeds.

Figure Legends

Figure 1

Extinction coefficients for maleimide fluorophore.

Figure 2

Cartoon for representation of TIRF flow cells.

Figure 3

Schematic for glass surface chemistry, pegylation, and actin filament attachment in the TIRF flow cells.

Figure 4

Imaging dynamic actin filament assembly by TIRF microscopy

(a). Image of actin filaments seed generate by polymerizing 1 μM actin (10% Alexa488 labeled) for approximately 2 minutes.

(b). Image montage showing the barbed end elongation of single actin filament in the presence of 1 μM actin (10% Alexa488 labeled).

(c). Kymograph showing the rate of change for a single actin filament elongating.

References

- Bieling, P., Telley, I.A., Hentrich, C., Piehler, J., and T. Surrey. (2010). Fluorescence Microscopy Assays on Chemically Functionalized Surfaces for Quantitative Imaging of Microtubule, Motor, and +TIP Dynamics. *Methods in Cell Biology*. v.95.
- Hansen, S.D. and R.D. Mullins. 2010. VASP is a processive actin polymerase that requires monomeric actin for barbed end association. *J. Cell Bio.* 191(3):571-84.
- Hermanson, G.T. (1996). *Bioconjugate Techniques*. San Diego: Academic Press (pp. 266-272). (Product # 20002T)
- Kovar, D.R., E.S. Harris, R. Mahaffy, H.N. Higgs, and T.D. Pollard. 2006. Control of the assembly of ATP- and ADP-actin by formins and profilin. *Cell*. 124: 423–435.
- Kuhn, J.R. and T.D. Pollard. 2005. Real-Time Measurements of Actin Filament Polymerization by Total Internal Reflection Fluorescence Microscopy. *Biophys. J.* 88:1387-1402.
- Kuhn, J.R. and T.D. Pollard. 2007. Single Molecule Kinetic Analysis of Actin Filament Capping. *J. Bio. Chem.* 282(38):28014-28024.

Figure 1

Fluorophore	Extinction coefficient (M ⁻¹ cm ⁻¹)	Absorbance Peak (nm)	Contribution to A290 (%)
Alexa 488	71,000	494	13.2
Cy3	150,000	550	8
Cy5	230,000	649	3

Figure 2

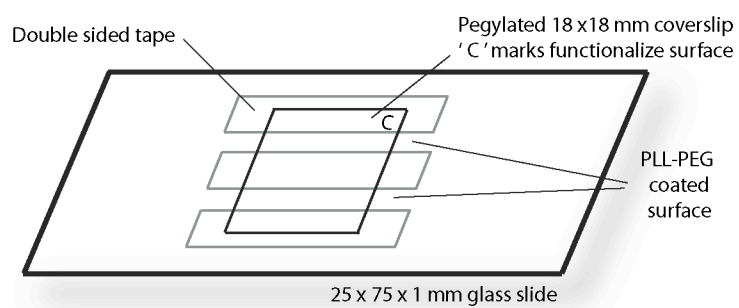


Figure 3

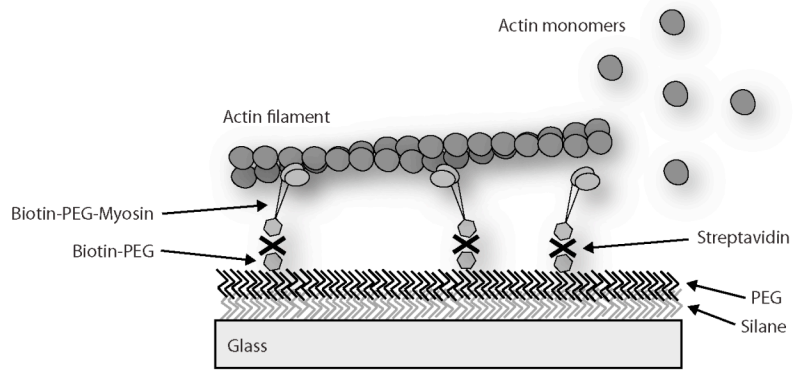
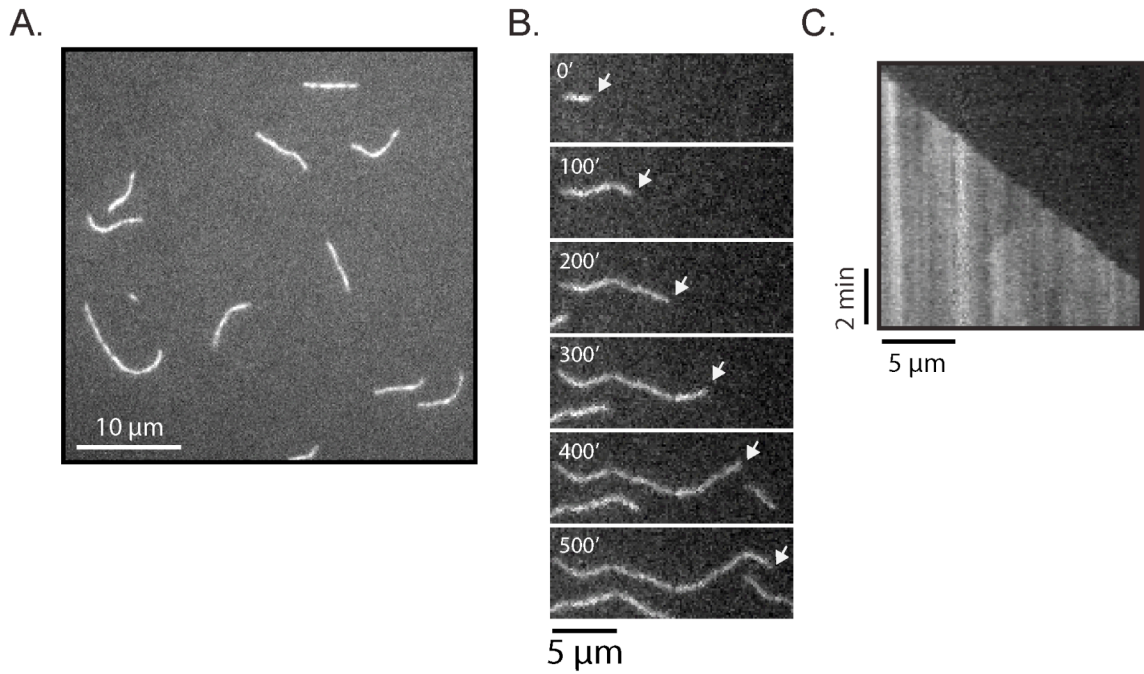


Figure 4



Chapter 6

Unpublished experiments:

Role of mDia2, VASP, and fascin in building filopodial actin networks

Scott D. Hansen

Introduction

In addition to the essential role of Ena/VASP proteins in the regulating the organization of filopodial actin networks, formins and fascin also contribute to the formation of these structures *in vivo*. Several formin family members have been shown to colocalize with VASP at the tips of filopodia when expressed as constitutively active forms. Interestingly, VASP and formin build slightly different types of filopodial actin networks, which arise from either convergent elongation and tip nucleation, respectively. Recently, a physical and genetic interaction between mDia2 and VASP was identified. Based on these findings, we hypothesize that mDia2 and VASP might modulate one or more of each others actin regulatory activities (i.e. filament nucleation or processivity). To test whether mDia2 and VASP can form a barbed end associated tip complex *in vitro*, we visualized fluorescently labeled mDia2 and VASP in the presence of elongating single actin filaments using TIRF microscopy. We found that interaction between mDia2 and VASP is too weak to observe a tip complex using the single actin filament TIRF assay.

In collaboration with Ena/VASP proteins, the F-actin cross-linker, fascin, tightly bundles parallel actin filaments and reduces actin network branching to favor filopodia formation. *In vivo*, Fascin and VASP have a distinct localization pattern in filopodia. Fascin localizes along the length of parallel filopodial actin filaments, while VASP localizes to the tip of filopodia where it interacts with the barbed ends of actin filaments. It is unclear how VASP and fascin influence each other spatial localization in actin networks. Using reconstituted actin networks,

we aimed image the localization of VASP and Fascin and test whether they intrinsically regulate each others spatial distribution *in vitro*.

Results

Consistent with results from Kovar et al. (2006), nanomolar concentrations of mDia2 FH1-FH2 domain can nucleate actin filaments in the presence of 2 μM actin or 2 μM actin-hProfilin1 (Figure 1A-C). In the presence of actin alone, the filament barbed ends elongate much slower than barbed end free of mDia2 (not shown). In the presence of 2 μM actin (10% Alexa488), 2 μM hProfilin 1, 0.5 nM mDia2 two population of filaments can be seen (Figure 1D). The bright filaments (no mDia2 bound) elongate at a rate of 12.8 sub/sec, while the second population of filaments (much dimmer fluorescence) polymerize at rate of 30.9 sub/sec (Figure 1D-1F). Interestingly, this mDia2 dependent rate enhancement was not previously observed by Kovar et al. (2006). I can reproduce their polymerization kinetics if I use 30% Alexa488 labeled actin monomers in the TIRF assay. It appears as though the labeled actin poisons mDia2 barbed end polymerization kinetics. I used 10% Alexa488 actin for all my assays.

To characterize the competition between mDia2 and VASP I first measured the kinetics of filament growth in the presence of 2 μM actin (10% Alexa488), 2 μM hProfilin 1, and 25 nM hVASP. All filaments elongates at 22 sub/sec. Next I added 0.5 nM mDia2 to the assay. Again, two populations of actin filaments were observed. The bright filaments (VASP dependent) elongate at a rate of 22 sub/sec, while the dim filaments (mDia2 barbed end associated)

polymerize at rate of 30.7 sub/sec (Figure 1F). I do not observe dim filaments change rate or increase in fluorescence due to VASP knocking mDia2 off the barbed end. Although I was able to detect a weak interaction between VASP and mDia2 on lipid coated beads (Figure 2) I never observed a mDia2-VASP barbed end tip complex in the single actin filament TIRF assay. I did however, observe single high processive SNAP-Alexa488-mDia2 molecules track the end of single actin filaments (Figure 3).

Characterization of Cy3-VASP and fascin actin filament binding revealed that both proteins can simultaneously bind to filamentous actin *in vitro* (data not shown). This suggests that fascin dependent exclusion of VASP from actin filament bundles is not the mechanism by which Ena/VASP proteins are localized to the tips of filopodia. A more probable mechanism would involve Ena/VASP proteins being tethered to the plasma membrane by a protein like Lamellipodin. Changes in the underlying actin network organization by fascin could increase the size of the Lpd-VASP tip complex and promote filopodial formation. Although we were unable to test this hypothesis *in vitro*, we did characterize the dynamics of fascin dependent actin filament bundling with single actin filament resolution (Figure 4).

Materials and methods

Protein purification:

his₁₀-TEV-mDia2^{(519-1171aa) M1041A} was cloned into a modified pETM-11 vector. Transformed BL21 bacteria containing pRARE (rare codon vector) were grown to OD₆₀₀ = 0.7. Cultures were transferred to 16⁰C shaker and grown for 60 minutes before induction with 50μM IPTG (OD₆₀₀ at time of induction was ~1.2). Cells were then grown overnight at 16⁰C, harvested, and lysed into buffer containing 20mM Tris pH 8, 400mM NaCl, 0.5mM BME. High speed supernatant was then pumped over a 5mL HiTrap Cobalt Chelating column. The column was washed with 100mL of buffer containing 20mM Tris pH 8, 10mM imidazole, 400mM NaCl, 0.5mM BME. The protein was then eluted with buffer containing 20mM Tris pH 8, 250mM imidazole, 400mM NaCl, 0.5mM BME. TEV protease was added to cleave the his₁₀ tag and the protein mixture was dialyzed into 10mM Hepes pH 7.5, 200mM NaCl, 1mM EDTA and 5mM BME overnight. Flow over NiNTA resin to remove uncleaved protein and his₆-TEV. Next, load cleaved mDia2 onto a Superdex 200 gel filtration column (323mL), equilibrated with 10mM Hepes pH 7.5, 200mM NaCl, 1mM EDTA, and 5mM BME. The dimer peak was immediately buffer exchanged into 10mM HEPES pH 7.5, 25mM NaCl, 1mM TCEP using a 10mL PD-10 desalting column and loaded onto a MonoS column. Two peaks eluted from the column, each having different nucleation activities in a pyrene assay. The high salt peak (right peak) had more activity and was therefore used for experiments (Figure 1A).

Pure mDia2^{(519-1171aa) M1041A} off the MonoS column (high salt peak) was dialyzed into 10mM HEPES pH 7.5, 100mM NaCl, 1mM TCEP, 20% glycerol overnight and then frozen with liquid nitrogen. The activity of mDia2 (frozen and unfrozen) were compared in a pyrene actin polymerization assay. In the presence of 2 μ M actin (5% pyrene) and activity of 5, 10, or 25nM mDia2 (frozen and unfrozen) were indistinguishable (Figure 1B). A negative control in which I froze mDia2 without glycerol showed a marked loss in activity (Figure 1B).

Single actin filament TIRF assay:

All TIRF assays were performed with GOPTS silanized glass that was coated with NHS-PEG/NHS-PEG-Biotin. Prior to experiments, glass was blocked with 1% Pluronic F-127, 1mg/mL BSA, and 50 μ g/mL kappa casein. Blocked glass was then washed with 50nM streptavidin, followed by 50nM biotin-HMM. Polymerization assays were performed in the presence of 10 mM imidazole pH 7.0, 50 mM KCl, 1 mM MgCl₂, 1 mM EGTA, 20 mM BME, 0.1 mM ATP, 0.2% methylcellulose cP400, 1 mg/mL BSA, 20 mM glucose, 200 μ g/mL glucose oxidase, and 150 μ g/mL catalase.

Figure Legends

Figure 1

VASP does not modulate mDia2 polymerase activity

- (a). mDia2 nucleates actin according to the pyrene fluorescence assay. In 96-well black bottom plate, 2 μ M actin (10% pyrene) was combined with 5, 10, or 25 nM mDia2 and allowed to polymerize.
- (b). mDia2 loses activity when frozen in the absence of cryo-protectant (20% glycerol). mDia2 stored under different conditions was combined at a final concentration of 5 nM with 2 μ M actin (10% pyrene labeled) and allowed to polymerize.
- (c). Image of actin filament length distribution from a pyrene actin polymerization assay performed in the absence or presence of 1 nM mDia2 for 2 minutes.
- (d). Kymographs for single actin filament barbed ends elongating in the presence of 2 μ M actin and 0.5 nM mDia2. Images show an example of a filaments with or without barbed end associated mDia2.
- (e). Montage of two actin filaments elongating with (dim) or without (bright) barbed end associated mDia2.
- (f). Table showing single actin filament growth rates in the presence of mDia2 alone, VASP alone, and the mDia2/VASP combined.

Figure 2

mDia2 interacts with VASP

- (a). Predicted VASP EVH1 binding sites found in different formin family proteins.

(b). Membrane tethered his10-GFP-mDia2 interacts with Cy3-VASP. Lipid coated glass beads (2.37 μm , PC:PS:Ni-NTA (75:23:2%)) were charged with 100 nM his10-GFP-mDia2 and then mixed with 100 nM of either Cy3-VASP(1-380aa) or Cy3-VASP(160-380aa). Fluorescent intensity of each protein is represented as line scans across the bead surface.

Figure 3

Single molecule imaging of barbed end associated SNAP-Alexa488-mDia2

- (a). Montage of single actin filament elongating in the presence of 2 μM profilin-actin (10% TMR, red) in the presence of 0.5 nM SNAP-Alexa488-mDia2 (green).
- (b). Kymograph showing SNAP-Alexa488-mDia2 processively attached with a single actin filament barbed end.

Figure 4

Actin filament bundling by fascin

- (a). Montage of fascin dependent parallel actin filament bundling. Filament elongation was performed in the presence of 2 μM actin (30% Alexa488) and 500 nM monomeric fascin.
- (b). Colocalization of Cy3-fascin and Alexa488-actin filament bundles.
- (c). Fascin dependent aster formation on a 5 μm polystyrene beads coated with ActA (30-262aa). Actin polymerization off the bead surface was performed in the presence of 7.5 μM actin, 100 nM Arp2/3, 500 nM fascin, and 0.2% methylcellulose.

Figure 1

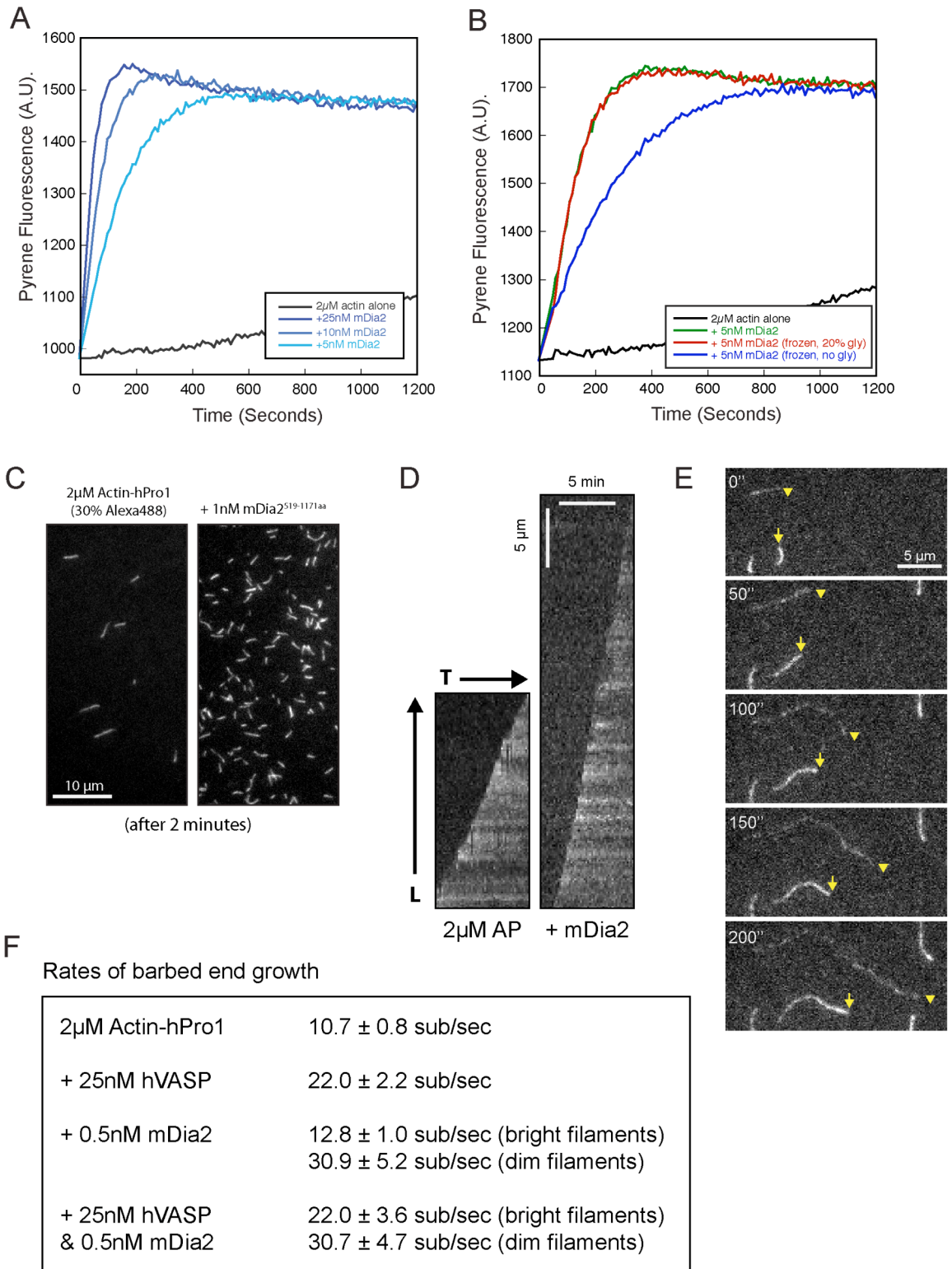
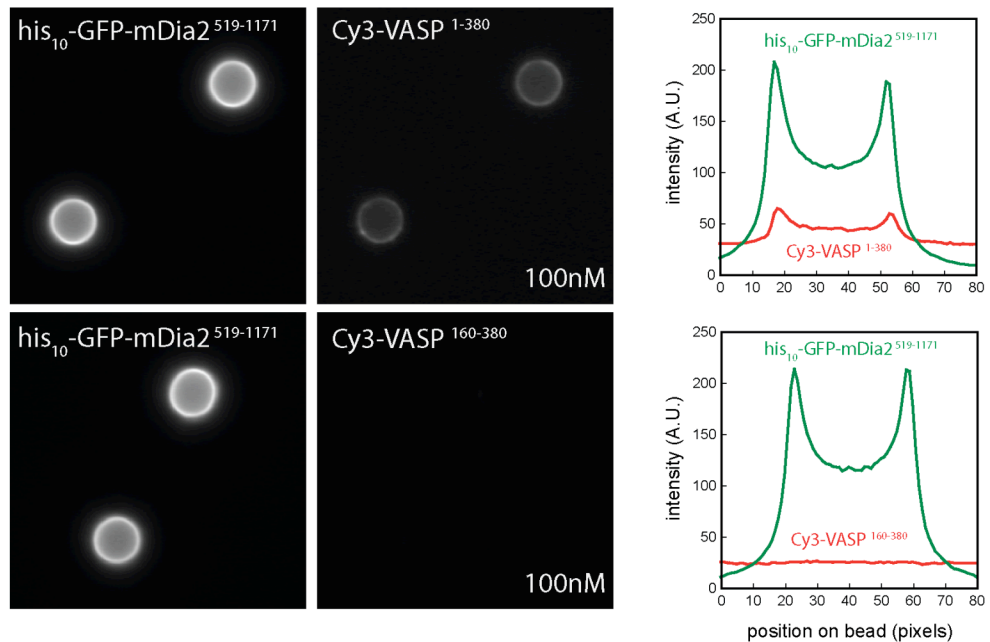


Figure 2

A.

DAAM2_HUMAN/539-54	DLPPPP
DIAP2_HUMAN/576-58	PLPPPP
DIAP2_HUMAN/938-94	TFPPPE
FHOD1_HUMAN/587-59	PLPPPP
FHOD1_HUMAN/597-60	PFPPPP
FMN1_HUMAN/902-90	PLPPPP
FMN2_HUMAN/933-93	PLPPLP
FMNL_HUMAN/583-58	DLPPPP
FMNL2_HUMAN/525-53	PLPPPP
FMNL3_HUMAN/517-52	PLPPPP
FMNL3_HUMAN/525-53	PLPPPP

B.

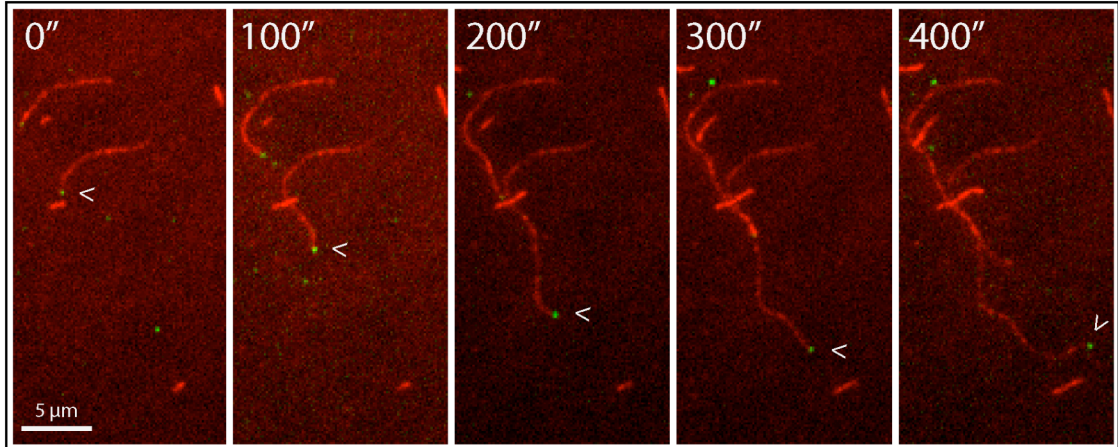


Lipid coated glass beads
 2.37 μ m beads, PC:PS:Ni-NTA (75:23:2%)
 buffer containing 100mM NaCl

Figure 3

A

TMR-Actin / SNAP-Alexa488-mDia2



B

TMR-Actin / SNAP-Alexa488-mDia2

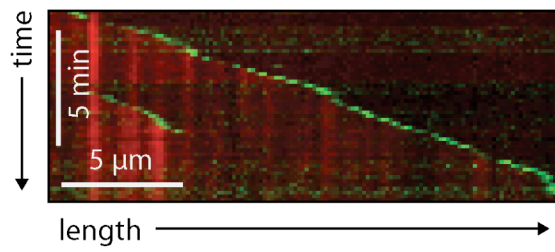
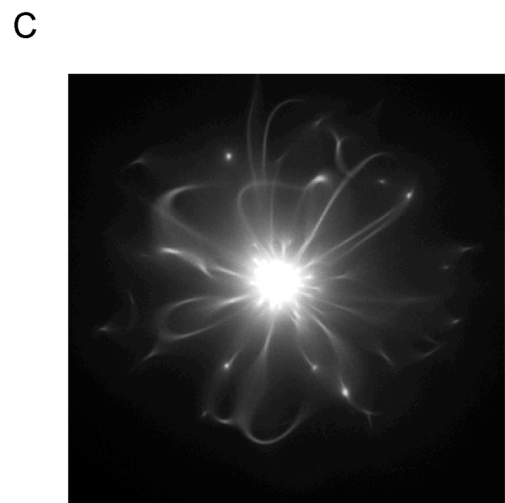
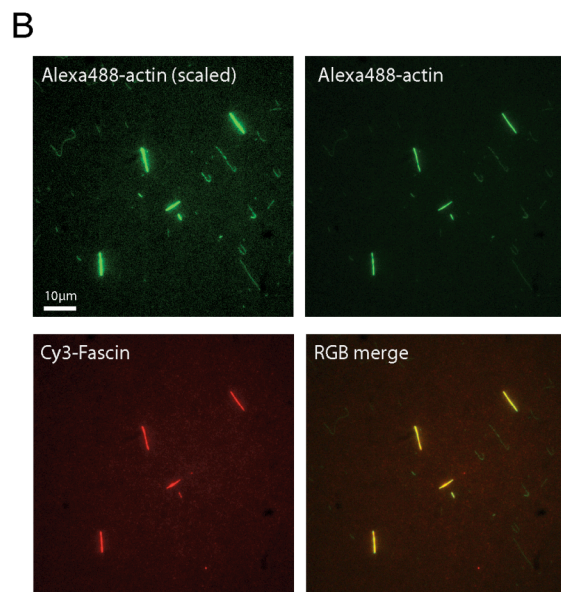
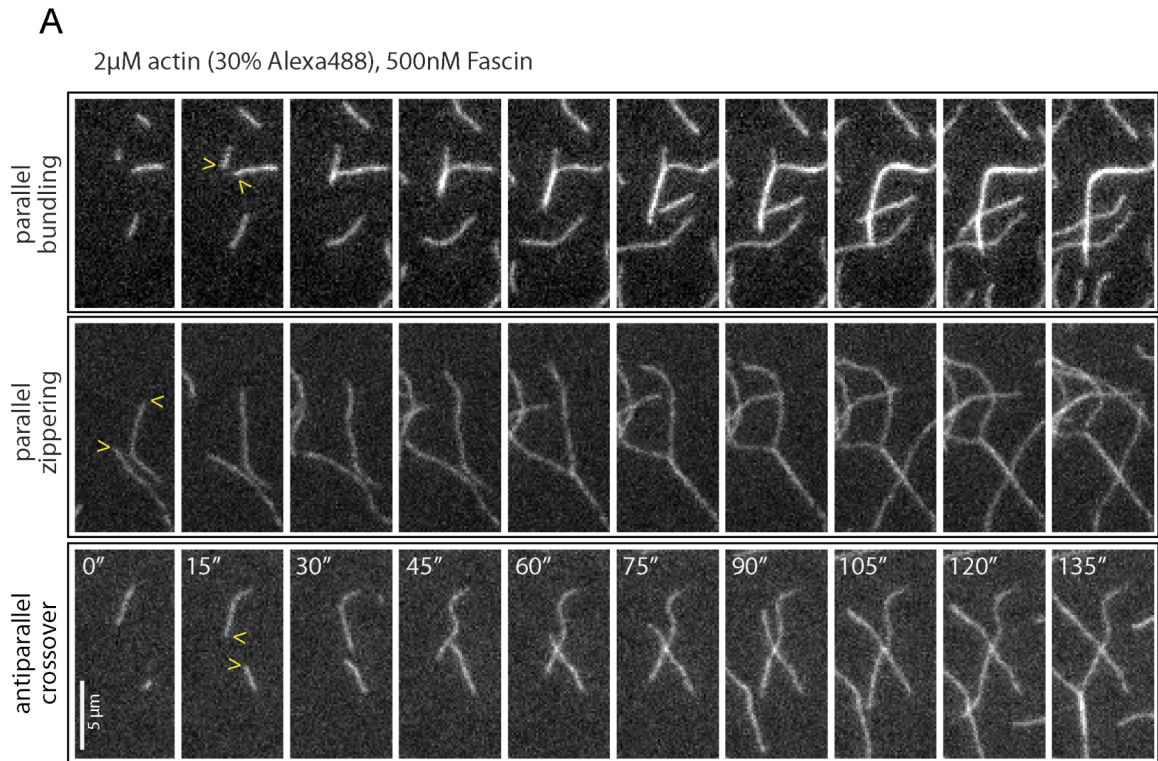


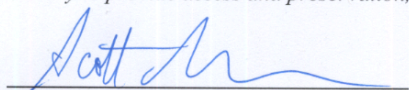
Figure 4



Publishing Agreement

It is the policy of the University to encourage the distribution of all theses, dissertations, and manuscripts. Copies of all UCSF theses, dissertations, and manuscripts will be routed to the library via the Graduate Division. The library will make all theses, dissertations, and manuscripts accessible to the public and will preserve these to the best of their abilities, in perpetuity.

I hereby grant permission to the Graduate Division of the University of California, San Francisco to release copies of my thesis, dissertation, or manuscript to the Campus Library to provide access and preservation, in whole or in part, in perpetuity.



Author Signature



Date